Delft University of Technology

Wind Power Ramps

Characterisation, Forecasting and Future Projection

Cheneka, B.R.

Important note
To cite this publication, please use the final published version (if applicable).
Please check the document version above.

WIND POWER RAMPS

CHARACTERISATION, FORECASTING AND FUTURE PROJECTION

WIND POWER RAMPS

CHARACTERISATION, FORECASTING AND FUTURE PROJECTION

Dissertation

for the purpose of obtaining the degree of doctor
at Delft University of Technology,
by the authority of Rector Magnificus prof. dr. ir. T. H. J. J. van der Hagen,
chair of the Board for Doctorates,
to be defended publicly on
Wednesday 13 September at 15:00 o'clock

by

Bedassa Regassa CHENEKA

Master of Science in Meteorology Science,
Arba Minch Universty, Arba Minch, Ethiopia,
Born in Bekoji, Ethiopia.

This dissertation has been approved by

promotor: Prof. dr. S. J. Watson and Prof. dr. S. Basu

Composition of the doctoral committee:

Rector Magnificus,	Chairperson
Prof. dr. S. J. Watson	Delft University of Technology, promotor
Prof. dr. S. Basu	University at Albany, promotor

Independent members:

Prof. dr. G. Harrison,	University of Edinburgh
Prof. dr. G. Kariniotakis	MINES Paris / PSL University
Dr. G. J. Steeneveld	Wageningen University and Research
Prof. dr. D. A. von Terzi	Delft University of Technology
Prof. dr. ir. H. W. J. Russchenberg	Delft University of Technology, reserve member

T U Delft Delft University of Technology

An electronic version of this dissertation is available at
http://repository.tudelft.nl/.

The more I study science, the more I believe in God.

Albert Einstein

CONTENTS

NOMENCLATURE

Acronyms

AEP	Annual energy production
ANN	Artificial neural network
BMU	Best-matching unit
C3S	Copernicus Climate Change Service
CMIP5	Coupled Model Inter-comparison Project Phase 5
CMIP6	Coupled Model Inter-comparison Project Phase 6
CNN	Convolutional neural network
CORDEX	Coordinated regional climate downscaling experiment
CWT	Continuous wavelet transform
EP	Empirical model
ERA5	ECMWF reanalysis v5
FC	Fully connected layers
GCMs	General circulation models
GFS	Global forecast system
IN	Inception network
LSTM	Long short term memory
MLP	Multi-layer perceptron
ML	Machine learning
NCEP	National Centers for Environmental Prediction
NWP	Numerical weather prediction
PBL	Planetary boundary layer
RE	Renewable energy
ResNet	Residual network
RC	Ramp cases
RCP	Representative concentration pathway
ReLU	Rectified linear unit
RNN	Recurrenet neural network
SLP	Sea level pressure
SOMs	Self-organizing maps
SSP	Shared Socioeconomic Pathways
SST	Sea surface temperature
TH	Defined threshold for min-max method
WL	Window length
WS	Wavelet-surrogate

Symbols

ΔP	Ramp magnitude
Δt	Ramp duration
$\Delta P/\Delta t$	Ramp rate
t_o	Ramp time
P_R	Rated power
y	The target value
$\overline{y}$	the model output
W	Weight of the neurons
n	Number of input feature
b	Bias
X	input features
ϕ	Activation function
σ	Sigmoid activation function
ψ	Mother wavelet function
a	Mother wavelet function scale
b	Mother wavelet function position
$P(t)$	Original time series of wind power
$P^*(t)$	Randomly shuffled wind power time series
$W(a,b)$	Continuous wavelet transform
W	The continuous wavelet transform of the original time series
W^*	The continuous wavelet transform of the surrogate time series
W_T^*	The threshold value of W^*
$R(t)$	Calculated mean normalized power ramps
a_{max}	Maximum resolved scale of $W(a,b)$
R'_u	Average ramp-up
R'_d	Average ramp-down
k	ramp-up period
l	Ramp-down period
n_k	Normalized power ramp-up
n_l	Normalized power ramp-down
$D(k)$	The kth ramp-up event
$D(l)$	The lth ramp-down even
S_1	Ten-days surrogate period
S_2	One-year surrogate period
R1	Small domain around the Belgian offshore wind farm
R2	Big domain around the Belgian offshore wind farm
U	Wind speed magnitude
u	Zonal wind speed
v	Merdional wind speed
P-0	1970 – 2005
P-I	2006 – 2041
P-II	2042 – 2077

$\Delta MSLP$	Mean sea level pressure change
ΔT	Temperature gradient
U+	U, x_{sin}, x_{cos}, u, v and ΔT
x_{sin}	Sine transform of time data
x_{cos}	Cosine transform of time data
$Loss$	The error between target and model output values
δP	Residual power error
$\alpha(t)$	Learning rate
h_{ci}	Gaussian neighborhood function
S1 – S5	Wind farm locations

SUMMARY

Offshore wind energy is a renewable energy source that is anticipated to be significant in the global shift towards clean and green energy in order to reduce the reliance on fossil fuels and mitigate climate change. In recent years, the overall output of offshore wind energy has increased, and as a result, investments in offshore wind power have been on the rise. Governments around the world, particularly those in Europe, are investing heavily in establishing and maintaining offshore wind farms, with a particular focus on the North Sea. This is because the North Sea has high wind speeds and shallow waters, making it an ideal location for offshore wind farms.

However, one of the challenges of offshore wind energy is that it exhibits temporal oscillations, which can lead to electrical load fluctuations. This is because wind power is naturally volatile and can experience fast drops or increases in power generation, which are known as wind power ramps. In order to ensure the stability of wind power and the electrical grid, it is important to carefully monitor the temporal variability of wind power ahead of time.

To do this, it is necessary to model and forecast the available wind power production and understand the features of wind power ramps. This can help to ensure the provision of offshore wind power production and recognise the timing, length, and amplitude of wind power ramps. It is also important to understand the link between large-scale meteorological systems and wind power production and the behaviour of wind power ramps. This can provide valuable insights into the deployment of offshore wind power production and how wind power and wind power ramps may change in response to climate change.

The research results presented in this thesis focus on investigating offshore wind power generation and wind power ramp features over the North Sea region. The research covers four main areas, including modelling and enhancing the forecasting of offshore wind power production and wind power ramps using deep learning neural network models, developing a wavelet-surrogate algorithm to detect wind power ramp events, quantifying the relationship between wind power production and wind power ramp behaviour with weather patterns using self-organising maps (SOMs), and quantifying the projected change in wind power production and wind power ramps in response to future climate change.

Overall, this research provides valuable insights into the behaviour of offshore wind power production and wind power ramps, and how this behaviour can be managed currently and in the face of future climate change. The findings of this research can be used to help balance supply and demand and aid the wind energy sector by providing a better understanding of the characteristics of wind power production, wind power ramps and the factors that drive these. It can also help to enhance wind power and power ramp forecasting methods and detection algorithms, and provide valuable insights into

the meteorological systems that govern the magnitude of wind power output and wind power ramp characteristics.

SAMENVATTING

Offshore windenergie is een hernieuwbare energiebron die naar verwachting een belangrijke rol zal spelen in de wereldwijde verschuiving naar schone en groene energie om de afhankelijkheid van fossiele brandstoffen te verminderen en klimaatverandering te matigen. De afgelopen jaren is de totale output van windenergie op zee toegenomen, waardoor de investeringen in windenergie op zee in de lift zitten. Overheden over de hele wereld, met name in Europa, investeren fors in het opzetten en onderhouden van offshore windparken, met bijzondere aandacht voor de Noordzee. De Noordzee heeft namelijk hoge windsnelheden en ondiep water, waardoor het een ideale locatie is voor offshore windparken.

Eén van de uitdagingen van offshore windenergie is echter dat het tijdelijke trillingen (oscillaties) vertoont, wat kan leiden tot fluctuaties in de elektrische belasting. Dit komt omdat windenergie van nature vluchtig is en snelle dalingen of toenames in stroomopwekking kan vertonen, die bekend staan als power ramps (fluctuaties in de stroomvoorziening). Om de stabiliteit van windenergie en het elektriciteitsnet te waarborgen, is het belangrijk om de tijdelijke variabiliteit van windenergie van tevoren goed te monitoren.

Om dit te doen, is het noodzakelijk om de beschikbare windenergieproductie te modelleren en te voorspellen en de kenmerken van fluctuaties in de windenergie te begrijpen. Dit kan helpen om de levering van offshore windenergieproductie te waarborgen en de timing, lengte en amplitude van fluctuaties in de windenergie te herkennen. Het is ook belangrijk om het verband te begrijpen tussen grootschalige meteorologische systemen en de productie van windenergie en het gedrag van fluctuaties in de windenergie. Dit kan waardevolle inzichten opleveren in de inzet van offshore windenergieproductie en hoe windenergie en -fluctuaties kunnen veranderen als reactie op klimaatverandering.

De onderzoeksresultaten die in dit proefschrift worden gepresenteerd, richten zich op het onderzoeken van de opwekking van offshore windenergie en fluctuatie-kenmerken van windenergie in de Noordzee regio. Het onderzoek bestrijkt vier hoofdgebieden, waaronder het modelleren en voorspellen van offshore windenergieproductie en fluctuaties met behulp van deep learning neurale netwerkmodellen, ontwikkeling van een wavelet-surrogaatalgoritme om windenergiefluctuaties te detecteren, kwantificering van de relatie tussen windenergieproductie en windenergie fluctuatiegedrag met weerpatronen, gebruik makend van zelforganiserende kaarten (SOM's), en het kwantificeren van de verwachte verandering in windenergieproductie en windenergiefluctuaties als reactie op toekomstige klimaatverandering.

Over het algemeen biedt dit onderzoek waardevolle inzichten in het gedrag van offshore windenergie productie en fluctuaties in de windenergie, en hoe dit gedrag kan worden beheerst, nu en in het licht van toekomstige klimaatverandering. De bevindingen van dit onderzoek kunnen helpen om vraag en aanbod in evenwicht te brengen en de windenergiesector helpen door een beter inzicht te geven in de kenmerken van

windenergieproductie, fluctuaties in de windenergie en de bepalende factoren daarachter. Het kan ook helpen bij het verbeteren van windenergie en-voorspellingsmethoden voor fluctuaties in de stroomvoorziening en detectiealgoritmen, en waardevolle inzichten bieden in de meteorologische systemen die de omvang van windenergie-output en kenmerken van fluctuaties in de windenergie bepalen.

1

INTRODUCTION

I have not failed. I've just found 10,000 ways that won't work.

Thomas Alva Edison (February 11, 1847 – October 18, 1931)

1

This chapter presents trends in the development of wind power and improvement in turbine technology over recent years. The topic of wind power ramps is discussed, which is an important area for this dissertation. Challenges related to wind power ramps, such as ramp detection and forecasting and their association with weather systems are also discussed briefly. Furthermore, how renewable energy, more specifically wind energy, is influenced by climate change under the current projected climate change scenarios is also introduced. Finally, the research questions, objectives, and organizational structure of this thesis are described.

1.1. INTRODUCTION

Wind is one of the earliest sources of energy used by humans. For instance, it has been used for sailing by mariners for many centuries. Wind power was used to grind or mill grains and for water pumping in Europe in the pre-Industrial Revolution era. For instance, since 1350, the Netherlands used windmills to turn marshes and shallow lakes into agricultural land [1, 2]. Windmills were one of the primary sources of energy until the beginning of the industrial revolution when, in the 1880s, fossil fuels became the most utilised source of energy [3].

The wind energy industry grew rapidly in the 2000s. This was mainly due to volatile gas prices and increasing concerns about climate change which resulted in the Kyoto Protocol in 1997. Wind energy was seen as an important means to reduce greenhouse gas emissions. In the late 2000s, the number of offshore wind farm projects increased significantly. European offshore wind farms are increasing in size and are being built in deeper water. Globally, about 88% of offshore wind farms are located in Europe [4] spurring developers and manufacturers to invest in the sector.

Investments are increasing in research, installation, operation and maintenance of offshore wind farms. As a result, European countries have seen rapid progress in increasing their offshore wind farm fleets, particularly in the North Sea. The climatology of the North Sea and its relatively shallow water depth are favourable for the installation and operation of wind farms.

1.2. OFFSHORE WIND POWER PRODUCTION TRENDS AND TUR-BINE SIZES

Total wind power production has been rapidly increasing, particularly since 2009 [5]. European offshore wind turbine average rated powers and wind farm sizes have increased significantly. In 2009, turbine rated power was about 3 MW, increasing to 8MW by 2019 (Figure 1.1a). At the same time, offshore wind farm size increased from 200 MW in 2009 to 600MW in 2019 (Figure 1.1b). The annual installed and cumulative capacity of offshore wind power between 2009 and 2019 are shown for 12 European countries in Figure 1.1c, where total capacity has increased from about 0.4GW in 2009 to 22.5GW in 2019. This corresponds to 502 new offshore wind turbines connected to the grid across 10 wind farms. In 2021, European countries added a net offshore capacity of about 3.5GW. Europe had 28GW of installed offshore wind capacity as of August 2022, and the UK had the largest installed offshore capacity in Europe, followed by France, Netherlands, and Ger-

many [6].The North Sea, Baltic, Irish Sea and Atlantic are all potential areas for European offshore wind power production. At present, the North Sea and nearby Atlantic Ocean contribute around 90% of global installed offshore wind power capacity [7].

Much has been done to increase the contribution of wind energy and to shift the energy supply from fossil fuel to renewable energy sources to mitigate climate change. Progress has been seen in turbine size, for instance, the deployment of greater turbine hub heights and longer blades giving larger swept areas [5].
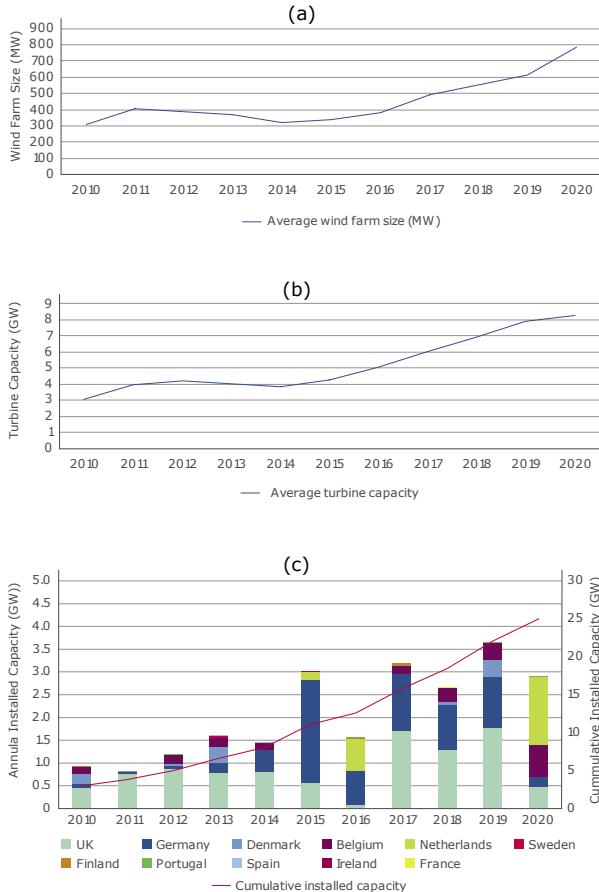
Figure 1.1: (a) wind farm size trend in MW, (b) wind power turbine capacity trend in MW, and (c) wind power production trend [8].

1.3. WIND POWER VARIABILITY

As might be expected, wind power production is closely related to the wind speed (Figure 1.2) and this is subject to temporal fluctuations. Wind speed can be converted to expected wind power using a turbine power curve. There is no wind power production for wind speed values between 0 and 3m/s, power output is approximately a cubic func-

tion of the wind speed between 4 and 12m/s, and rated output is achieved when the wind speed is between 12 and 25m/s. The turbine shuts down when wind speed values are higher than 25m/s to protect the turbine from potential damage due to high loads. This varying output presents a challenge when integrating wind power production into a power system that requires relatively stable, predictable and dispatchable power generation sources. Wind power ramps, which are rapid increases or decreases of wind power, represent challenges to this integration [9–11].
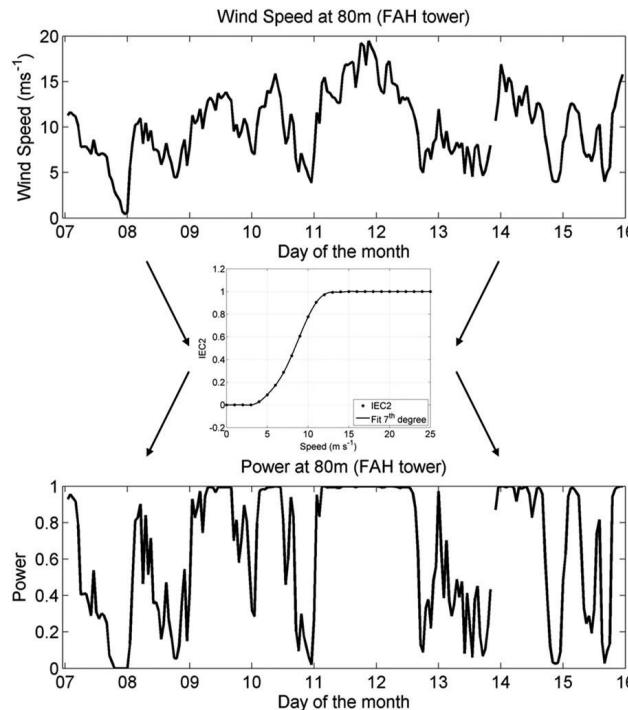
Figure 1.2: (top) Time series of 80m wind speed and (bottom) the hypothetical equivalent normalized power (capacity factor) using (centre) an IEC class 2 wind power curve. Data are for the period 7 – 15 Jan 2012 from one of four South Dakota State University (SDSU) 80-m-tall towers [Faith (FAH): latitude 45.0539°, longitude -102.2630°, altitude 797m; [12].

The temporal fluctuation of wind power production manifested in the form of wind power ramps is caused by complex physical processes and atmospheric dynamical phenomena, such as land/sea transitions, pressure systems, thunderstorms, wind gusts, cyclones, and low-level jets [14]. Climatological conditions at the local scale can also cause variable wind power generation [15]. Figure 1.3 illustrates the temporal and spatial scales associated with various meteorological phenomena. These phenomena strongly influence the magnitude of wind power production and the characteristics of wind power ramps [16–19], for example, small-scale meteorological phenomena tend to cause short duration ramps, whereas long duration ramps are mainly associated with large scale meteorological phenomena. Gaining a better understanding of how wind power production
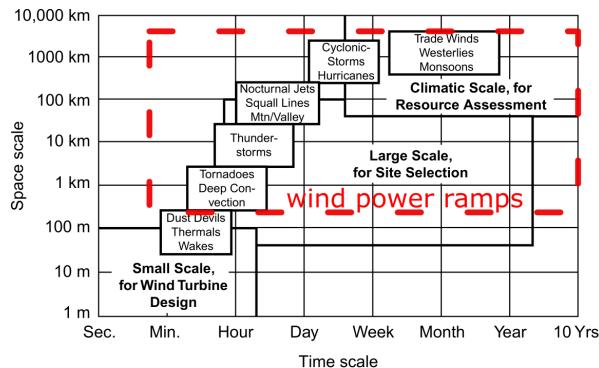
Figure 1.3: Temporal and spatial scales of atmospheric motion related to the scale of wind resources of Europe [13].

and wind power ramps are associated with meteorological phenomena could give a better insight into patterns of production, including how well they might be forecast and what action might be taken when integrating wind power into a network. However, detecting and characterising wind power ramps remains a challenge.

1.4. CLIMATE CHANGE AND IMPACTS ON WIND POWER

By 2050, it is expected that onshore and offshore wind power (along with solar power) will be major renewable energy generation sources that will generate more than 35% of total electricity [20]. In the next three decades, the offshore wind power market is expected to show significant growth in order to meet the Paris Climate Agreement of 2015. This ambitious agreement aimed to limit the rise in global temperature to "well below" $2°C$ and ideally to limit warming to $1.5°C$ in the current century relative to the pre-industrial period [21]. For example, compared with 2018, in 2030, the total installed offshore wind power capacity is expected to increase from 23GW to 228GW, then to about 1000GW in 2050.

Although wind power is seen as a significant weapon in the fight to mitigate global warming, it is expected to be affected by climate change. There is a need therefore, as we accelerate the development of wind power to meet global targets, to better understand how projected climate change is likely to affect wind power production including its temporal fluctuation, i.e. wind power ramps.

1.5. RESEARCH MOTIVATIONS AND OBJECTIVES

Wind is anticipated to be among the top sources of future renewable energy production. However, wind power displays strong temporal variability. In the contemporary and projected future climate, detecting and modeling wind power ramps is an important challenge from the perspective of power system integration.

Accurate wind power production and wind power ramp forecasts are required to minimize the difference between energy supply and demand. Studies that work on improving wind power and wind power ramp forecast model(s) are needed. In this the-

sis, we use deep learning models to model and forecast wind power (and wind power ramps).

Past studies have proposed methods to identify wind power ramp events from temporal wind power production. However, many of these methods only depend on a threshold of wind power change relative to rated power, whereas in many applications, it is necessary to consider ramps of different timescales. In this thesis, a method is developed that can be used to detect wind power ramp events over a range of ramp duration times.

Weather patterns determine the magnitude of wind power production, and the strength and characteristics of wind power ramps. Studies that can quantify the relationship between weather patterns and wind power production (and thus, wind power ramps) are necessary for power production forecasting and longer term planning. Such studies are of particular benefit to the North Sea region, as this will be one of the largest sources of future European offshore wind power production. Thus, this study focuses on this region as a case study to show how offshore wind power production, and wind power ramps are associated with large-scale synoptic weather systems.

Climate change has the potential to affect the future production patterns of renewable energy, including wind power and power ramps. Quantifying these projected changes and their impact on wind power production is needed for the future integration of wind power into energy networks.

In summary, the main objectives of this research are:

- To develop a simple and efficient algorithm to detect wind power ramps with ranges of duration.

- To explore the potential of deep learning in modeling and forecasting wind power and wind power ramps.

- To quantify the association of weather patterns with wind power and power ramp characteristics.

- To quantify future changes in the characteristics of wind power production and their relationship to weather patterns.

1.6. RESEARCH QUESTIONS

Following the research motivation and objectives, the following high-level research questions are formulated and will be answered in the subsequent chapters of the thesis.

The formulated research questions are:

- Can an algorithm be developed to detect wind power ramps over a range of durations?

- Do deep learning models have the potential to improve wind power and power ramp modeling and forecasting?

- How do weather patterns affect the magnitude of wind power production and the characteristics of power ramps?

1

- Are there expected to be changes in future patterns of wind power production and power ramps related to climate change?

The research questions are described in detail as follows:

1.6.1. CAN AN ALGORITHM BE DEVELOPED TO DETECT WIND POWER RAMPS OVER A RANGE OF DURATIONS?

Detection of power ramp events from a temporal wind power series is a particular challenge in wind energy. Wind power ramp detection algorithms have been proposed by several scholars but there are shortcomings in the capabilities of these algorithms in identifying ramp events. For instance, most algorithms apply a threshold approach, based on a change in wind power magnitude over a given time as a proportion of rated power. This approach has its drawbacks, e.g. it may not detect multiple ramp events with a variable duration. Also, it has difficulty in detecting ramp event start and end times. To overcome these limitations, a new wind power ramp detection algorithm is developed and applied.

1.6.2. DO DEEP LEARNING MODELS HAVE THE POTENTIAL TO IMPROVE WIND POWER AND POWER RAMPS MODELING AND FORECASTING?

Predicting available wind power production and wind power ramps ahead of time helps the wind power industry to plan the supply of wind power production. There has been much research to increase the forecast accuracy of wind power production and wind power ramps. However, the wind power industry still needs improved wind power forecasting model(s) with better forecasting skill. Studies have shown that the combination of physical and data-driven models is advantageous in improving model skill. This study uses state-of-the-art deep learning models to generate improved forecasts of wind power production and wind power ramps.

1.6.3. HOW DO WEATHER PATTERNS AFFECT THE MAGNITUDE OF WIND POWER PRODUCTION AND THE CHARACTERISTICS OF POWER RAMPS?

Weather systems determine the magnitude of wind power production and the characteristics of wind power ramps. Understanding the association of weather systems with wind power production (and ramps) benefits the deployment of wind generation and its integration. Several studies have looked at the association of weather patterns with onshore wind power production, particularly in Europe. In this study, the association of weather patterns with offshore wind power production and wind power ramps over the North Sea area has been studied, using the Belgian offshore wind farm fleet as a case study.

1.6.4. ARE THERE EXPECTED TO BE CHANGES IN FUTURE PATTERNS OF WIND POWER PRODUCTION AND POWER RAMPS RELATED TO CLIMATE CHANGE?

Patterns of wind power production and wind power ramp characteristics may change in the future due to changes in the prevalence of weather patterns driven by climate change. This study quantifies future changes in weather pattern frequency and its im-

1

pact on future wind power production and power ramps.

1.7. THESIS ORGANIZATION

CHAPTER 1 INTRODUCTION
This chapter presents trends in wind power production, challenges related to wind power variability and wind power ramps, research motivation and objectives, research questions, and the organization of this thesis.

CHAPTER 2 BACKGROUND
This chapter reviews the relevant literature in detail, mainly concerning wind power ramp detection, modeling (forecasting) and projected climate change as it relates to wind power. Some of the wind power ramp detection and forecasting techniques are discussed briefly. Moreover, the projected change in climate change and impacts on renewable energy is also presented in this chapter.

CHAPTER 3 WIND POWER RAMPS DETECTION ALGORITHM
A new technique for detecting wind power ramps based on wavelets to discriminate events of different magnitudes and durations is presented in this chapter. The technique is described in detail and its application demonstrated using actual offshore wind power data.

CHAPTER 4 ENHANCING FORECASTS OF WIND POWER AND WIND POWER RAMPS
This chapter presents the potential of deep learning in modeling and forecasting wind power production and wind power ramps. The deep learning neural network architectures that are implemented to model and forecast wind power production and wind power ramps characters are presented. Furthermore, model performance in improving wind power production and wind power ramp forecasts is presented and discussed.

CHAPTER 5 WIND POWER AND POWER RAMPS: ASSOCIATION WITH WEATHER PATTERNS
The type of prevailing weather pattern determines the magnitude of wind power production and the characteristics of wind power ramps. In this chapter, first, a discrete number of European-area weather patterns is identified from high-dimensional time series of sea level pressure clustered using a self-organizing map (SOM). The association of these weather patterns with offshore wind power production and wind power ramps is quantified.

CHAPTER 6 PROJECTED CHANGES IN WIND POWER AND POWER RAMPS
In this chapter, a SOM is used to cluster future projected weather patterns over Europe. Future changes in the characteristics of offshore wind power production and wind power ramps for the North Sea region are investigated, including how these changes are related to the change in the prevalence of particular weather patterns.

CHAPTER 7 CONCLUSIONS AND RECOMMENDATIONS
Chapter 7 discusses the conclusions, limitations, and recommendations from this thesis.
    The outline of this thesis and connection between the chapters are shown schematically in Figure 1.4.

Chapter 1
Introduction

Chapter 2
Background

Chapter 3 Wind power ramps detection algorithm
[22]

Chapter 4
Enhancing forecasting of wind power and wind power ramps

Chapter 5
Wind power and power ramps: association with weather patterns
[23, 24]

Chapter 6
Projected changes in wind power and wind power ramps
[25]

Chapter 7
Conclusions and recommendations
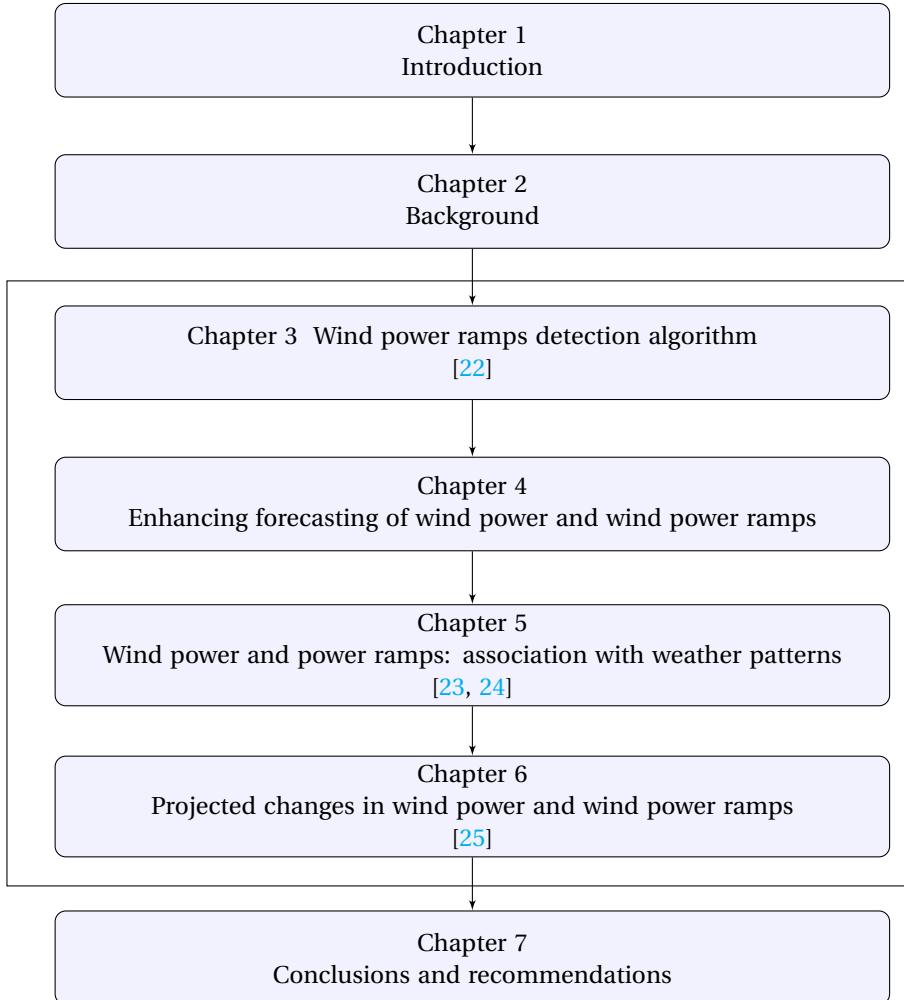
Figure 1.4: The flowchart shows the connection between the chapters of this thesis with published papers.

2

BACKGROUND

All of us, at certain moments of our lives, need to take advice and to receive help from other people.

Alexis Carrel (28 June 1873 – 5 November 1944)

This chapter provides an overview of the thesis background, which primarily focuses on wind power production and wind power ramps. The thesis aims to find a robust way to detect wind power ramp events, forecast wind power and power ramps, analyze their association with large-scale meteorological systems, and examine their changes in a projected future climate. To achieve these objectives, the study uses various data sources, including observed aggregated wind power, global reanalysis, numerical weather prediction, and downscaled global models. Moreover, the study employs wavelet transforms, and unsupervised and supervised machine learning techniques. The information presented in this chapter serves as a background for the subsequent chapters of the thesis.

2.1. INTRODUCTION TO WIND POWER RAMPS

Although the wind can provide a sustainable source of energy, its temporally fluctuating nature is a serious challenge to the safety and stability of power grids [26] as wind power penetration increases. Rapid increases or decreases in wind power production, commonly known as wind power ramps, can cause problems for electricity networks, such as power outages [27, 28] and challenge the availability of limited reserve power [28]. In 2008, a ramp-down event was reported in the State of Texas causing serious economic loss to the grid operated by the Electric Reliability Council of Texas (ERCOT) [29].

During a decrease in wind power production, i.e. a ramp-down event, a grid operator has to compensate for the loss of power generation by instigating the ramping up of other online generation incurring increased costs to the grid. Moreover, wind farms are sometimes curtailed during a rapid increase in wind power when that power is surplus to requirements. In many cases, wind farm owners are requested to cover additional costs when they are unable to meet specific loads and quotas. Therefore, the generation of electricity systems must match the load to operate reliably. In real-time operations, the system must always keep a maximum capacity that is larger than the expected load to overcome the sudden loss of any generating unit.

The temporally fluctuating nature of wind power occurs due to the influence of wind speed changes driven by changing circulation patterns [15]. These patterns are in turn dependent on land-atmosphere-ocean interactions at various scales. Therefore, the strength of wind power ramps and volatility of wind power depends on the characteristics of mesoscale and large-scale circulation patterns. Understanding these characteristics and how they may change due to a changing climate will therefore give valuable insights into the nature of wind power production and wind power ramps in the present and future.

Temporal variations in wind power can influence short-term power regulation, load following and day-ahead scheduling (Figure 2.1). With current plans to install a large amount of wind power capacity, understanding swings in wind power production will become important for network operators to manage the integration of wind power into electricity systems.
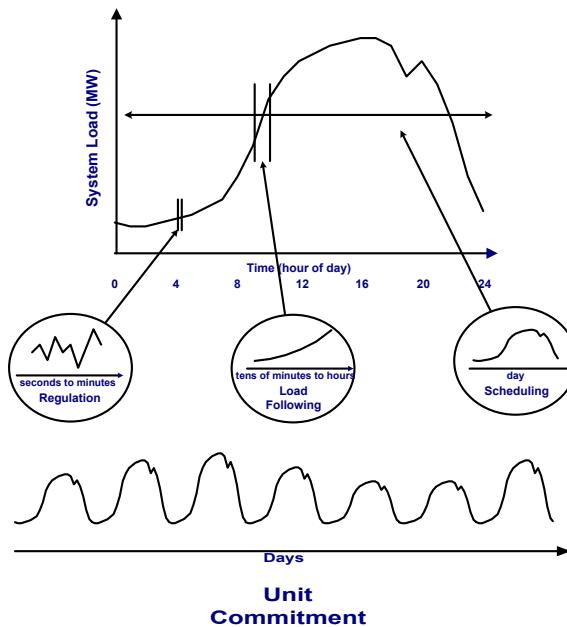
Figure 2.1: Temporal fluctuations in wind power and impact on the dispatch of other generation units [30].

2.1.1. THE CHARACTERISTICS OF WIND POWER RAMPS

In Chapter 3, a new algorithm to detect wind power ramps events is presented, but firstly, in this chapter, the characteristics of wind power ramps are described. Wind power ramps events are categorised based on a number of parameters which relate to a rapid increase or decrease in wind power production [31] as illustrated in Figure 2.2. The characteristics of wind power ramps which are considered relevant in this thesis are:

- Ramp magnitude (ΔP): the magnitude of wind power variation observed during the power ramp event.

- Ramp duration (Δt): the period of time over which the wind power ramp occurs.

- Ramp rate ($\Delta P/\Delta t$): is derived from the previous variables (ΔP, Δt)) and provides a measure of the ramp intensity.

- Ramp time (t_o): the time at which a ramp occurs. This can be defined either as the starting time or mid-point of the event.

- Ramp direction: whether the ramp event represents an increase (ramp up) or a decrease (ramp down) in wind power production.

Identifying these wind power ramp event characteristics is not straightforward given the different temporal scales of wind power fluctuation (e.g. minutes, hours, days) [30].
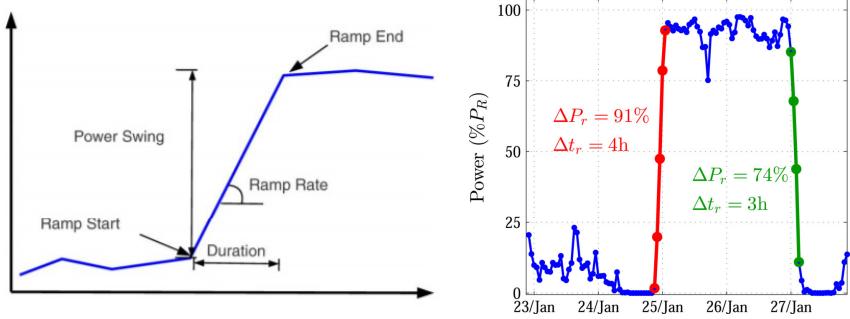
Figure 2.2: (a) Power ramp characteristics [32], and (b) an example wind power ramp with ramp magnitude and duration shown [15].

2.1.2. WIND POWER RAMPS DETECTION ALGORITHMS

Power ramps detection algorithms have been developed to detect the occurrence of ramps events based on their characteristics as defined in the previous section. But, there is a lack of holistic ramp detection algorithms to detect ramp events over a long period of time with variable ramp magnitude and duration [31, 33]. Though it is possible to identify power ramp events easily through visualisation over a short period of time, it is more difficult to identify them over a longer period of time. In Table 2.1, the prominent ramp detection algorithms are summarized where the methods are broadly categorized into: the change of wind power over a defined period relative to rated power, wavelet-transform and Optimized Swinging Door Algorithm.

Table 2.1: Wind power ramps detection algorithms

Algorithms	P_R (MW)	ΔP	Δt	resolution	Author
Threshold	65	65%	1h	10-min	[34]
	65	75%	3hrs	Hourly	[34]
	1,200 - 8,900	–	–	hourly	[35]
	1000	10%	1h	–	[36]
	3 - 240	50%	4hrs	–	[37]
	–	20%	1h	–	[38]
	–	50%	–	–	[39, 40]
	–	50%	2h	–	[41]
	–	15%	1h	–	[41]
Wavelet	–	–	–	–	[42–45]
Optimised swinging door algorithm	–	–	–	–	[46, 47]

2.2. METEOROLOGICAL PHENOMENA

Meteorological phenomena range from minutes to months in terms of temporal resolution, and have spatial coverage from meters to thousands of km as shown in Figure 2.3. They can be classified as microscale, mesoscale or large-scale atmospheric phenomena, and play a significant role in the formation of wind power ramps as shown in Figure 1.3. Small scale atmospheric phenomena, i.e. micro-scale to meso-scale, play a role in the formation of short-duration wind power ramps. Whereas wind power ramps that are characterised by a long duration often occur due to the prevalence of large-scale atmospheric phenomenon such as frontal, high-pressure or low-pressure systems. Meteorological systems that evolve over time thus play a significant role in the nature and occurrence of power ramps [48].
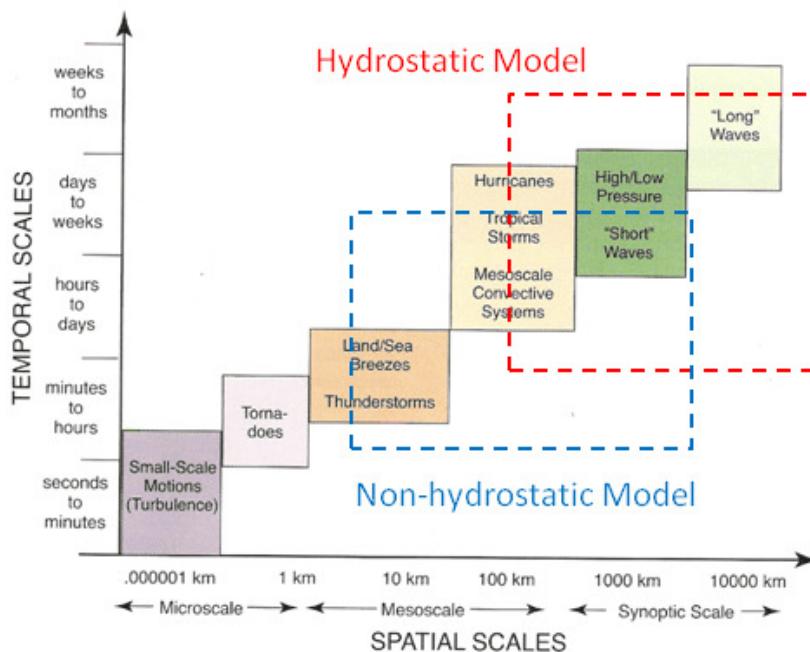
Figure 2.3: The spatial and temporal scales of different meteorological phenomena [49].

2.2.1. MICROSCALE PHENOMENA

Microscale phenomena include small dust devils, thermals, and turbulent eddies. They occur on very short-time scales that range from a few seconds to minutes, and their average scale ranges from less than a meter to a couple of kilometers. The wind speed at the microscale is determined by prevailing local pressure gradients, centrifugal, and fric-

2

tional forces. At the microscale, atmospheric processes are dominated by the underlying surface conditions and energy exchanges in the lowest portion (<1km) of the planetary boundary layer (PBL). The PBL includes: (1) a turbulent surface layer, a layer of the PBL that fluctuates with diurnal fluctuations in small-scale turbulence; (2) a roughness layer, a portion of the PBL mostly influenced by terrain and land cover variability; and (3) a laminar layer, a non-turbulent layer of the PBL, extending a few millimeters above the surface [50].

Surface friction from obstacles (e.g., urban structures, trees, uneven terrain) and unequal surface heating in the PBL produce small-scale eddies and irregular wind patterns known as turbulence. Mechanical (friction-induced) and thermal (heating-induced) turbulence influence local wind shear and wind veer which are changes in wind speed and wind direction, respectively, with height. In the PBL, thermals (rising warm air plumes) and short-lived vortices may develop. As a rising column of air encounters obstructions, it can twist into a small rotating column (with a scale of typically a few meters). These small-scale phenomena occur over a short period of time and thus influence wind power production and wind power ramps over a similarly short time-scale.

2.2.2. MESOSCALE PHENOMENA

Mesoscale phenomena last several hours to a couple of days. Thunderstorms, land-sea breezes, mesoscale convective systems, orthographic waves and squall lines are typical mesoscale phenomena and these can range in scale from 1 to 100km.

Mesoscale phenomena are triggered by either internal or external forcing mechanisms. Internally, mesoscale systems generate their structure and circulation from internal latent heat energy released and the dynamics of local temperature and pressure gradient forces. External forces are the circulation processes either at the micro-scale or large-scale meteorological systems. Large-scale temperature and vorticity advection, and atmospheric disturbances from a non-uniform surface can trigger mesoscale circulation systems [51, 52]. For instance, the uneven heating between land and water bodies can generate a regional pressure difference leading to a sea-breeze or land-breeze circulation, and the atmosphere is under non-hydrostatic equilibrium. Non-hydrostatic atmospheric dynamics are more complex and are usually associated with phenomena like convection, thunderstorms, and other intense weather systems. In these situations, the vertical motion and associated accelerations play a significant role in the pressure distribution and atmospheric dynamics.

Meteorological phenomena that prevail at the range of the mesoscale can therefore influence the temporal fluctuation of wind speed over a longer timescale than those at the microscale. Large-scale complex terrain driven flows, mesoscale convective systems and land-sea breezes are examples of mesoscale phenomena that can influence wind power ramps [18].

2.2.3. LARGE-SCALE SYNOPTIC SYSTEMS

Macroscale weather phenomena or large-scale synoptic systems cover a large area and persist over a relatively long time-scale. Their largest scale is more than 1000km, with a maximum time-scale of several days or weeks. Synoptic systems have a horizontal scale length several magnitudes larger than their vertical depth and can be modelled by as-

suming the hydrostatic approximation, i.e. the pressure variation with height is solely determined by the weight of the overlying air column [53]. Low-pressure systems, cold fronts, low-level jets, and thunderstorm outflows are some of the synoptic-scale meteorological phenomena that can cause ramp-up (increasing wind) events [47, 54]. In contrast, ramp-down (decreasing wind) events tend to occur due to the reduction or reversal of these physical processes [55]. The occurrence of power ramps tends to be associated with particular large-scale atmospheric circulations. Identifying the characteristics of large-scale synoptic systems, using the concept of weather patterns, is considered a valuable tool in better understanding the characteristics and prevalence of wind power ramps. This will be pursued further in Chapter 5.

2.3. WIND POWER RAMP FORECASTING

The temporal variability of wind speed challenges wind power forecasting models in generating reliable and accurate predictions of wind power production and wind power ramps. This is due to the inability of a model to fully capture the complex non-linear dynamics of the weather. The deviation of the forecast wind power from the observed wind power is either due to the limitation of the model to generate the actual magnitude of the wind power or an error in predicting the time or speed of a weather event related to an increase or decrease in wind power. As a result, a model may incorrectly forecast the timing, amplitude, duration or ramp rate of a wind power ramp [36]. This is illustrated in Figure 2.4 which shows a 24 hour ahead forecast of wind power compared with that observed. For example, between 0 – 6 hours, the forecast predicts close to the magnitude of the actual wind power but, the forecast lags what is actually observed. Around 20 – 24 hours, the forecast error is associated with the limitation of the model to correctly predict the magnitude of the wind power increase even though the timing is quite close. Although wind power and wind power ramp forecasting is in general challenging, it may be possible to improve the forecasting skill through combining physical and data-driven models.
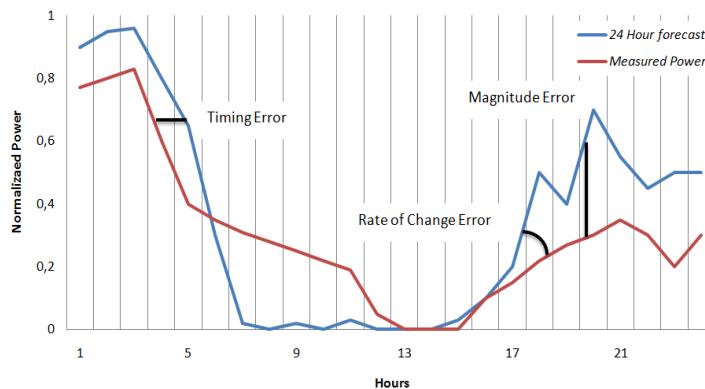
Figure 2.4: A comparison between observed and 24 hour ahead forecast of wind power production inspired by [36] and taken from [31].

2.3.1. PHYSICS-BASED MODELS

A physical model employs a combination of wind turbine parameters and weather information to generate wind power (and thus, wind power ramps) [56, 57]. This wind power forecasting approach uses numerical weather prediction output of wind speed and the wind speed is converted to wind power using a turbine power curve. Running numerical weather prediction (NWP) models is complex, expensive (computationally) and challenging. Some of the challenges related to NWP forecasting are predicting terrain-modulated flow, model initialization, physical parameterization, accurate representation of lower-boundary conditions, and the implementation of numerical methods for solving continuous equations on discrete grids [58]. Surface layer, planetary boundary layer (PBL), land surface, cloud microphysics and cumulus parameterizations are just some of the factors that influence the accuracy of NWP model-driven wind power forecasts [59].

NWP relies on mathematical equations that describe the physics and dynamics of the atmosphere. These equations include the laws of fluid motion, thermodynamics, and the conservation of mass, momentum, and energy. The models are often represented as systems of partial differential equations. To initialise the models, NWP incorporates observed data into the simulations through a process called data assimilation. This involves combining real-time weather observations from various sources, such as satellites, weather stations, and radars, with the model's initial conditions to create the most accurate representation of the current state of the atmosphere. NWP models also divide the atmosphere into a three-dimensional grid, with each grid point representing a specific location in space and time. The equations are solved numerically on this grid to calculate how the weather variables evolve over time. The grid resolution varies, with finer grids providing more detailed predictions. NWP is also frequently used to downscale coarse-resolution climate models to a finer-scale using, for example, mesoscale models, enabling more accurate predictions for specific regions. By considering local topography, land use, and other factors, downscaling provides detailed information about temperature, precipitation, wind, and other weather variables that can be used for a range of applications, including wind power forecasting.

2.3.2. DATA-DRIVEN MODELS

Data-driven methods are commonly used to post-process NWP model output to improve its accuracy based on either linear or non-linear approaches. In recent times, non-linear machine learning-based approaches such as neural networks have shown promise in this regard. A neural network is often simply referred to as an artificial neural network (ANN), and it is a computational model inspired by the structure and functionality of the human brain's neurons. It is a machine learning algorithm that learns from data to perform tasks such as classification, regression, pattern recognition, and decision-making. The multi-layer perceptron (MLP), convolution neural network (CNN) and recurrent neural network (RNN) are some of the commonly used architectures of neural networks which have been used. The algorithms of MLP and CNN are briefly described in the following sections.

MULTILAYER PERCEPTRON

A multilayer perceptron is a simple kind of neural network that consists of an input layer, non-linearly interconnected neurons, hidden layer(s) and an output layer as shown in Figure 2.5. The summation of the neuron weight multiplied by the input data added to the bias passes through a non-linear activation function. This is repeated through each layer, in a process known as *feedforward* (Equation 2.1).
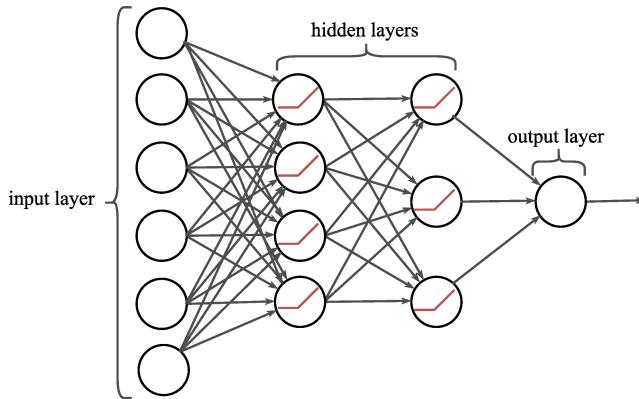
Figure 2.5: MLP architecture [60]. The red line in each neuron represents the form of a non-linear activation function.

Each of the input features (n) are multiplied by the weight of the neurons (W_1, W_2, ..., W_n) that connect the input feature with the neurons where are summed together (Equation 2.1):

$$y = W_1 \times X_1 + W_2 \times X_2 + ... W_n \times X_n + b = \sum_{i=1}^{n} W_i X_i + b \qquad (2.1)$$

The output y is fed into an activation function to get a non-linear output:

$$h1 = \phi \left(\sum_{i=1}^{n} W_i X_i + b \right) \qquad (2.2)$$

The calculations performed in Equations 2.1 and 2.2 are performed for each node and layer of the neural network, moving forward through the hidden layers to the output layer to obtain the output value.

The non-linear activation function allows the neural network model to map the input data non-linearly to the output layer. Some of the non-linear functions that are used in neural network are **sigmoid(σ)**, **tanh**, and **ReLU**:

2

$$\sigma = \frac{1}{1 + e^{-x}}$$
$$\mathbf{tanh(x)} = \frac{e^{x} - e^{-x}}{e^{x} + e^{-x}} \tag{2.3}$$
$$\mathbf{ReLU(x)} = max(0, x)$$

The initialization of the neural network influences the performance of the model. For instance, initializing the weights of the model with zero or a constant value leads to no change in the weight of the neural network. Initializing the weight vectors with a small value slows the model learning rate (vanishing gradients), whereas initializing with a large value can cause the model to diverge (exploding gradients). Thus, careful initialization of the neural network is required for optimum convergence.

To minimize the loss (error) between the model output and the target value, the model goes through several iterations. A *back-propagation algorithm* is used to calculate the gradient loss from the output to the input layer. The goal of back-propagation is to update the weight vectors of the neurons to make the actual output close to the target value, which is discussed further in Chapter 4.

CONVOLUTIONAL NEURAL NETWORK (CNN)

Like a multilayer perceptron, a convolutional neural network (CNN) consists of an input, hidden and output layers. The input to a CNN is in the form of a tensor (e.g. an image). The convolutional layers convolve (filter) the input image, pool (down-sample) the values and pass the result to the next layer (Figure 2.6) to separate and extract different unique features from the input image data. Once a CNN extracts all necessary features, then the extracted features are flattened into one dimension, which is known as a fully connected (FC) layer. The FC layer is akin to that of the MLP consisting of neurons with weights and biases. This type of layer is usually placed before the output layer and multiple such layers form the last few layers of the CNN.
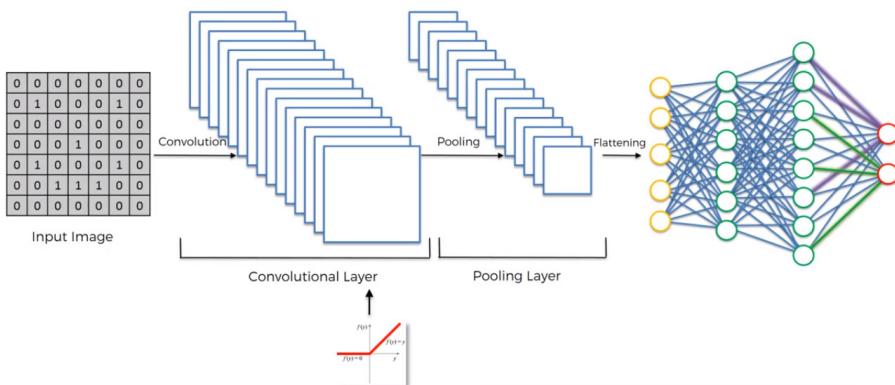
Figure 2.6: Schematic representation of a CNN model[61].

The CNN architecture can vary in complexity. In 1998, the LeNet-5 architecture

was developed which is one of the earliest and most basic of CNN architectures [62]. It consists of seven layers (3-convolutional, 2-average pooling and 2-fully connected). Furthermore, with the advent of deep neural networks, scholars have been refining the architecture and increasing the depth of the CNN model. Some well-known and common image recognition CNN architectures are ALexNet[63], VGG16 [64], GoogleNet [65] and ResNet[66] amongst many others. These models have 8, 16, 22 and 34 layers, respectively. In addition to the number of layers in the models, the architectures of the models have advanced; some of these model architectures such as ResNet and GoogleNet (Inception network) are presented in Chapter 4.

2.4. CLIMATE CHANGE

Climate is defined as the long-term average and/or degree of variability of weather over a defined temporal and spatial scale [67]. The earth's climate has been changing over its 4.5 billion year life. Changes in the earth's climate can be caused by several factors. These include natural factors such as volcanic eruptions, changes in the earth's orbit and shifts in the earth's crust (plate tectonics) or anthropogenic factors such as the burning of fossil fuels since the industrial revolution in about 1800 which is causing an increase in the global average temperature [68].

When comparing the different factors that contribute to climate change, anthropogenic factors have been estimated to have contributed to a global surface temperature increase of 0.85°C between 1880 - 2021. This rise in global temperature has been associated with an increase in the global frequency, spatial extent and severity of droughts, floods and extreme weather events [69, 70]. Typical extreme weather events include tropical cyclones, extratropical cyclones and severe storms. A rise in sea surface temperature (SST) and change in jet stream position which have been observed have been linked to the intensity, scale, frequency, seasonality and geographical distribution of extreme weather events [71–73].

Extreme events linked to mesoscale convective storms such as severe thunderstorms with strong hail, tornadoes or high winds can have severe socio-economic costs. A convective mesoscale storm is a strong thunderstorm downburst due to a convective instability which can result in damagingly strong winds. Studies have shown there has been an increase of convective available potential energy (CAPE) which is associated with an increase in thunderstorms in most parts of the USA [74, 75] and Australia [76], and a similar trend was found in Europe for the regions climatologically susceptible to severe weather such as Spain, Switzerland, Austria, Poland, southern Germany, much of Turkey, and Cyprus [77, 78].

With an increase in the global temperature, the frequency and severity of extratropical cyclones, tropical cyclones and mesoscale convective systems will increase in the future. These changes will have an impact on sea levels, and these extreme meteorological phenomena also affect renewable energy resources, for instance, wind power production. Global sea levels have increased but the rate shows variation: 1mm/yr increase from 1900 to 1950, 0.5mm/yr in the 1960s and 3mm/yr by 2000 [79]. These changes are caused by the thermal expansion of ocean water and melting of continental ice sheets and glaciers, and these changes have the potential to affect the renewable energy resources in a future climate mainly offshore wind power.

2

2.4.1. CLIMATE CHANGE IMPACTS ON RENEWABLE ENERGY

Renewable energy (RE) sources play a significant role in mitigating climate change and the provision of cleaner energy for sustainable social and economic development. Bioenergy, solar energy, geothermal energy, hydropower, ocean energy and wind energy are the six main source of RE [80]. To minimize emissions of carbon dioxide, the share of renewable energy for generating electricity has to be increased. However, climate change may challenge the reliability and performance of renewable energy systems [81].

2.4.2. WIND POWER PRODUCTION UNDER A CHANGING CLIMATE

Wind speed (and thus wind power) over Europe has been projected to show an increase over northern and Central Europe, and a decrease in Southern Europe [82–87]. According to [83] the change in projected wind power over Europe (spatially) ranges from -12% (Mediterranean) to +8% (northwestern Europe) over 2020 – 2049 resulting from an ensemble of global climate models under the RCP4.5 climate change scenario. Using different projected climate models, the projected change in wind power (derived from CORDEX data under different RCP scenarios) [84] and downscaled A1B emission scenarios [88] will be ± 20%. The energy density derived from multi-model global model predictions for a range of RCP scenarios also shows both an increase and decrease spatially in the range ± 30%, with an increasing trend over the Baltic region and a decreasing trend over Eastern Europe [89].

A number of studies have looked in more detail in terms of how climate change may affect wind power in the future. Climate related threats to wind power generation are presented in Table 2.2. Table 2.3 shows how the different emission scenarios are likely to affect wind power generation.

Table 2.2: Main climate threats and impacts on wind power generation [90].

Climate threats	Impacts
1. Changes in wind speed	a) Changes in wind speed can reduce generation (as turbines cannot operate in very high or very low winds) [91] .
	b) Within operational wind speeds, output is greatly affected by wind speed, as the energy in the wind is the cube of wind speed [89, 91, 92] and many others.
2. Changes in daily or seasonal distribution of wind	a)It can affect the match between wind energy input to the grid and daily load demand [89, 91].
	b) Seasonal changes can affect the profitability of the plants due to the evolution of price[90].
3. Changes in temperature	a) Increasing air temperatures, as expected with climate change, will lead to slight declines in air density and power output[92, 93].
	b) Drifting sea ice due to ice melting can damage wind turbine foundations offshore [91, 93, 94] and affect operations at wind farms located in Northern latitudes[92].
	c) Changes in extreme cold periods can affect output (e.g., through turbine blade icing) [91]. Ice on turbine blades can affect performance and durability[93, 95].
	d) A rise in temperature might increase operational costs and affect the efficiency of the equipment [82].
	e) Extremely low or high temperatures may affect various components of wind farms [93].
	f) Changes in permafrost conditions may affect road construction and repairs for wind farms [92].
4. Sea level rise	a) Sea level rise could damage offshore turbine foundations in low-lying coastal areas [91] as well as onshore turbines in coastal locations [92].
5. Extreme weather events	a) Any extreme event can damage infrastructure and complicate access [91]. In this regard, hurricanes or storm surges can cause damage to offshore farms[91] and affect the lifespan of wind turbines [92].
	b) The design of the turbine will be affected by expected turbulence intensity, wind shear and transient wind conditions such as wind speed or directional changes [92, 96].
	c) During extremely high or low wind speeds, farms can be shut down [83].
6. Others	a) Changes in vertical wind shear, directional distribution and turbulence intensity are relevant, but difficult to quantify with existing tools [92].
	b) Large-scale circulation and seasonal patterns such as El Ni no/Southern Oscillation may affect wind [97].
	c) Changes in wave activity may affect structural conditions of offshore farms [93].

Table 2.3: Different climate change scenarios and related impacts on projected wind power generation [90].

Scenarios	Reference periods	projection periods	Projection changes	References
$1.5°C$, $2°C$ and $3°C$ based on AR5 RCP4.5 and 8.5	1971 - 2000	The earliest 30-year period when global mean temperature exceeds 1.5, 2 and $3°C$	Reductions in wind energy potential are projected in all countries except Greece. Changes do not exceed 5% except in Portugal, Ireland and Cyprus in the $3°C$ scenario.	[98]
AR5 RCP4.5	1979 - 2005	2020 - 2049	Wind speeds are projected to increase 2 – 4% in Northwest Europe during the summer and winter (production is expected to increase 4 – 8%), while decreases of 3 – 6% are expected for the Mediterranean in the winter (production expected to decrease 6 – 12% for this area and season.	[83]
AR5 RCP4.5 and 8.5	1979 - 2004	2021 - 2050 and 2061 - 2090	A general decrease in wind power density is to be expected in Europe, except in a few locations. The decrease is constant in RCP4.5 and 8.5, but of a greater magnitude in the latter. However, no discernible changes are expected in the Black Sea Area.	[88]
$1.5°C$ (HAPPI Project)	2013 - 2015	Future with $1.5°C$ increase	Potential for wind development will increase in Northern Europe and decrease in Southern Europe but will not jeopardize future generation.	[87]
RCP4.5 and 8.5	1986 - 2005	2016 - 2035, 2046 - 2065 and 2081 - 2100	The general trend is a decrease in wind energy density in Europe, particularly in Eastern Europe (except the Baltic Sea) and the Mediterranean. Variations increase over time and are more pronounced under RCP 8.5. A decrease in spring, autumn and especially in the summer is to be expected, while an increase in winter is predicted.	[89]
RCP4.5 and 8.5	1971 - 2000	2071 - 2100	Overall energy production will remain within ±5% throughout the 21st century. The greatest reductions are expected for the Iberian Peninsula and Italy. RCP8.5 projects changes with enhanced magnitude.	[86]
SRES A1B	1971 - 2000	2031 - 2060 and 2071 - 2100	Changes in wind energy potential are weak or non-significant over a large part of Europe. A decrease is projected for the Mediterranean and an increase on the Baltic Sea	[84]
SRES A1B	1961 - 2000	2001 - 2100	Regarding wind energy potential, an increase is expected in Northern and Central Europe, particularly in winter and autumn. A decrease is predicted in Southern Europe, expect for the Aegean Sea. Changes in wind energy output follow the same pattern but of a smaller magnitude.	[85]

3

WIND POWER RAMPS DETECTION ALGORITHM

By working faithfully eight hours a day you may eventually get to be boss and work twelve hours a day.

Robert Frost (March 26, 1874 – January 29, 1963)

Knowledge about the expected duration and intensity of wind power ramps is important when planning the integration of wind power production into an electricity network. The detection and classification of wind power ramps is not straightforward due to the large range of events that are observed and the stochastic nature of the wind. The development of an algorithm that can detect and classify wind power ramps is thus of some positive benefit to the wind energy community. In this study, we describe a relatively simple methodology using a wavelet transform to discriminate ramp events. We illustrate the utility of the methodology by studying distributions of ramp rates and their duration using two years of data from the Belgian offshore cluster. This brief study showed that there was a strong correlation between ramp rate and ramp duration, that the majority of ramp events were less than 15 hours with a median duration of around eight hours and that ramps with a duration of more than a day were rare. Also, we show how the methodology can be applied to a time series where installed capacity changes over time using Swedish onshore wind farm data. Finally, the performance of the methodology is compared with another ramp detection method and their sensitivity to parameter choice is contrasted.

3.1. INTRODUCTION

IN Chapter 2, several power ramp detection algorithms were described. However, these algorithms have their own limitations in discriminating ramps events. This chapter presents an improved ramp detection algorithm which can detect ramps of arbitrary ramp rate and duration and is insensitive to changes in rated capacity.

Rapid changes in wind speed can cause ramps in wind power production of a wind farm. With plans to install a large amount of capacity in the North Sea, understanding swings in offshore wind farm power production will become important for wind farm and network operators to manage the integration of wind power into the electricity system. In their development of a wind power variability index, [99, 100] distinguish between three different time-scales which are of importance to system operators. The first of these is sub-hourly up to two hours when load following and frequency control is required. The second and that where wind power generation is stated to cause most ramping is for timescales between one hour and around 15 hours. For these time-scales, there can be significant impact on thermal plant start-ups and shut-downs, though this depends on the characteristics of the plant installed in the particular power system. The final ramping timescales of relevance are between 10 hours and around a day. This is of relevance where large scale storage is required such as hydro pump-storage. An understanding of the prevalence and magnitude of ramps across a range of timescales is thus important.

There is no accepted definition or classification of wind power ramps except that they are manifested in terms of a significant change in production over a relatively short time. The quantification of the duration and magnitude of wind power ramps has been explored by several scholars. Most of the studies set thresholds with respect to the rated power of the wind farm to detect wind power ramps. One such definition [46, 101] defines a ramp as a minimum change in wind farm output ΔP as a fraction of the rated wind power P_R of the wind farm over a period of time (Δt). Different researchers consider different rates of change to define ramps, for example, [102] define a power ramp

when there is a change in wind power production of 75% of P_R within a Δt of 3hours or 65% of P_R within a Δt of 1 hour. In contrast, [101] define a wind power ramp when there is a change in wind power of 50% of P_R over one hour. Other researchers such as [12] and [103] use yet different percentage changes in wind power and time ranges to define wind power ramps. There have been studies to detect power ramps without using any pre-defined change in wind power relative to rated power and time. An optimized swinging door algorithm was used by [46] to extract ramps where the ramp definition parameters related to power change and timescale could be easily adapted. An optimal method based on scoring functions [47] was used to detect ramps of varying lengths at a US wind farm. These authors used a piece-wise linear trending fit to remove short-term stochastic fluctuations.

Even though there has been a significant body of work to detect wind power ramps, it is clear that there is no precise consensus as to the definition of a ramp. Indeed, it may be necessary to extract information about a range of power ramp events depending on the requirements of the wind farm operator or the utility, as described above. What is required is a robust method which can extract ramps of arbitrary magnitude and duration and to discriminate above the incoherent stochastic noise level. In this chapter, we propose an improved method to discriminate ramp events above incoherent stochastic variations using wavelets. Wavelets have been used in the past to extract ramp events from wind power time series, e.g. [42–45].

In this chapter, we build on this work by demonstrating how a wavelet transform can be used in conjunction with the generation of wind power surrogates to give a robust method for the detection of wind power ramps of varying magnitude and duration.

Rather than relying on fixed power or timescale thresholds, the methodology uses a method of discrimination based on statistical thresholds section 3.4. In section 3.2, we illustrate the methodology and its application using data from Belgian offshore and Swedish onshore wind farms. Firstly, we describe the methodology and illustrate its application using a ten-day period of data. Next, in section 3.5, the sensitivity of the discrimination of ramps from natural stochastic variation is investigated using a longer period to generate the surrogate distributions. Then, in section 3.6 we show the utility of the approach in terms of characterising the distribution of ramp rates, their duration and diurnal-seasonal variation using two years of the offshore wind power data. Next, the versatility of the methodology is demonstrated for a non-stationary time-series where installed capacity changes over time in section 3.7. Finally, in section 3.8, we compare the methodology with another commonly used approach, namely the min-max method [12]. The conclusions of the chapter are drawn in section 3.9.

3.2. THE WIND FARM DATA

The Belgian transmission system operator, Elia, makes available 15-minute power output data for the aggregated fleet of Belgian onshore and offshore turbines [104]. In this work, we have used offshore data over a period of two years from 2015 – 2016 when the combined Belgian offshore wind power capacity was 712 MW. For simplicity, the 15-minute values were normalised to the total capacity before analysis to create a time series of values $P(t)$. In addition, we make use of Swedish onshore hourly wind power data for the period 2000 – 2001 aggregated within the SE1 price region [105]. The installed ca-

pacity in this region increased from about 500 MW to 1300 MW over this period. Further details of this data-set can be found in [106].

3.3. WAVELET DECOMPOSITION

Wavelet decomposition, also known as wavelet transform or wavelet analysis, is a mathematical technique used to decompose a signal or data series into different frequency components at different scales. It provides a time-scale representation of the signal, allowing for the analysis of both high and low-frequency components and their temporal localisation.

The continuous wavelet transform (CWT) can be used to decompose a series of data using a mother wavelet function (ψ) by varying its dilation and translation. A mother wavelet function with scale a and position b can be defined as [107]:

$$\psi^{a,b}(t) = \psi\left(\frac{t-b}{a}\right). \tag{3.1}$$

The CWT $W(a,b)$ of a signal $X(t)$ is produced by the convolution of the mother wavelet function over a range of scales and positions:

$$W(a,b) = \frac{1}{\sqrt{a}} \int_{-\infty}^{\infty} X(t)\, \psi\left(\frac{t-b}{a}\right) dt. \tag{3.2}$$

A wavelet transform is thus able to localise the scales of a series of data in time, which makes it a useful function to detect and characterise wind power ramps. We use the Daubechies level 1 (Haar) mother wavelet to decompose the time series of power values. This wavelet is useful to detect abrupt changes in a level which might be expected to occur during a ramp event.

Using values over a ten-day period, 27 Jan 2015 to 07 Feb 2015, taken from the Belgian offshore wind power data, a CWT was applied, and the results are shown in Figure 3.1 comparing the original time series (a) with the corresponding CWT values (b). It can be seen that a high magnitude of W corresponds to a strong power ramp. Similar finding has been reported elsewhere [42, 44]. However, what is not clear is what magnitude of W can be considered as a ramp above the incoherent stochastic variations in wind power. In the following section, we consider how to discriminate ramps above such stochastic variations.

3.4. DISCRIMINATION OF RAMP EVENTS

Random shuffling is a technique to generate surrogate data (a synthetic analogue of the original data) from an original time series which preserves limited statistical properties of the original data, namely their distribution. However, it destroys the auto-correlation within a time series. Surrogate analysis helps distinguish between true structures or dynamics in the data and random artifacts or noise. Randomly shuffled surrogates have been used to test for non-linearity in a time series [108]. It has also been used to test for stationarity in temporal data [109–113]. Furthermore, surrogates have been applied
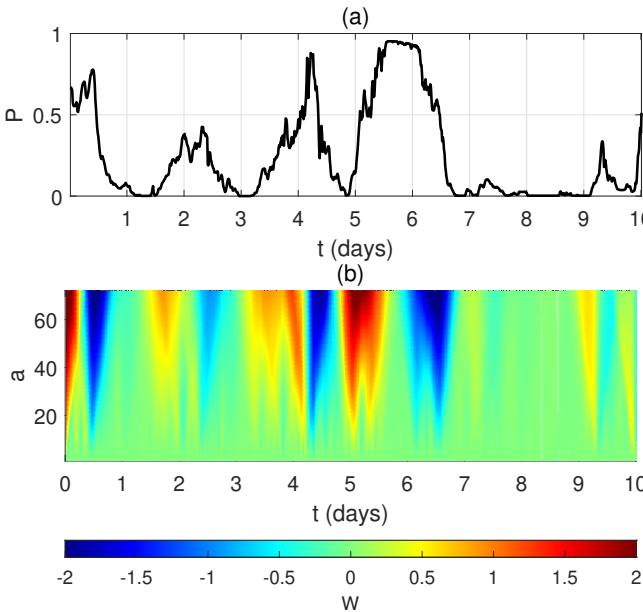
Figure 3.1 (a) aggregated Belgian offshore wind power output over the period 27th Jan 2015 to 7th Feb 2015. (b) continuous wavelet transform of the wind power data using the Haar mother wavelet.

to discriminate gusts and other coherent structures from incoherent noise in high frequency wind speed data [114, 115].

In Figure 3.2, as an example, we analyze a surrogate based on the ten-day time series shown in Figure 3.1(a). Figure 3.2(a) shows a comparison between the auto-correlation of the original time series of normalised power values, $P(t)$ and that of a randomly shuffled time series of these values, $P^*(t)$. It can be seen that any coherent structure in the original data is destroyed. Figure 3.2(b) shows the continuous wavelet transform of the surrogate time series, $W^*(t)$. It can be seen that the lower frequency (higher scale value) structure that was seen in Figure 3.1(b) has disappeared and the power in the transformed wavelet spectrum is much more distributed over all scales.

In order to test the hypothesis that the value of a wavelet coefficient represents a ramp event, we generate 100 such randomly shuffled surrogates of normalised wind power, $P_i^*(t)$, where $i = 1$ to 100, based on the ten days of data. This period was used for easy visualisation of a small number of ramp events. For each surrogate time series, the CWT is generated to give a series of coefficients $W_i^*(a, b)$. These are used to generate distributions of coefficient values (containing $100 \times b$ values) for each scale a, against which the CWT coefficient of the original, $W(a, b)$ can be compared. In Figure 3.3(a) – 3.3(d) we show the distributions for W and W^* at the scale $a = 40$ where we discriminate the W values based on the largest 10%, 5%, 2% and 1% of $|W^*|$ values, respectively. The threshold values, $\pm W_T^*$ are shown for each plot in Figure 3.3.

We then extend this method of discrimination to all the scales of W. So, for each
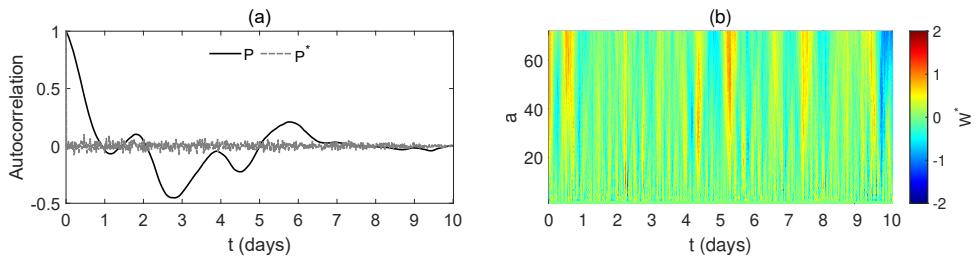
Figure 3.2 (a) the auto-correlations of the original wind power (P) and the normalised wind power surrogate (P^*); (b) the CWT of the normalised wind power surrogate.
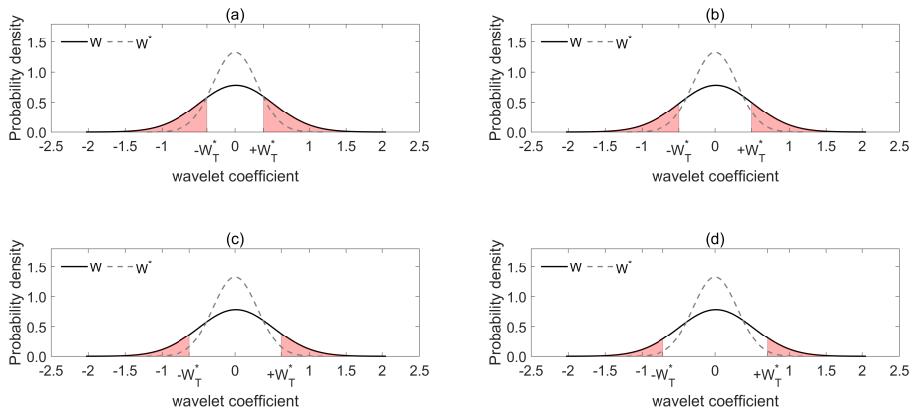
Figure 3.3 The distributions of W and W^* shown at the scale ($a = 40$). The shaded regions show the W values which are classified as ramp events based on thresholds $\pm W_T^*$ set using the highest (a) 10% (b) 5% (c) 2% and (d) 1% of the W^* distribution.

scale a, we compute a scale-dependent threshold $W_T^*(a)$ for a specific discrimination level by utilising the $|W_i^*(a, b)|$ values from all the surrogates. If the value of $|W(a, b)|$ is greater than this threshold $W_T^*(a)$, then the null hypothesis (no ramp) is rejected at the specific discrimination level and the event is assumed to be a wind power ramp. We repeat this for the four different discrimination levels used above, namely the 10%, 5%, 2% and 1% levels.

Figure 3.4 shows the result of using this approach to discriminate the wind power ramps at each scale. The plot is similar to the bottom plot in Figure 3.1, but now values which do not satisfy the criterion to be considered as ramps have been removed and are shown as white with different null hypothesis testing. Only the colour shaded values that satisfy the requirement to be considered as wind power ramps for different discrimination levels are shown.
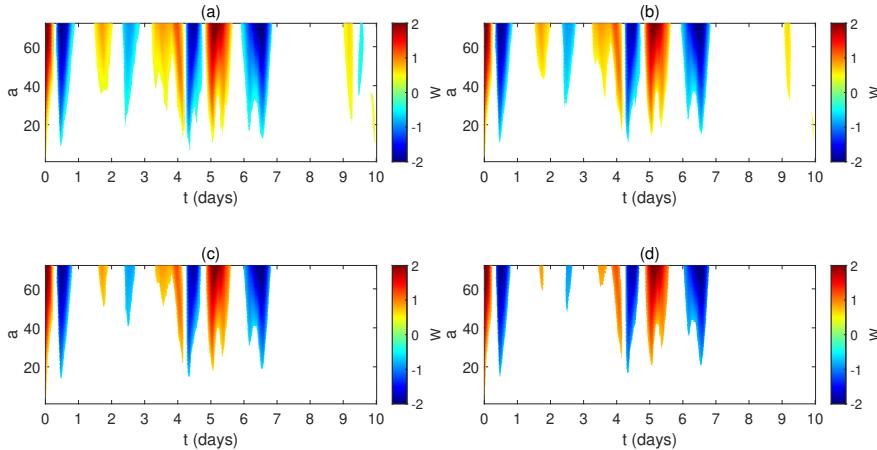
Figure 3.4 The CWT coefficients $W(a, b)$ of the normalized wind power discriminated against the distribution of $W_i^*(a, b)$ using the (a) 10%, (b) 5%, (c) 2% and (d) 1% discrimination levels. The colour scale is blue (ramp-down events), red (ramp-up events) and white (no ramp).

It is then possible to sum $W(a, b)$ over all discriminated scales up to the maximum resolved, a_{max} at each time step, $t = b$ to calculate mean normalised power ramps, $R(t)$:

$$R(t = b) = \frac{1}{a_{max}} \sum_{a=1}^{a_{max}} W_R(a, b)$$ (3.3)

where:

$$W_R(a, b) = W(a, b) \qquad \text{when} \qquad |W(a, b)| \geq W_T^*(a)$$
$$W_R(a, b) = 0 \qquad \text{when} \qquad |W(a, b)| < W_T^*(a)$$

Figure 3.5 shows the original ten-day time series of wind power values with the normalised ramp values, $R(t)$ superimposed. Power ramps are now clearly defined in

terms of both timing and magnitude. Although there is not a large difference in those events which are classified as ramps, in particular, the events on days nine and ten are excluded at the three highest discrimination levels. For the remainder of the chapter, we have chosen the 10% level to provide a good balance between the removal of stochastic variation whilst preserving ramp events that would be of relevance from a power system perspective.
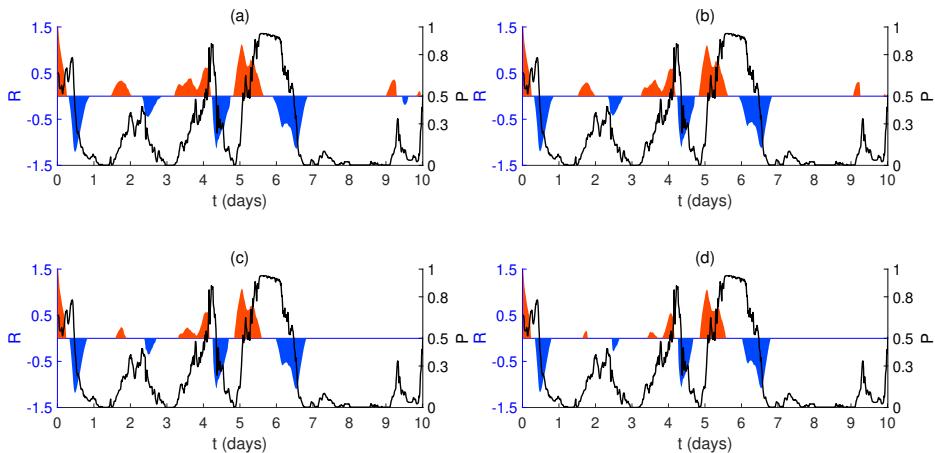
Figure 3.5 Normalised wind power ramps, $R(t)$ is superimposed over the normalised wind power values $P(t)$ for the ten-day period discriminated at the 10% (a), 5% (b), 2% (c) and 1% (d) levels. Ramp-up events are shown in red and ramp-down events in blue.

3.5. SENSITIVITY TO LENGTH OF SURROGATE SERIES

To test the generality of the technique, we consider further testing periods and increase the length of time for which the surrogate distributions are calculated. Three additional ten-day periods are selected and for each period, we examine the sensitivity of the results to the length of surrogate, namely: the same ten-day period and one calendar year of values encompassing the ten-day period. These cases are summarised in Table 3.1.

Table 3.1: Test periods and length of surrogate series used to detect and quantify ramps.

Test Period	Start	End	Surrogate 1 (S_1)	Surrogate 2 (S_2)
T1	28 Jan 2015	7 Feb 2015	Same as test period	2015
T2	20 Nov 2015	30 Nov 2015	Same as test period	2015
T3	27 Jan 2016	5 Feb 2016	Same as test period	2016
T4	3 Nov 2016	13 Nov 2016	Same as test period	2016

As before, for each case, we generate 100 surrogates and the wavelet coefficients $W(a, b)$ are discriminated against the distributions generated using the two different surrogate periods in Table 3.1. The results are presented in Figure 3.6. It can be seen that
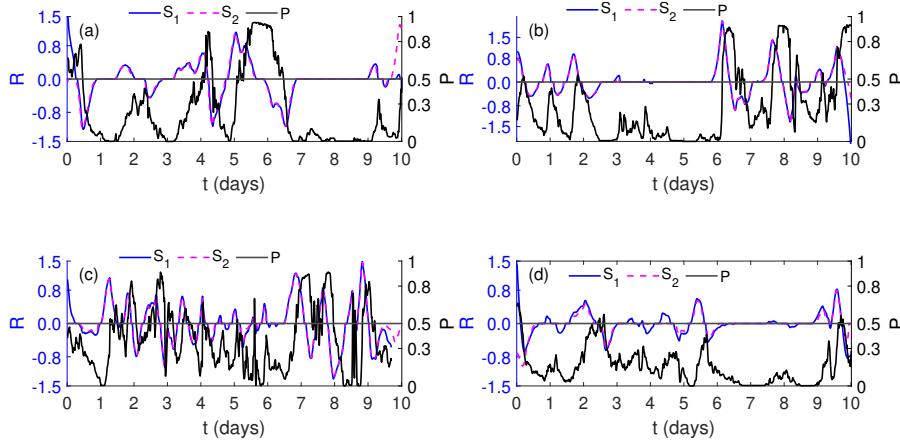
Figure 3.6 Normalised power ramps: (a) period T1; (b) period T2; (c) period T3; and (d) period T4. Normalised wind power is shown in black. The ramp-ups and ramp-downs derived using surrogate statistics from the ten-day period (S1) are shown in blue; and from the one-year period (S2) are shown in purple.

once again, ramp periods are well discriminated from periods of incoherent stochastic variation. In addition, the results show no difference when using a longer period to generate the surrogates except at the very beginning and end of the time series. This is due to boundary effects inherent in using a convolution function which is integrated over all time and should thus be disregarded in any comparison. The fact that the results show no differences when using an extended surrogate period confirms that the process is filtering out short-term incoherent fluctuations and that a ten-day period is sufficient to capture these.

3.6. RAMP RATES AND DURATION

In this section, we show how the methodology can quantify both ramp rates and their duration, using two years of the Belgian offshore wind power data for 2015 – 2016. We also use this two-year period to produce the surrogate distributions for deriving the 10% discrimination level. Firstly, we generate a time series of normalised ramp rates. As can be seen in Figures 3.5 and 3.6, there are discrete periods of ramp-up and ramp-down events. For each ramp-up period k and ramp-down period l we calculate the average ramp-up rate, $R'_u(k)$ and average ramp-down rate $R'_d(l)$, respectively:

$$R'_u(k) = \frac{\sum_{t=1}^{n_k} R(t)}{D(k)} \tag{3.4}$$

$$R'_d(l) = \frac{\sum_{t=1}^{n_l} R(t)}{D(l)} \tag{3.5}$$

where the n_k normalised power ramp-up values $R(t)$ are summed over the duration

$D(k)$ of the kth ramp-up event and the n_l normalised power ramp-down values $R(t)$ are summed over the duration $D(l)$ of the lth ramp-down event.

3.6.1. OVERALL DISTRIBUTIONS

Distribution plots of ramp rates over the entire two year period as a function of duration (binned by hour) are shown in Figure 3.7. The ramp-up and ramp-down event distributions are broadly similar in nature, though there are some features of note:

- There is a strong correlation between the average normalised ramp rate and the duration of the ramp

- The majority of ramp durations are less than 15 hours with a median value of 8.25 hours for ramp-up events and 8.5 h for ramp-down events

- There is a significant spread in ramp rates of duration between two and 15 hours

- For ramps of duration greater than around 12 hours, ramp rates tend to decrease

- There are very few ramp events with a duration of longer than a day (24 hours)

The features described above are logical when considering the nature of the events driving wind ramps which are generally localised in nature and rarely lasting longer than a day, such as the passage of a weather front, a sea breeze [116] or a low-level jet [117, 118].

3.6.2. DIURNAL AND SEASONAL DEPENDENCY

We also investigate whether the ramp rates show a diurnal or seasonal dependence. To do this, we classify ramp-up and ramp-down rates based on their duration: ramps ≤ 2 hrs are classified as short duration; ramps within the range 2 – 15 hrs are classified as medium duration; and long duration ramps are assumed to be ≥ 15 hrs. This classification is somewhat arbitrary but is broadly based on the discussion in Section 3.1.

These results are shown in Figure 3.8. It can be seen that medium duration ramps in particular show a strong diurnal cycle with a higher frequency of ramp-up events in the afternoon and ramp-down events in the morning. This is true to a lesser extent for the long duration ramps. There is no discernible diurnal pattern in the short duration ramps. By contrast, there is no clear cycle at any scale across the different months of year. The observed diurnal variation in medium and long duration wind power ramps is consistent with the pattern of average diurnal generation observed as seen in Figure 3.8(e) which is strongly influenced by mesoscale effects such as low-level jets, land-sea breezes and thermally driven entrainment from aloft due to the relatively close proximity of the Belgian offshore wind farms to the coast. Low-level jets are known to be more prevalent during the evening hours at the location of some of the Belgian offshore wind farms [118] which may contribute to the increase in power generation observed during this period.

These results are based on one dataset for a limited two-year period. Clearly, further work is necessary to investigate the generality of the observations above. However, this short investigation does illustrate how wavelets can be used to investigate ramps rates, their duration and prevalence.
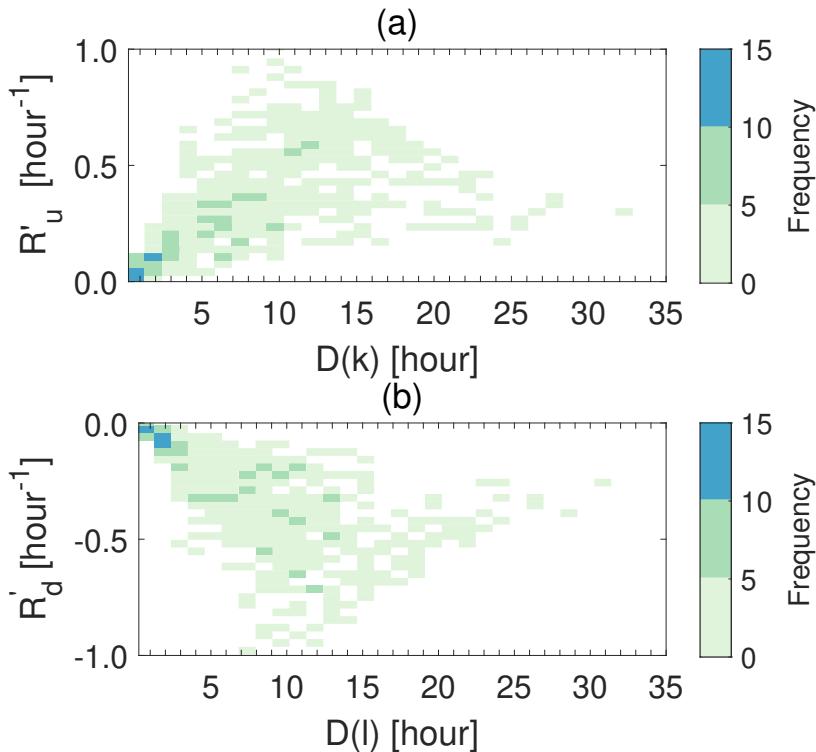
Figure 3.7 Distributions of normalised ramp rates as a function of duration for: (a) up-ramp rates, $R'_u(k)$ and (b) down-ramp rates, $R'_d(l)$.

3.7. RAMP DETECTION DURING A PERIOD OF CHANGE IN IN-STALLED POWER CAPACITY

As a further illustration of the utility of the ramp detection methodology, we apply it to a different time series of wind power data where the installed capacity increases with time. Such a change can be problematic where ramps are defined using a minimum change in wind power output ΔP over a time Δt.

In this section, we use the measured hourly wind power data from the Swedish SE1 price region for the period 2000 – 2001. Figure 3.9(a) shows an increasing trend in the production of wind power which reflects an increase in installed capacity over the two-year period. This trend is also clearly observed in the continuous wavelet coefficient of the power values (P) shown in Figure 3.9(c). Note that in this case, we have deliberately *not* normalized the data to show how the method can be applied when the installed capacity is non-stationary. If the wind power data over the period are randomly shuffled, then clearly the trend is no longer visible in either the surrogate series seen in Figure 3.9(b) or its continuous wavelet transform coefficients W^* as depicted in Figure 3.9(d).

3
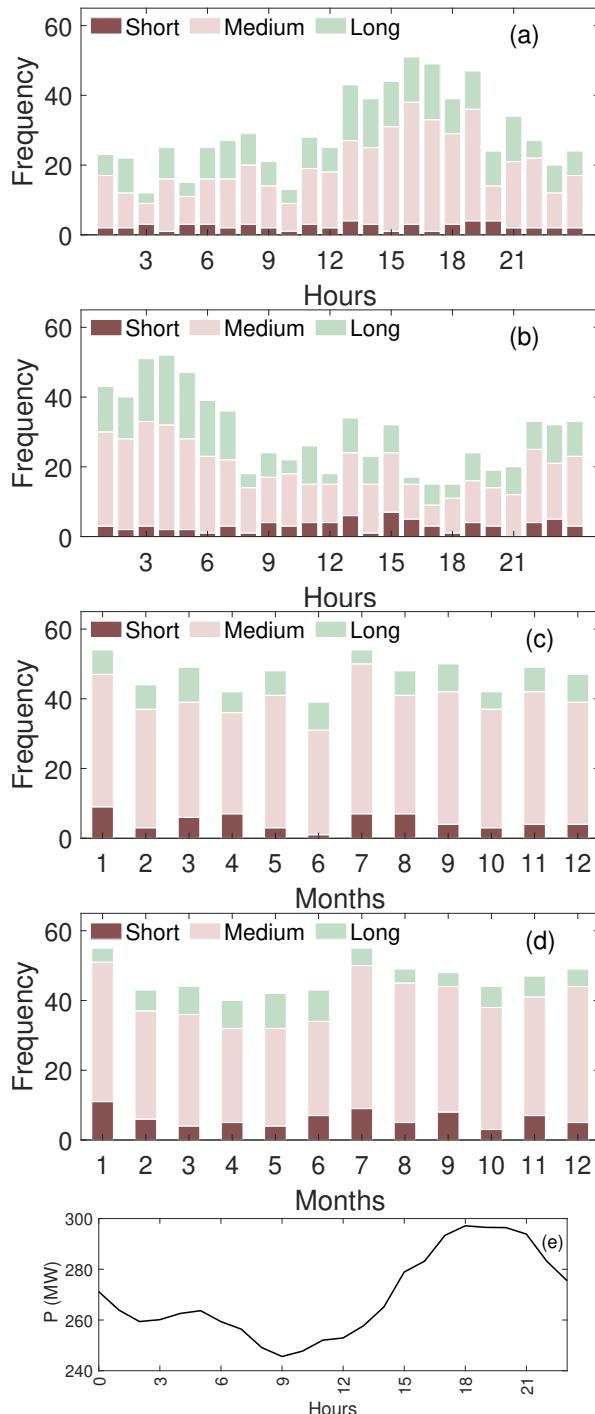
Figure 3.8 Diurnal and monthly frequency ramps events for short, medium and long duration: (a) diurnal ramp-up events; (b) diurnal ramp-down events; (c) monthly ramp-up events; (d) monthly ramp-down events; (e) diurnal variation of wind power.
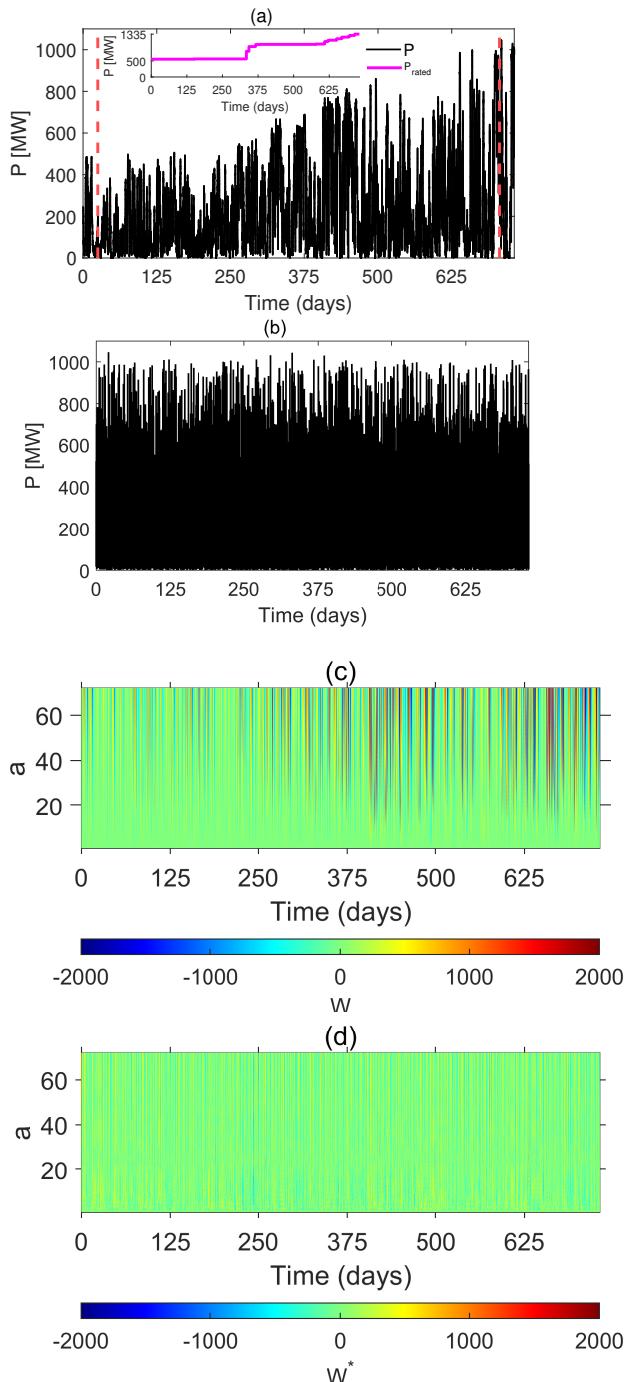
Figure 3.9 (a) hourly wind power production (P) and rated power (P_{rated}) for the aggregated Swedish Energy price region SE1 for 2000–2001. The dash red lines represent two periods studied in further detail (see Figure 3.9); (b) a randomly shuffled hourly values based on the time series in top left; (c) the continuous wavelet transform coefficient of the values in (a); and (d) the continuous wavelet transform coefficient of the randomly shuffled values in (b).

We then focus on two periods of data shown by dashed lines in Figure 3.9(a). In the first period, 01 Jan 2000 to 25 Jan 2000, installed capacity was around 500 MW. In the second period, 06 Dec 2001 to 31 Dec 2001, installed capacity had increased to around 1300 MW. The difference in magnitude of the W values can clearly be seen in Figure 3.10(a) for the first period and Figure 3.10(b) for the second. Then, using the entire period 2000 – 2001 and the method of surrogates to fix the 10% discrimination level following the same methodology as described above, we calculate the power ramps, $R(t)$ for these two periods. Although the values of $R(t)$ are of a different magnitude for the two periods, it can be seen that there is no discernible difference in the ability to detect ramps in the first period, Figure 3.10(c) or the second period, Figure 3.10(d).
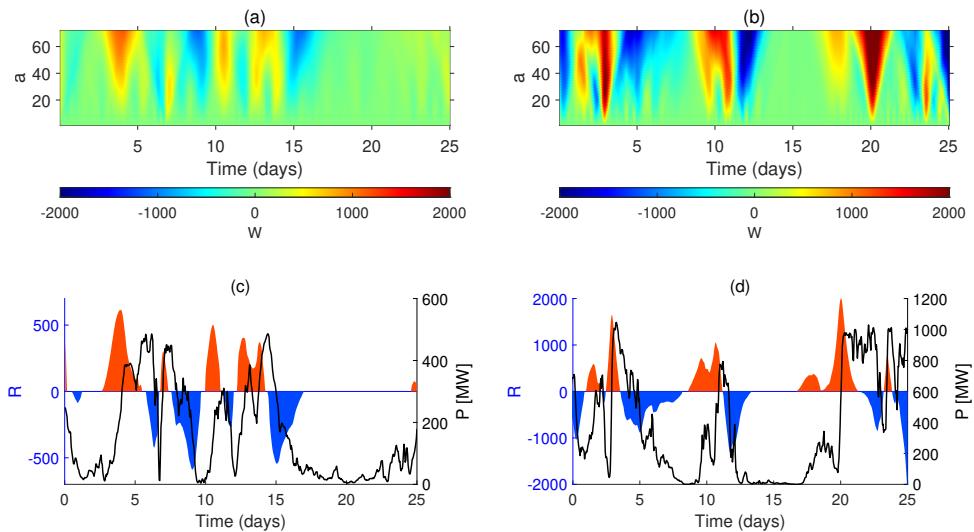
Figure 3.10 Wavelet coefficients and ramps based on wind power for the aggregated Swedish energy price region SE1 for two periods, 01 Jan 2000 to 25 Jan 2000 and 06 Dec 2001 to 31 Dec 2001; (a) continuous wavelet transform coefficient for the period 01 Jan 2000 to 25 Jan 2000; (b) continuous wavelet transform coefficient for the period 06 Dec 2001 to 31 Dec 2001; (c) power ramps for the period 01 Jan 2000 to 25 Jan 2000; and (d) power ramps for the period 06 Dec 2001 to 31 Dec 2001.

3.8. A COMPARISON BETWEEN THE WAVELET-SURROGATE AND MIN-MAX RAMP DETECTION METHODS

Finally, we compare our wavelet-surrogate (WS) method with an existing ramp detection method known as the min-max method [12]. The min-max ramp detection method makes use of a sliding window of a given window length (WL) (in time steps) and considers the change in power during that window defined as the difference between the maximum and minimum power within the window. If this change in power is greater than a defined threshold (TH) then a ramp is deemed to have occurred. Clearly, the sensitivity of this method depends on the chosen values of two parameters, namely WL and TH in

contrast to our WS methodology which depends on a discrimination level. In this study, we compare the two methods in detecting the number of up and down ramps events. This comparison is made for both the Belgian and Swedish wind power data-sets.

Table 3.2 shows the number of ramp-up and ramp-down events that are detected using the WS and min-max methods for different time periods of the two wind power data-sets as a function of different parameter values used by each method. For the WS method, we quantify the sensitivity of ramp detection using the 10% (WS10), 5% (WS5), 2% (WS2) and 1% (WS1) discrimination levels. In the case of the min-max method, we use a combination of window lengths (WL1 = 8 and WL2 = 12) and threshold levels (TH1 = 0.3 and TH2 = 0.4). For the 15-minute Belgian offshore wind power, these WL values correspond to WL1 = 2 h and WL2 = 3 h, whereas for the hourly Swedish onshore wind power data, they correspond to WL1 = 8 h and WL2 = 12 h. Note that the actual Swedish wind power data values are used for the WS algorithm while the data are normalized by time-varying installed power capacity for the min-max method (see Figure 3.9(a)).

In general, the number of ramp events detected by the WS method is greater than for the min-max method. The number of events detected by the WS method generally reduces as the discrimination percentage value gets smaller. The exception to this is for the T1 and T2 periods where a slight increase is seen at the 1% discrimination level when the overall event count is low. This is due to the splitting of single ramp events into two events, an example of which can be seen around day four in Figure 3.5(d). Similarly, the min-max method detects fewer ramp events as TH is increased. By contrast, increasing the WL value does not show such a clear trend in the number of ramp events detected. In addition, the min-max method seems more sensitive to the range of WL and TH values used than for the range of discrimination values used for the WS method.

Table 3.2: Comparison of the (a) wavelet-surrogate (WS) and (b) min-max ramp detection methods. The number of ramp-up and ramp-down events are shown in bold and in parenthesis, respectively. Periods T1 – T4 are given in Table 3.1, T5 is the Belgian offshore wind power data for the entire period 2015 – 2016 and SE1 is the hourly Swedish wind power data for the period 2000 – 2001.

	(a)			
Times	WS10	WS5	WS2	WS1
T1	**6**(6)	**6**(5)	**4**(4)	**6**(4)
T2	**11**(9)	**8**(8)	**8**(7)	**7**(8)
T3	**16**(15)	**14**(13)	**13**(12)	**12**(4)
T4	**10**(12)	**10**(10)	**6**(8)	**5**(6)
T5	**567**(564)	**498**(487)	**434**(430)	**397**(390)
SE1	**237**(244)	**209**(220)	**193**(194)	**179**(182)
	(b)			
Times	WL1, TH1	WL1, TH2	WL2, TH1	WL2, TH2
T1	**4**(2)	**1**(2)	**4**(3)	**4**(3)
T2	**6**(4)	**4**(2)	**7**(5)	**5**(3)
T3	**15**(13)	**10**(6)	**14**(18)	**11**(10)
T4	**2**(5)	**1**(2)	**3**(6)	**1**(4)
T5	**426**(386)	**214**(181)	**527**(467)	**294**(260)
SE1	**185**(179)	**89**(85)	**224**(224)	**132**(139)

3.9. CONCLUSIONS

The detection of wind power ramps is a challenge in terms of how to characterise their magnitude and duration, and how to discriminate a ramp from incoherent stochastic fluctuations in wind power. In this paper, we have presented a relatively simple methodology based on a wavelet transform and the use of surrogates to discriminate and extract ramp events.

Using wind power data from the Belgian offshore wind farm cluster, we have illustrated the application of the methodology and have shown that a ten-day period is sufficient to discriminate coherent ramp events from incoherent fluctuations. We show the utility of the technique in characterising the distribution of ramp rates and their duration, seasonal-diurnal variation for the Belgian offshore cluster. In addition, we have shown how the methodology can be used to detect wind power ramps when installed capacity increases with time, using Swedish onshore wind power data as an example.

Lastly, we compare our ramp detection algorithm with the min-max method, contrasting their sensitivity to parameter choice. Further work is required to apply the methodology to a broader range of sites and for longer periods to investigate the prevalence of different ramp rates and their duration. It might be expected that depending on the climatology of the site that this could differ; on the other hand, consistent trends may be apparent, which could help operators in accommodating fluctuations within an integrated power system.

4

ENHANCING FORECASTS OF WIND POWER AND WIND POWER RAMPS

You cannot create experience. You must undergo it.

Albert Camus (November 7, 1913 – January 4, 1960)

As wind power penetration increases, accurate wind power and wind power ramp forecasting models are increasingly required to help balance supply and demand. This chapter presents the use of deep learning neural network architectures to build such forecasting models based on global numerical weather prediction model data. The reanalysis is used as a benchmark to determine the additional added value of the deep learning neural network in post-processing the coarse resolution of global numerical weather prediction model output data. The performance of the deep learning models in forecasting wind power production and wind power ramps is benchmarked against a simple empirical model.

4.1. INTRODUCTION

As offshore wind power plays an increasingly significant role in generating electricity [119], its time varying behaviour has more of an impact on integration and dispatch of power. Due to this variability, [120], wind power needs to be predicted ahead of time. A wind power forecasting model with sufficient skill can reduce the adverse impacts of wind power variability in an era of high wind power penetration [119]. For this to be achieved, a wind power forecasting model that can accurately capture the statistical and dynamical nature of the atmosphere and forecast wind power production is required. Broadly speaking, wind power forecasting models are classified into physical, and data-driven models. These forecasting models can generate wind power or power ramps individually or in a hybrid form by combining two or more models [121].

Physical forecasting models employ a combination of a numerical weather prediction (NWP) model [56, 57] and some form of transfer function to convert NWP forecast wind speed into wind power. This transfer function normally takes the form of a turbine or farm level power curve. Forecasts can be made for time scales up to days ahead.

Traditional statistical models can be used to improve forecasts from physical models particularly up to a few hours ahead. In this case, either a linear or non–linear regression technique is used based on previous wind power data from an operational wind farm combined with the output from a physical model to produce a short-term forecast [122]. In more recent years, machine learning models have been developed which also use previous wind power data and physical model output, but comprise a more complex modelling process, e.g. a neural network, which can 'learn' the non-linear relationship between input data (observed wind power and NWP output) and future power forecast.

Commonly used neural network models are a multi-layer perceptron (MLP), convolution neural network (CNN), and recurrent neural network (RNN). The general architecture of each model includes an input, one or more hidden layers, and an output layer, where the outputs from each layer pass through a non-linear activation function. A neural network model with one hidden layer is called a shallow neural network [122]. A shallow neural network model has several limitations. It requires "sufficient prior knowledge on the problem domain to manually choose an important input features" [123], and has limitations in the generalization of large data and learning complex patterns [124]. Its use should mainly be restricted to small data sets [125]. A neural network model with more than one hidden layer is known as a deep neural network (DNN) which has been found to be more suitable for learning complex non–linear interactions within a large data set [126].

Neural network models have shown their potential in predicting wind power. For instance, a recurrent neural network (RNN) was shown to outperform an auto-regressive moving average in forecasting wind power [127]. Wavelet transforms have been used to decompose wind speed (and wind power) into different frequency components which are then used as input to neural network models to generate wind power forecasts [120, 121, 128–130]. Hybrid architectures of wavelet-MLP [121], wavelet-CNN [120], and wavelet-Extreme Learning Machines [128] have shown better forecasting performance compared with the models that do not use a decomposed input data using a wavelet-transform. Several studies have been carried out using numerical weather prediction output as an input to a neural network model to generate wind power forecasts e.g. [131–134]. In each case, the neural network was able to improve the site-specific forecast from the NWP model.

Several studies have looked at the ability to forecast wind power ramps. A study compared the wind power forecast generated by a simple power curve using the wind speed forecast by an NWP model (Model I) with a multivariate data-driven model to correct Model I (Model II) [135]. The multivariate model was found to significantly improve the forecasting of wind power and wind power ramps. Recently, [136] used an LSTM and CNN-LSTM architecture to forecast wind power ramps. The hybrid CNN-LSTM outperformed a standard LSTM when predicting power ramps.

This study aims to explore the potential of using neural network models to ingest numerical weather prediction (NWP) model output in order to directly forecast wind power and wind power ramps. The results are benchmarked using a simple empirical model based on a windfarm power curve. The reanalysis is used to provide the closest approximation to the 'ground' truth wind speed. This is done to see to what extent the neural networks improve the forecasts compared with how much they are able to 'downscale' the wind speed and translate it to wind power.

4.2. DATA

4.2.1. MEASURED WIND POWER

This study uses the aggregated Belgian offshore wind power production. Production data are available from the Belgian system operator, Elia [104] and are in the public domain. Belgian offshore wind power capacity has been steadily increasing. In 2016, the rated power capacity was 712.2MW which increased to 2255MW by 2020. For the purposes of this study, the total wind power production is normalized by the total rated power of the wind farms to adjust for changes in the installed capacity. This effectively means that the study will forecast normalized production (between 0 and 1) which is equivalent to the capacity factor of the Belgian fleet. The 15-minute normalized wind power production is aggregated into three-hourly blocks to ensure the same temporal resolution as the global forecast system (GFS) weather model output which is used as input to the neural network models.

4.2.2. GLOBAL FORECAST SYSTEM

GFS is a global weather forecasting model developed by the National Centers for Environmental Prediction (NCEP). The model is initialized at 00, 06, 12, and 18 UTC and

generates weather forecasts for up to 16 days ahead at 1.0°, 0.5°, and 0.25 ° spatial and three-hourly temporal resolution. This study uses GFS data output at the horizontal resolution of 0.25°. For simplicity, the GFS model output initialized at 00 UTC for the first 24 hours of the forecast is used in this study as input to a neural network to generate daily wind power forecasts at three-hourly intervals. Model output wind velocity (wind speed, zonal and meridional) at 100m height and air temperature at 100m and 2m above the surface ground are used as inputs.

4.2.3. ECMWF REANALYSIS V5

The ECMWF Reanalysis v5 (ERA5), the fifth generation ECMWF atmospheric global climate reanalysis, spans the time period from January 1950 to the present. ERA5 is generated by the Copernicus Climate Change Service (C3S) of ECMWF. The ERA5 reanalysis consists of hourly estimates of several atmospheric, terrestrial, and oceanic climate variables. The ERA5 data are available globally at 30km grid spatial resolution. In this study, the ERA5 wind velocity at 100m, the skin surface temperature, and the air temperature at 2m above the ground are employed. In contrast to ERA5, GFS outputs air temperatures at 100m and 2m. The ERA5 reanalysis assimilates more measurements compared with the GFS forecasts and being a hindcast can be considered as a truer estimate of the actual observed values at the site of interest.

4.2.4. TEMPORAL PARAMETRS

In addition to the ERA5 and GFS meteorological parameters, temporal parameters that may have a bearing on the forecast are also used as inputs to the models. The temporal parameters months, days, and hours of the year show cyclic in nature, they are decomposed into cyclic features and input to neural network models. These temporal parameters are translated into two components using sine (Equation 4.1) and cosine (Equation 4.2) transformation functions:

$$x_{sin} = sin\left(\frac{2 \times \pi \times x}{max(x)}\right) \tag{4.1}$$

$$x_{cos} = cos\left(\frac{2 \times \pi \times x}{max(x)}\right) \tag{4.2}$$

where x are either months, days or hours of the years, max(x) are 12, 365 and 24 respectively, and x_{sin} and x_{cos} are the corresponding two-dimensional transformed features.

4.3. METHODOLOGY

4.3.1. EMPIRICAL MODEL

As a simple benchmark, a wind farm cluster power curve is derived to relate forecast wind speed to forecast wind power. Wind speed is grouped into a range of bins and the corresponding wind power is aggregated to generate a power curve. This binning approach is easy to understand and implement, though it has some limitations [137] (e.g. the wind power curve may not be smooth due to the binning process).

In Figure 4.1a, it can be seen that wind speed at grid points closest to the Belgian wind farm cluster shows a strong correlation with measured wind power. To generate the wind

power curve, four grid points (2×2) and 210 grid points (15×14) closest to the wind farm are used, where the areas are shown as R1 and R2, respectively in Figure 4.1a. Wind speeds from each of the grid points within these regions are used to generate cluster wind power curves, partitioning the wind speed values in bins of 1m/s. Figure 4.1b - 4.1e, shows examples of the wind farm normalized power curves based on scatter plots of normalized power output against ERA5 wind speed for each of the four grid points in R1 using data between 2016 and 2019. Note that the power curve at high wind speeds is not smooth due to a lack of data values in this region, a fact noted also by [137].

4.3.2. Neural network models

Neural network (NN) models are a useful tool for capturing and modeling nonlinear processes. In the wind energy field, neural network models have been utilized widely to model and forecast wind energy. This section briefly discusses the multilayer perceptron (MLP), convolutional neural network (CNN), residual neural network (ResNet), and inception network (IN), which are utilized in this study to forecast wind power.

Multilayer perceptron

A multilayer perceptron (MLP) is a basic neural network architecture that consists of an input layer, one or more hidden layers, and an output layer, where each one is comprised of one or several neurons. Through the weight vectors of the neurons, the prior layers are linked to the dense layers that follow. The linked layers are mapped to the output layer using a *feedforward* process where the output y_j^k of each neuron j in a layer k is given by a weighted combination of n input data values x_i

$$y_j^k = \sum_{i=1}^{n} W_{ij}^k x_i + b_j^k \tag{4.3}$$

where W_{ij}^k is the weighting vector and b_j^k the bias for each neuron.

The output of each neuron passes through an activation function ϕ which in this chapter takes the form of a ReLU function

$$\phi(y_j^k) = max(0, y_j^k) \tag{4.4}$$

This feedforward process is repeated for all layers such that the output (after passing through the activation function) acts as one of the inputs to the next layer until the output layer is reached.

In the first training step for the neural network, weighting functions are specified using arbitrary values. A loss value is then calculated as the magnitude of the difference between the model output (which in this paper is a single value) $\hat{y}_m$ and the target value y_m, where m is the sample consisting of the vector of input data values. This is then aggregated over all M samples to give the average loss

$$Loss = \frac{1}{M} \sum_{m=1}^{M} |y_m - \hat{y}_m| \tag{4.5}$$

An update of the neuron weights is then performed by backward derivation, which uses the derivative of the *Loss* function with respect to neuron weight from output to

4
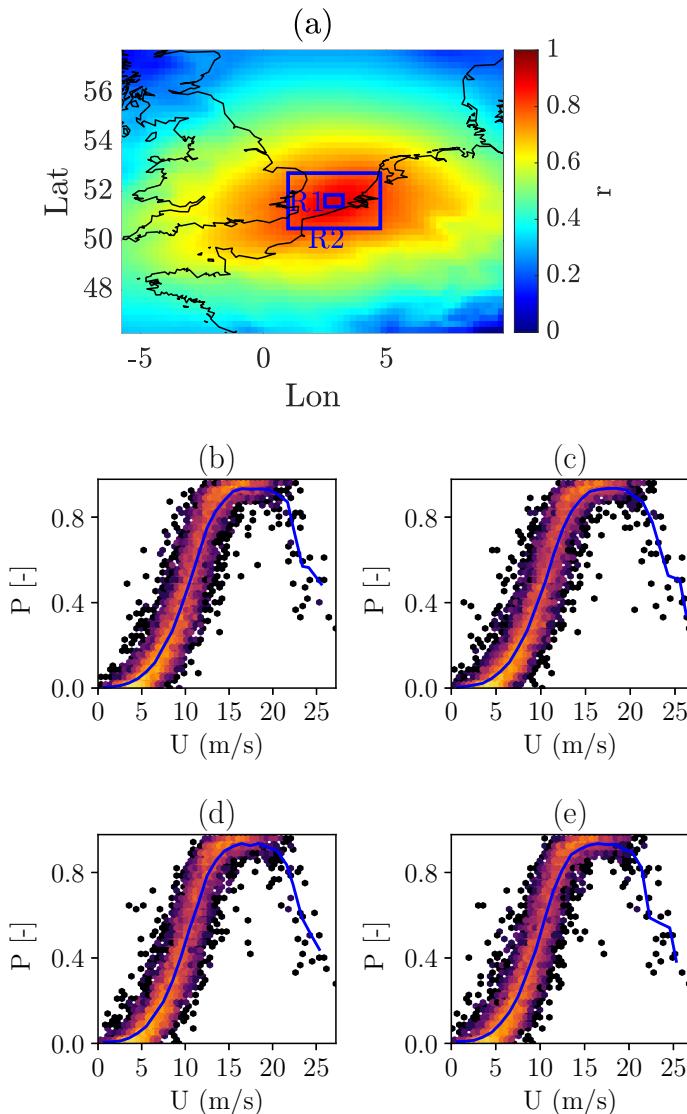
Figure 4.1: (a) correlation of normalized wind power with ERA5 grid point wind speed, and (b) to (e) power curves (blue line) and hexabin log plots of wind power and wind speed values for the four grid points closest to the wind farm fleets (area R1). R1 and R2 rectangles in (a) are the two input regions used in the neural network models.

input layer [138]. This is the reverse of feedforward, and is called a *backpropagation* training algorithm

$$W_{ij}^k(t+1) = W_{ij}^k(t) - \lambda \frac{\partial Loss}{\partial W_{ij}^k}(t) \tag{4.6}$$

where λ is a learning rate, and $\frac{\partial Loss}{\partial W_{ij}}$ is the derivative of the *Loss* function. It is calculated backward from the output layer at training epoch t.

In this study, the *backpropagation* training is performed for several training epochs. After each training epoch, the *Loss* is calculated, and then the model weights are updated.

Figure 4.2 shows five MLP models, MLP1 to MLP5 that are used in this study for the four grid points of wind speed values over the R1 area which is around the wind farm fleets. The figure shows the depth of the models and the number of neurons that are used.
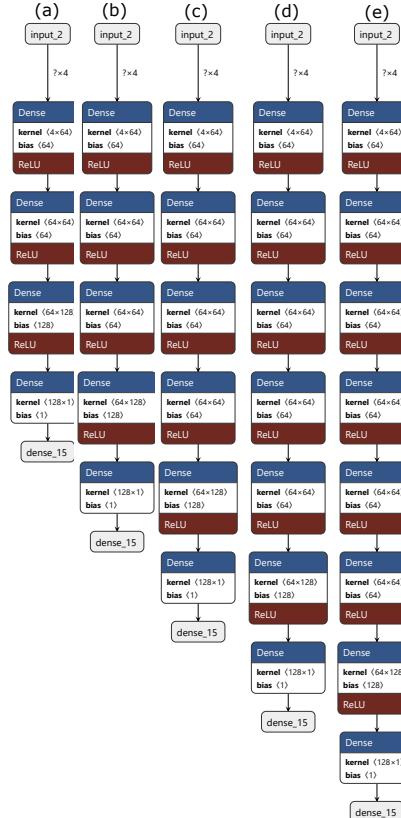
Figure 4.2: The layers of MLP models using U (wind speed magnitude) input over R1 area: (a) MLP1, (b) MLP2, (c) MLP3, (d) MLP4 and (e) MLP5.

4

Convolutional neural network

Unlike the MLP neural network, which uses tabular data, a CNN model operates on spatial data such as a 2D image. A CNN consists of several elements: convolutional filtering, pooling, and fully linked layer(s). The convolutional layer is the main building block of a CNN. A kernel filter extracts essential information by executing convolutional operations across a convolutional window. The extracted features pass through a non-linear activation function to the next layer. The primary purpose of the convolution layer is to extract important features from an input image. A pooling layer usually comes after the convolutional layer in order to downsample the output data from this layer and pass the resulting aggregated information to the next layer. This procedure is used to reduce the spatial size of the input image. A CNN can consist of several such layers. The pooled 2D image from the final layer is flattened into one dimension. This string of values is then fed to a fully connected layer which is similar to an MLP to give the desired output. The architecture of CNN models that are used in this study are shown in the Figure 4.3. CNN1, CNN2 and CNN3 architectures are used to show the sensitivity of the model to the depth of the the CNN layers.

Residual network

As the depth of a neural network increases, the model is vulnerable to accuracy saturation. The model suffers degradation, and information is lost within the deeper layers due to the vanishing gradients problem. Usually, this degradation is not because of overfitting, but rather adding more layers leads to a larger training error [139, 140]. To overcome the training degradation problem in deep models, [66] introduces a deep residual network (ResNet) learning framework. Residual Networks (ResNets) use a different approach to conventional CNNs, where the layers fit a residual mapping (the identity and convolutional block shown in the Figure 4.4a and 4.4c, respectively) rather than being stacked. ResNets utilize "short connections" to skip one or more layers, creating a feedforward neural network architecture. The identity mapping operation of these short connections is combined with the outputs of the stacked layers. Importantly, the use of identity shortcut connections does not increase the computational complexity of the network or introduce new parameters. These ideas are well-described in the literature by various sources [66, 141, 142]. The architecture of the ResNet used in this work to forecast wind power is presented in Figure 4.4b, where the skipping connections are known as "identity mapping" as shown in Figure 4.4a, and the "convolutional block" performs a convolution and batch normalisation before adding the input to the output (see Figure 4.4c).

Inception network

The inception network (IN) was proposed [65] to overcome some of the shortcomings of adding increasing layers and neurons to a conventional CNN, most importantly: 1) susceptibility to overfitting and 2) for the requirement more processing resources. Both of these problems could be resolved by switching from fully connected to sparsely connected topologies inside the convolutional network. The first version of IN architecture was designed to improve the performance of deep neural networks for image classification tasks while minimizing the number of parameters and computations required by using a combination of 1×1, 3×3, and 5×5 convolutional filters in parallel. Later the
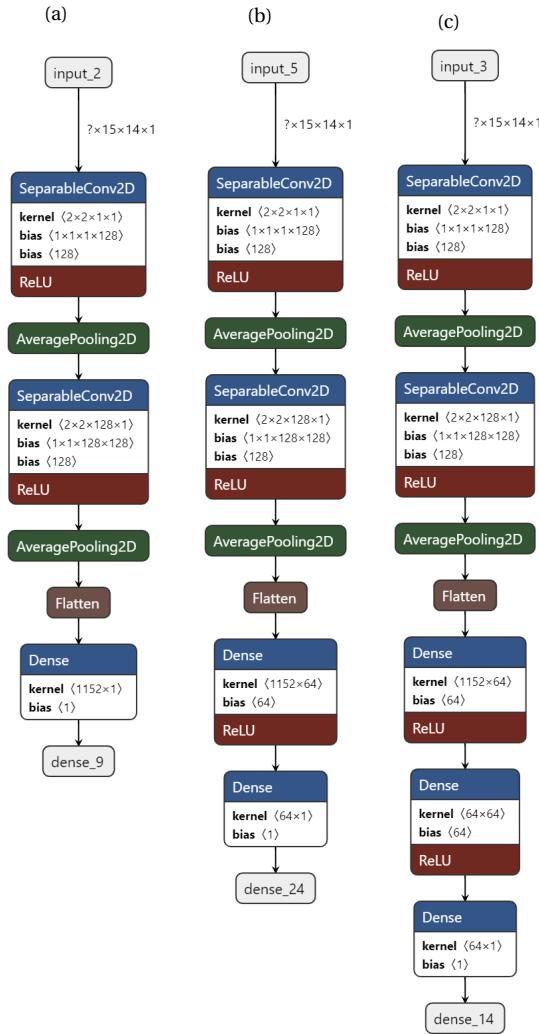
Figure 4.3: The three CNN models architecture used in this study: (a) CNN1, (b) CNN2 and (c) CNN3.
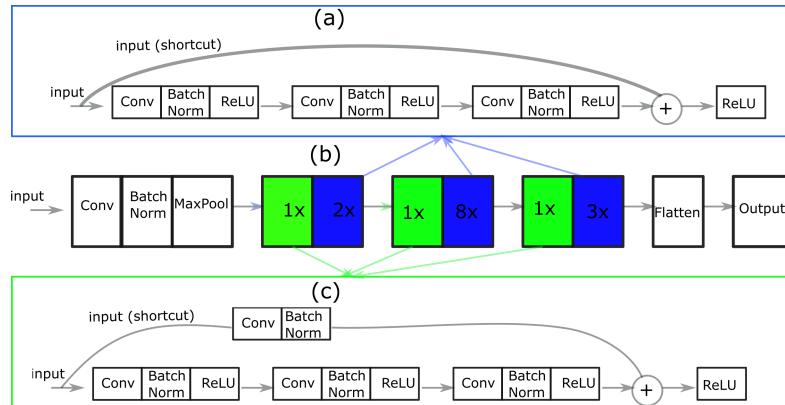
Figure 4.4: ResNet architecture with the components: (a) identity mapping, (b) the overall ResNet architecture, and (c) convolutional block.

Inception-3 version, introduced in 2016, made further improvements to the architecture, including the use of factorized 3x3 convolutions, which are more computationally efficient [143]. The IN architecture uses an inception module (the pink, green, and blue shapes shown in Figure 4.5) to perform parallel convolutional operations of different filter sizes on the input and concatenate the output feature maps, allowing the network to capture information at multiple scales and resolutions.

Figure 4.5 shows the IN that is used in this study which repeatedly filters the input data spatially with a variable filter size, and extracts the associated local and global features. These filter outputs are then concatenated into a single output vector. The output vectors are fed as an input to succeeding levels of the inception architecture, which are layered, allowing an increasing number of units without a significant increase in computational complexity [65].

The inception architecture has been used as a backbone in many state-of-the-art deep learning models for computer vision, including the Inception-v3, Inception-ResNet, and NASNet models. The architecture has shown impressive performance on various benchmark datasets, such as ImageNet, and has helped advance the field of deep learning for computer vision.
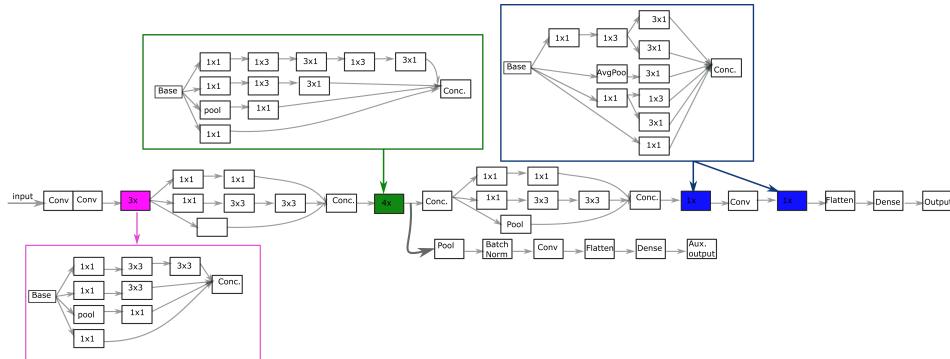
Figure 4.5: The inception network architecture used in this study.

4.3.3. Data pre-processing and model development

Each of the four model architectures described above is used to generate wind power forecasts for the Belgian wind farm cluster. The models use the ERA5 and GFS forecast data from 2016 to 2020 to predict aggregated wind power output. Where ERA5 is assumed to be true ground data.

All the input data that are used by the MLP models are normalized using Min-Max normalization (Equation 4.7) to transform all data to a common scale.

$$X_{norm} = \frac{X - X_{min}}{X_{max} - X_{min}} \tag{4.7}$$

Where X_{norm} is the normalized value of parameter, X is the input parameter, X_{max} is the maximum and X_{min} are the minimum values of the input parameter.

Table 4.1 shows the meteorological and temporal parameters that are used for each of the four models. Two data sets:

- U (wind speed magnitude) and

- U+ (U, x_{sin},x_{cos}, wind speed components (u,v) and ΔT) are used as input.

Where ΔT is the temperature gradient between 100m and 2m for GFS, and the difference between the 2m and skin surface temperature for ERA5. The MLP models use the data from the grid points within the two areas R1 and R2 whereas the image regression models (CNN, ResNet and IN) only use the points within the R2 grid as the number of points within the R1 grid is too small for convolutional filtering.

The 2016 to 2020 datasets for GFS and ERA5 are first spilt into two: 2016 to 2019 for model development, and a testing period covering 2020 to evaluate the performance of the models. Furthermore, the 2016 – 2019 periods are partitioned into training and validation sets as shown in the Figure 4.6. The training set is used to train the model while the validation set is used to monitor the performance of the model (underfitting, overfitting or optimum) by inspecting the training and validation loss versus the training epochs. In each partition, the validation indices are higher than the earlier time to

Table 4.1: MLP and image regression model inputs.

Grids	Models	U	U+
R1/R2	MLP	U	U,x_{sin},x_{cos},u,v,ΔT
R2	CNN	U	U,u,v,ΔT
	ResNet	U	U,u,v,ΔT
	IN	U	U,u,v,ΔT

avoid leakage of data since shuffling time series in cross-validation is inappropriate as shown in Figure 4.6. By dividing the data into five portions, the models are trained and evaluated on different portions of the data to develop multiple forecasting models.
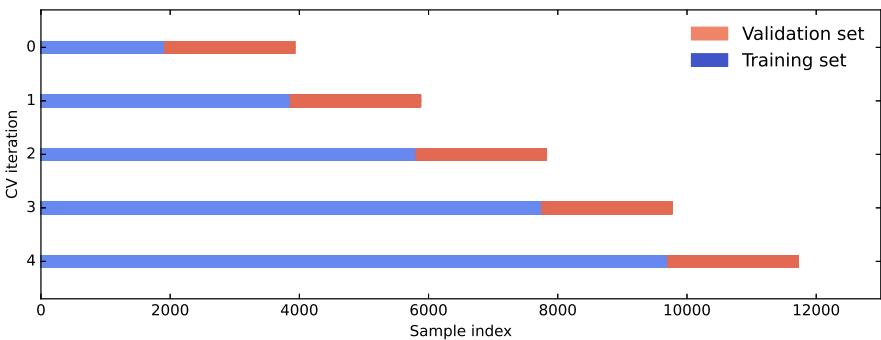
Figure 4.6: Time series data split into training and validation periods during cross validation.

All the models in this study use the Adam optimizer algorithm, which is computationally efficient and requires little memory and typically little tuning [144], with the initial learning rate value of 0.01. The learning rate is further reduced by a factor of 0.2 if no improvement is seen in validation loss for a 'patience' (i.e. number of epochs with no improvement after which training will be stopped) of over five epochs. An early stopping function limits the number of training epochs to stop the training when there is no further improvement in validation loss [145]. The number of neurons/filters in the dense layers are either 64 or 128 for MLP/CNN models. However, the number of neurons in the residual and inception network is less to reduce the number of parameters because of their deep layers and the spatial data used in this study are not complex features. The Glorot normal initializer, also called the Xavier normal initializer, is used to initialize all the models in this study [146]. All the models use the non-linear rectified linear unit (ReLU) activation function [147].

The sensitivity of each model's performance is explored with respect to the number of layers. Five different layer depths are used for the MLP models (Figure 4.2), and three for the CNN models (Figure 4.3). In the case of the ResNet and IN models, only one layer depth is used.

4.4. ERROR METRICS

Root-mean-square error (RMSE), mean absolute error (MAE), mean bias (Bias), and R-squared (R^2) metrics are used to evaluate the performance of the empirical and deep neural network models (Equation 4.9 - 4.11). The lower the RMSE, and MAE metrics are, the better the model. The closer R^2 is to one, the better the model.

$$\text{Bias} = \frac{1}{M} \sum_{m=1}^{M} (y - \hat{y}) \tag{4.8}$$

$$\text{MAE} = \frac{1}{M} \sum_{m=1}^{M} |y - \hat{y}| \tag{4.9}$$

$$\text{RMSE} = \sqrt{\frac{1}{M} \sum_{m=1}^{M} (y - \hat{y})^2} \tag{4.10}$$

$$R^2 = \left(\frac{\sum_{i=1}^{M}(y - \overline{y})(\hat{y} - \overline{\hat{y}})}{\sqrt{\sum_{m=1}^{M}(y - \overline{y})^2}\sqrt{\sum_{m=1}^{M}(\hat{y} - \overline{\hat{y}})^2}} \right)^2 \tag{4.11}$$

where y is the target value, $\overline{y}$ is the mean of y, $\hat{y}$ is the model output and $\overline{\hat{y}}$ is the mean of $\hat{y}$.

4.5. WIND POWER FORECASTS

4.5.1. EMPIRICAL MODEL

As explained earlier, Figures 4.1b – 4.1e showed wind farm power curves generated using ERA5 wind speed for the period 2016 – 2019 for the four grid points in area R1. This process was repeated for the grid points in R2 and furthermore using GFS forecasts for the areas R1 and R2. Then, all the wind farm normalized power curves for each grid were averaged to obtain mean power curves over the R1 and R2 areas, based on ERA5 and GFS wind speeds (four normalized power curves for R1 and 210 for R2).

The normalized power production was also calculated based on the GFS wind speed forecast at t+03hrs, t+06hrs, t+09hrs, t+12hrs, t+15hrs, t+18hrs, t+21hrs and t+24hrs; and the concurrent ERA5 wind speed values for the year 2020 (testing period for the deep learning model in this study). Finally, absolute power was calculated by multiplying the normalized power by the rated power of the cluster at that time. This model is called the empirical (EP) model.

The performance of the EP model is summarised in Table 4.2 for the two different regions and wind speed datasets. All the error metrics show that the EP model based on the smaller R1 region performs significantly better than that based on R2 for the GFS wind power forecasts. Furthermore, as expected, the empirical model based on ERA5 outperforms that based on GFS.

To give further insight into the error spread, the empirical model box-whisker plots of the residual power error (δP based on the observed minus the forecast value) are shown in Figure 4.7. These results confirm the observations above. The inter-quartile

Table 4.2: Empirical model based on the R1 and R2 grids, and ERA5 and GFS. The first value is based on ERA5 as input and the second value (in parentheses) is based on GFS up to 24h ahead. RMSE, MAE and Bias are in units of MW.

Model Type	Grid	Input	RMSE	MAE	Bias	R^2
EMPIRICAL	R1	ERA5 (GFS)	160.2 (193.9)	109.7 (128.7)	-4.6 (1.2)	0.93 (0.91)
EMPIRICAL	R2	ERA5 (GFS)	237.0 (246.0)	195.5 (203.0)	9.4 (15.6)	0.89 (0.88)

range (IQR) of the residual error for forecasts (GFS) based on area R1 ranges from -300 MW to 300MW and for R2 ranges from -600 MW to 600MW. Comparing the values of δP based on ERA5 and GFS, ERA5 shows a somewhat smaller spread as expected. For the remainder of this study, the EP model is based on the R1 cluster power curve only due to its significantly better performance.
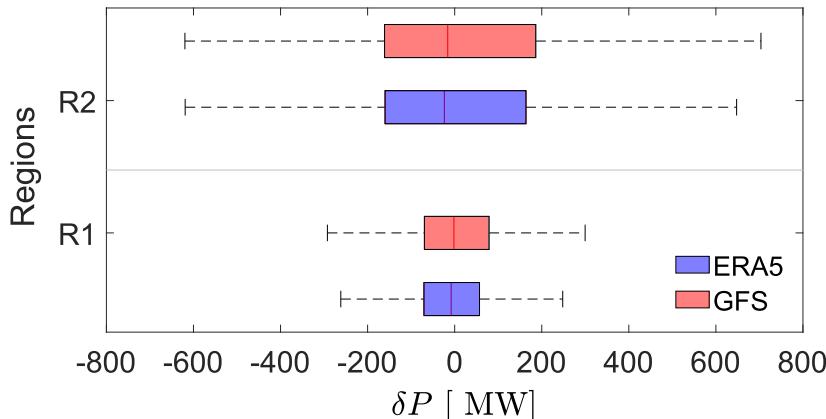
Figure 4.7: The EP model residual wind power errors (δP) based on ERA5 and GFS (forecast up to 24hrs ahead) for R1 and R2 regions. The boxes show the 25th to 75th centile range (the inter-quartile range or IQR). The vertical line within each box represents the median error. The dotted horizontal lines show the 5th to 95th centile range.

4.5.2. NEURAL NETWORK MODELS

The empirical wind power model based on the R1 grid was compared to four different types of neural network model architectures (MLP, CNN, ResNet, and IN), as well as their ensemble mean. Table 4.3 presents the error metrics for all models used to model using ERA5 and forecast wind power using GFS as inputs. Figure 4.8 shows plots of (a) RMSE and (b) MAE by model to allow an easier visual comparison of model performance. Overall, both the empirical and neural network models performed better when using ERA5 as input compared to GFS, with some exceptions. Notably, the neural network model chains M3R1U and RSR2U performed worse with ERA5 than with GFS input, as evidenced by the Bias error.

Furthermore, the performance of the neural network models is compared for dif-

ferent model architectures: grids R1 and R2, parameters U and U+, and input data sources ERA5 and GFS. The neural network model chains using ERA5 outperformed the empirical model in terms of RMSE (with the exception of model chains M1R1U, M3R1U, M4R1U, and M5R1U), MAE, and R^2. Similarly, the neural network model chains using GFS showed better performance than the GFS-based empirical model in terms of RMSE (with the exception of the MLP model chain based on the R1 grid), MAE, and R^2.

When examining the neural network model chain skill with regard to model architecture, grids, and parameters, differences are observed in model performance. For example, the combination of the MLP model using the R2 grid and U+ parameters showed better performance than the MLP model chains using the R1 grid and U in terms of RMSE and MAE. Additionally, the performance of the MLP model is better when using U+ parameters with the same grid. Similarly, the CNN, ResNet and Inception models, and their ensemble mean (IE) performed better than the empirical model, with the ensemble mean (EE) of all model chains (MLP, IE) giving the lowest RMSE and MAE.

4

Table 4.3: Neural network wind power model chains compared with the empirical model. The first value is based on ERA5 as input and the second value (in parentheses) is based on GFS (forecast errors up to 24h ahead). RMSE, MAE and Bias are in units of MW.

Model Type	Architecture	Model code	Grid	Input	Parms	Model Chain	RMSE	MAE	Bias	R^2
EMPIRICAL	M	EM	R1	ERA5(GFS)	U	EMR1U	160.2(193.9)	109.7(128.7)	-4.6(1.2)	0.93(0.91)
MLP	1	M1	R1	ERA5(GFS)	U	M1R1U	160.4(197.9)	105.5(122.4)	-7.4(2.5)	0.94(0.90)
MLP	1	M1	R1	ERA5(GFS)	U+	M1R1U+	154.4(197.7)	103.2(127.9)	-3.7(-4.3)	0.94(0.90)
MLP	2	M2	R1	ERA5(GFS)	U	M2R1U	159.8(198.9)	105.5(124.2)	-4.3(-7.2)	0.94(0.90)
MLP	2	M2	R1	ERA5(GFS)	U+	M2R1U+	152.2(197.5)	102.4(124.0)	5.8(-6.9)	0.94(0.90)
MLP	3	M3	R1	ERA5(GFS)	U	M3R1U	161.2(98.8)	105.8(123.7)	-17.5(-9.0)	0.94(0.90)
MLP	3	M3	R1	ERA5(GFS)	U+	M3R1U+	152.6(197.8)	102.3(124.4)	4.2(-3.7)	0.94(0.90)
MLP	4	M4	R1	ERA5(GFS)	U	M4R1U	160.6(199.9)	105.1(123.9)	-6.5(-8.2)	0.94(0.90)
MLP	4	M4	R1	ERA5(GFS)	U+	M4R1U+	153.1(199.1)	102.4(123.0)	-6.5(-12.3)	0.94(0.91)
MLP	5	M5	R1	ERA5(GFS)	U	M5R1U	161.8(199.1)	105.5(123.1)	-11.3(-7.3)	0.94(0.90)
MLP	5	M5	R1	ERA5(GFS)	U+	M5R1U+	150.3(198.9)	100.0(123.7)	-1.2(-10.8)	0.94(0.90)
MLP	1	M1	R2	ERA5(GFS)	U	M1R2U	156.7(190.4)	101.6(120.3)	-3.1(-26.8)	0.94(0.91)
MLP	1	M1	R2	ERA5(GFS)	U+	M1R2U+	149.3(180.6)	101.6(119.7)	0.1(4.6)	0.94(0.92)
MLP	2	M2	R2	ERA5(GFS)	U	M2R2U	155.2(192.4)	100.8(121.8)	-9.2(-20.1)	0.94(0.91)
MLP	2	M2	R2	ERA5(GFS)	U+	M2R2U+	148.0(182.6)	100.5(118.7)	0.6(3.7)	0.94(0.92)
MLP	3	M3	R2	ERA5(GFS)	U	M3R2U	156.7(189.6)	101.4(120.0)	-7.9(-10.6)	0.94(0.91)
MLP	3	M3	R2	ERA5(GFS)	U+	M3R2U+	147.9(181.6)	100.4(118.6)	3.4(0.6)	0.95(0.92)
MLP	4	M4	R2	ERA5(GFS)	U	M4R2U	156.0(190.1)	101.4(119.4)	-3.9(-12.3)	0.94(0.91)
MLP	4	M4	R2	ERA5(GFS)	U+	M4R2U+	149.5(180.5)	100.0(116.7)	0.6(2.8)	0.94(0.92)
MLP	5	M5	R2	ERA5(GFS)	U	M5R2U	157.7(189.7)	102.6(119.2)	-7.0(-23.6)	0.94(0.91)
MLP	5	M5	R2	ERA5(GFS)	U+	M5R2U+	147.5(179.8)	98.4(115.8)	1.9(6.0)	0.95(0.92)
CNN	1	C1	R2	ERA5(GFS)	U	C1R2U	146.1(186.0)	97.8(118.6)	-4.3(8.5)	0.95(0.92)
CNN	1	C1	R2	ERA5(GFS)	U+	C1R2U+	149.3(175.8)	99.3(113.2)	0.8(-4.8)	0.94(0.92)
CNN	2	C2	R2	ERA5(GFS)	U	C2R2U	147.6(186.5)	96.6(116.9)	-2.4(2.9)	0.95(0.92)
CNN	2	C2	R2	ERA5(GFS)	U+	C2R2U+	147.2(175.3)	97.4(112.0)	-4.3(-0.6)	0.95(0.92)
CNN	3	C3	R2	ERA5(GFS)	U	C3R2U	146.4(188.4)	96.2(117.2)	-4.3(2.9)	0.95(0.91)
CNN	3	C3	R2	ERA5(GFS)	U+	C3R2U+	148.3(176.6)	97.6(110.5)	-5.2(-1.6)	0.95(0.92)
RESNET	S	RS	R2	ERA5(GFS)	U	RSR2U	160.2(189.9)	103.6(117.9)	17.0(5.3)	0.94(0.91)
RESNET	S	RS	R2	ERA5(GFS)	U+	RSR2U+	146.9(176.5)	96.0(111.3)	-5.6(-8.4)	0.95(0.92)
INCEPTION	N	IN	R2	ERA5(GFS)	U	INR2U	156.8(189.5)	100.4(117.5)	8.3(4.5)	0.94(0.91)
INCEPTION	N	IN	R2	ERA5(GFS)	U+	INR2U+	148.0(176.1)	96.3(110.7)	-6.0(1.9)	0.95(0.92)
MLP	M	ME	[R1 R2]	ERA5(GFS)	[U U+]	ME	151.0(180.1)	100.1(113.5)	-4.1(-7.2)	0.94(0.92)
IMAGE	I	IE	R2	ERA5(GFS)	[U U+]	IE	145.1(180.5)	95.8(113.0)	-1.0(-6.1)	0.95(0.92)
ENSEMBLE	E	EE	[R1 R2]	ERA5(GFS)	[U U+]	EE	144.4(178.2)	94.1(112.0)	3.8(-6.8)	0.95(0.92)
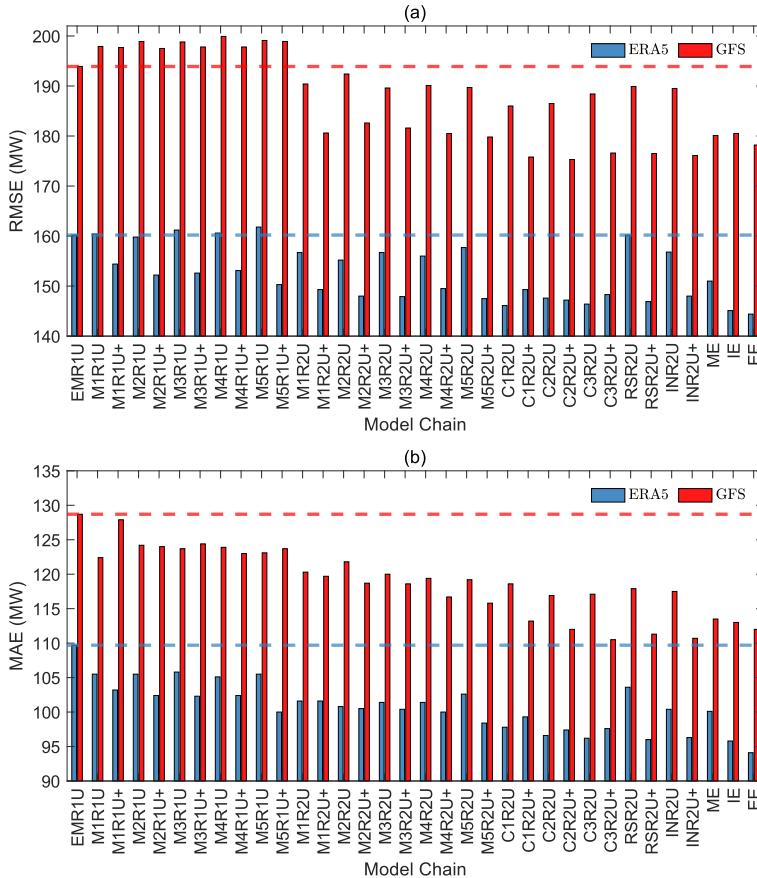
Figure 4.8: Neural network wind power model chains compared with the empirical model: (a) RMSE, and (b) MAE. For ease of comparison, the horizontal dashed lines show the error for the empirical model (EMR1U) using ERA5 (blue) and GFS (red) as input.

4.6. Wind power ramp forecasts

From the wind power model output, wind power ramps are calculated from the change in wind power over a given time period. The power difference is calculated from the observed and modeled wind power output for time increments: Δt = 3hrs, Δt = 6hrs and Δt = 9hrs. For each Δt, the RMSE, MAE, Bias, and R^2 error metrics are calculated by comparing the empirical and neural network models in a similar manner to the absolute power.

4.6.1. Empirical model

The performance of the empirical model is shown in Table 4.4. As expected, the models using ERA5 as input perform better than those using GFS for all values of Δt. RMSE, MAE, and Bias increase for all model chains as Δt increases from 3hrs to 9hrs. As for the absolute power production, the model performs better using the R1 grid (mainly for RMSE and R^2) which is unsurprising given that the ramps are calculated based on differences from the absolute power model.

Table 4.4: wind power ramp errors. The first value is based on ERA5 as input and the second value (in parentheses) is based on GFS (forecast errors up to 24h ahead). RMSE, MAE and Bias are in units of MW. Δt is in units of hours

Model Type	Architecture	Model Code	Grid	Input	Params	Δt	Model Chain	RMSE	MAE	Bias	R^2
EMPIRICAL	M	EM	R1	ERA5(GFS)	U	3	EMR1U3	170.60(199.79)	112.14(162.34)	0.080(-0.011)	0.54(0.41)
EMPIRICAL	M	EM	R1	ERA5(GFS)	U	6	EMR1U6	201.10(241.74)	138.64(162.34)	0.157(0.037)	0.73(0.61)
EMPIRICAL	M	EM	R1	ERA5(GFS)	U	9	EMR1U9	208.66(251.67)	146.74(168.64)	0.120(-0.015)	0.80(0.72)
EMPIRICAL	M	EM	R2	ERA5(GFS)	U	3	EMR2U3	177.06(182.27)	119.31(123.25)	-0.015(-0.026)	0.44(0.40)
EMPIRICAL	M	EM	R2	ERA5(GFS)	U	6	EMR2U6	242.52(252.52)	170.75(176.22)	0.014(-0.008)	0.61(0.57)
EMPIRICAL	M	EM	R2	ERA5(GFS)	U	9	EMR2U9	270.57(282.40)	194.89(201.04)	0.027(-0.006)	0.70(0.70)

Figure 4.9 shows scatter plots of the modelled vs. observed wind power ramps for Δt = 3hrs (Figure 4.9a), Δt = 6hrs (Figure 4.9b) and Δt = 9hrs (Figure 4.9c). The magnitude of the ramp is proportional to the timescale Δt as might be expected. This leads to a larger spread of values and an overall increase in RMSE, but the greater range of values gives a better determination of the regression line and thus an increase in the R^2 value as Δt increases.
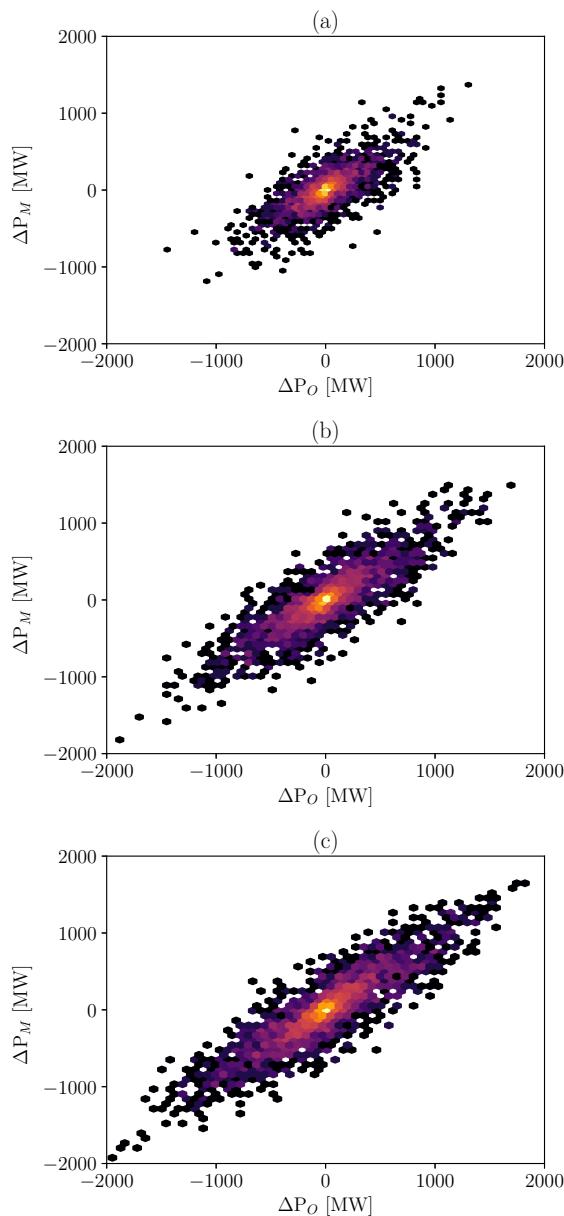
Figure 4.9: Scatter plot of measured (ΔP_O) and ERA5 empirical model (ΔP_M) wind power ramps: (a) Δt = 3hrs, (b) Δt = 6hrs, and (c) Δt = 9hrs.

4.6.2. NEURAL NETWORK MODELS

The wind power ramp metric errors comparing the empirical and neural network models are shown in Table 4.5, 4.6 and 4.7 for Δt = 3hrs, Δt = 6hrs and Δt = 9hrs, respectively. The difference in wind power ramp magnitude is observed as Δt increases. The RMSE and MAE increase as Δt goes from 3hrs to 9hrs, whereas the R^2 value increases.

Overall, when comparing the absolute power with power ramps for ERA5 and GFS (forecast), it can be seen that the correlation is better for absolute power than for ramps, *e.g.* the R^2 for the absolute wind power is in the range 0.94 – 0.95 (ERA5) and 0.90 – 0.92 (GFS), whereas the equivalent values when for ramps are 0.53 – 0.57 (ERA5) and 0.41 – 0.48 (GFS) for Δt = 3hrs, 0.72 – 0.75 (ERA5) and 0.60 – 0.66 (GFS) for Δt = 6hrs, and 0.80 – 0.83 (ERA5) and 0.70 – 0.75 (GFS) for Δt = 9hrs.

The overall performance of the absolute wind power and wind power ramps are similar for the different model chains, but there are some small differences. For the wind power, the ensemble mean of all the models (EE) shows the best performance but the wind power ramp performs best for the MLP model using the R2 grid in terms of RMSE and MAE.

Table 4.5: Wind power ramp errors for Δt = 3hrs. The first value is based on ERA5 as input and the second value (in parentheses) is based on GFS (up to 24h ahead). RMSE, MAE and Bias are in units of MW.

Model Type	Architecture	Model code	Grid	Input	Parms	Model Chain	RMSE	MAE	Bias	R^2
EMPIRICAL	M	EM	R1	ERA5(GFS)	U	EMR1U	170.60(199.79)	112.14(130.80)	0.080(-0.011)	0.54(0.41)
MLP	1	M1	R1	ERA5(GFS)	U	M1R1U	176.83(209.92)	114.49(133.30)	0.087(-0.005)	0.54(0.41)
MLP	1	M1	R1	ERA5(GFS)	U+	M1R1U+	172.22(205.63)	112.94(131.92)	0.047(-0.020)	0.54(0.41)
MLP	2	M2	R1	ERA5(GFS)	U	M2R1U	176.08(210.66)	114.42(133.90)	0.084(-0.005)	0.54(0.41)
MLP	2	M2	R1	ERA5(GFS)	U+	M2R1U+	169.55(206.62)	111.67(132.17)	0.044(-0.023)	0.55(0.41)
MLP	3	M3	R1	ERA5(GFS)	U	M3R1U	177.60(210.14)	114.52(133.15)	0.092(-0.003)	0.53(0.40)
MLP	3	M3	R1	ERA5(GFS)	U+	M3R1U+	170.40(206.82)	111.77(131.84)	0.063(-0.020)	0.55(0.41)
MLP	4	M4	R1	ERA5(GFS)	U	M4R1U	177.52(211.33)	114.68(133.42)	0.930(-0.003)	0.53(0.40)
MLP	4	M4	R1	ERA5(GFS)	U+	M4R1U+	170.44(208.17)	111.53(132.70)	0.034(-0.016)	0.55(0.41)
MLP	5	M5	R1	ERA5(GFS)	U	M5R1U	177.16(211.14)	113.85(133.71)	0.093(-0.003)	0.53(0.41)
MLP	5	M5	R1	ERA5(GFS)	U+	M5R1U+	169.47(208.20)	111.06(132.20)	0.045(-0.032)	0.55(0.41)
MLP	1	M1	R2	ERA5(GFS)	U	M1R2U	167.99(185.47)	108.42(119.33)	0.074(-0.027)	0.54(0.46)
MLP	1	M1	R2	ERA5(GFS)	U+	M1R2U+	159.63(175.94)	105.67(117.69)	0.002(-0.081)	0.57(0.48)
MLP	2	M2	R2	ERA5(GFS)	U	M2R2U	166.84(188.47)	107.94(120.73)	0.074(-0.035)	0.55(0.44)
MLP	2	M2	R2	ERA5(GFS)	U+	M2R2U+	159.53(178.61)	104.98(115.65)	0.010(-0.06)	0.57(0.47)
MLP	3	M3	R2	ERA5(GFS)	U	M3R2U	166.78(188.18)	107.87(119.75)	0.077(-0.034)	0.55(0.45)
MLP	3	M3	R2	ERA5(GFS)	U+	M3R2U+	158.60(178.61)	104.20(115.40)	-0.006(-0.070)	0.57(0.47)
MLP	4	M4	R2	ERA5(GFS)	U	M4R2U	167.63(188.99)	108.53(120.07)	0.078(-0.037)	0.55(0.45)
MLP	4	M4	R2	ERA5(GFS)	U+	M4R2U+	158.41(178.77)	104.03(115.95)	0.004(-0.072)	0.57(0.48)
MLP	5	M5	R2	ERA5(GFS)	U	M5R2U	167.88(187.24)	109.31(120.08)	0.076(-0.034)	0.54(0.45)
MLP	5	M5	R2	ERA5(GFS)	U+	M5R2U+	159.78(179.77)	104.74(115.99)	-0.015(-0.064)	0.57(0.47)
CNN	1	C1	R2	ERA5(GFS)	U	C1R2U	162.13(186.31)	107.42(120.10)	-0.007(-0.006)	0.56(0.45)
CNN	1	C1	R2	ERA5(GFS)	U+	C1R2U+	161.55(178.36)	107.56(116.62)	0.008(0.001)	0.56(0.48)
CNN	2	C2	R2	ERA5(GFS)	U	C2R2U	162.26(187.24)	106.28(120.23)	-0.004(-0.006)	0.57(0.45)
CNN	2	C2	R2	ERA5(GFS)	U+	C2R2U+	161.04(177.82)	106.42(115.54)	0.005(0.003)	0.57(0.48)
CNN	3	C3	R2	ERA5(GFS)	U	C3R2U	162.23(189.14)	105.24(120.25)	-0.006(-0.009)	0.57(0.44)
CNN	3	C3	R2	ERA5(GFS)	U+	C3R2U+	162.43(179.42)	106.59(114.80)	0.025(-0.005)	0.56(0.47)
RESNET	S	RS	R2	ERA5(GFS)	U	RSR2U	170.61(191.24)	109.04(123.44)	0.039(-0.031)	0.54(0.43)
RESNET	S	RS	R2	ERA5(GFS)	U+	RSR2U+	162.77(180.61)	107.37(117.07)	-0.009(-0.061)	0.56(0.47)
INCEPTION	N	IN	R2	ERA5(GFS)	U	INR2U	166.11(187.31)	108.97(120.15)	0.058(-0.033)	0.54(0.45)
INCEPTION	N	IN	R2	ERA5(GFS)	U+	INR2U+	164.21(182.77)	106.88(118.77)	0.023(-0.032)	0.56(0.47)
MLP	M	ME	[R1 R2]	ERA5(GFS)	[U U+]	ME	170.96(184.62)	111.10(118.77)	0.068(-0.032)	0.55(0.47)
IMAGE	I	IE	R2	ERA5(GFS)	[U U+]	IE	159.52(177.97)	104.50(114.69)	0.020(-0.025)	0.57(0.48)
ENSEMBLE	E	EE	[R1 R2]	ERA5(GFS)	[U U+]	EE	164.68(180.35)	107.15(115.50)	0.052(-0.030)	0.56(0.48)

Table 4.6: Similar to Table 4.5 but Δt = 6hrs.

Model Type	Architecture	Model code	Grid	Input	Parms	Model Chain	RMSE	MAE	Bias	R^2
EMPIRICAL	M	EM	R1	ERA5(GFS)	U	EMR1U	201.20(241.74)	138.64(162.340	0.157(0.037)	0.73(0.61)
MLP	1	M1	R1	ERA5(GFS)	U	M1R1U	206.21(252.42)	140.63(165.51)	0.162(0.047)	0.72(0.61)
MLP	1	M1	R1	ERA5(GFS)	U+	M1R1U+	198.51(249.47)	136.12(165.99)	0.098(0.015)	0.74(0.61)
MLP	2	M2	R1	ERA5(GFS)	U	M2R1U	205.59(252.50)	140.60(165.99)	0.153(0.050)	0.72(0.61)
MLP	2	M2	R1	ERA5(GFS)	U+	M2R1U+	195.61(251.87)	134.54(166.11)	0.091(0.015)	0.74(0.60)
MLP	3	M3	R1	ERA5(GFS)	U	M3R1U	206.78(252.94)	140.76(165.69)	0.167(0.056)	0.72(0.60)
MLP	3	M3	R1	ERA5(GFS)	U+	M3R1U+	196.31(249.83)	135.26(165.08)	0.121(0.014)	0.74(0.61)
MLP	4	M4	R1	ERA5(GFS)	U	M4R1U	206.73(254.33)	140.69(166.03)	0.165(0.052)	0.72(0.60)
MLP	4	M4	R1	ERA5(GFS)	U+	M4R1U+	197.10(251.53)	135.29(166.04)	0.077(0.026)	0.74(0.61)
MLP	5	M5	R1	ERA5(GFS)	U	M5R1U	207.45(253.32)	140.27(166.14)	0.163(0.053)	0.72(0.61)
MLP	5	M5	R1	ERA5(GFS)	U+	M5R1U+	195.63(252.27)	134.30(165.65)	0.091(-0.005)	0.74(0.60)
MLP	1	M1	R2	ERA5(GFS)	U	M1R2U	201.59(234.41)	135.52(156.81)	0.147(-0.016)	0.72(0.63)
MLP	1	M1	R2	ERA5(GFS)	U+	M1R2U+	191.76(225.38)	132.09(152.40)	0.013(-0.115)	0.74(0.65)
MLP	2	M2	R2	ERA5(GFS)	U	M2R2U	200.46(237.76)	134.49(158.05)	0.014(-0.024)	0.73(0.63)
MLP	2	M2	R2	ERA5(GFS)	U+	M2R2U+	191.66(229.30)	132.25(154.52)	0.022(-0.074)	0.74(0.64)
MLP	3	M3	R2	ERA5(GFS)	U	M3R2U	201.85(236.98)	135.04(157.33)	0.147(-0.027)	0.72(0.63)
MLP	3	M3	R2	ERA5(GFS)	U+	M3R2U+	191.02(228.53)	131.76(153.52)	-0.007(-0.081)	0.75(0.64)
MLP	4	M4	R2	ERA5(GFS)	U	M4R2U	201.03(237.78)	135.34(157.04)	0.153(-0.037)	0.73(0.63)
MLP	4	M4	R2	ERA5(GFS)	U+	M4R2U+	191.20(227.57)	131.72(153.22)	0.008(-0.106)	0.75(0.65)
MLP	5	M5	R2	ERA5(GFS)	U	M5R2U	201.73(235.99)	135.82(157.36)	0.148(-0.027)	0.73(0.63)
MLP	5	M5	R2	ERA5(GFS)	U+	M5R2U+	192.04(228.14)	131.42(153.20)	-0.009(0.065)	0.74(0.65)
CNN	1	C1	R2	ERA5(GFS)	U	C1R2U	192.31(232.47)	132.61(156.14)	0.020(0.049)	0.75(0.64)
CNN	1	C1	R2	ERA5(GFS)	U+	C1R2U+	194.51(225.06)	134.33(152.27)	0.039(0.055)	0.74(0.66)
CNN	2	C2	R2	ERA5(GFS)	U	C2R2U	193.01(234.46)	131.99(156.36)	0.031(0.037)	0.75(0.63)
CNN	2	C2	R2	ERA5(GFS)	U+	C2R2U+	192.40(224.41)	132.00(151.06)	0.027(0.044)	0.74(0.66)
CNN	3	C3	R2	ERA5(GFS)	U	C3R2U	193.00(236.36)	130.72(156.03)	0.016(0.037)	0.74(0.63)
CNN	3	C3	R2	ERA5(GFS)	U+	C3R2U+	194.03(227.71)	132.83(150.20)	0.067(0.024)	0.74(0.65)
RESNET	S	RS	R2	ERA5(GFS)	U	RSR2U	200.51(238.49)	134.78(158.13)	0.09(-0.028)	0.73(0.62)
RESNET	S	RS	R2	ERA5(GFS)	U+	RSR2U+	196.15(225.22)	133.40(150.89)	0.020(-0.066)	0.73(0.66)
INCEPTION	N	IN	R2	ERA5(GFS)	U	INR2U	200.63(235.26)	137.53(155.56)	0.132(-0.014)	0.72(0.63)
INCEPTION	N	IN	R2	ERA5(GFS)	U+	INR2U+	195.48(230.42)	132.96(153.83)	0.069(-0.004)	0.74(0.65)
MLP	M	ME	[R1 R2]	ERA5(GFS)	[U U+]	ME	196.99(228.83)	134.90(151.46)	0.129(-0.012)	0.74(0.65)
IMAGE	I	IE	R2	ERA5(GFS)	U+	IE	189.89(224.40)	129.92(149.77)	0.064(0.003)	0.75(0.66)
ENSEMBLE	E	EE	[R1 R2]	ERA5(GFS)	[U U+]	EE	191.71(224.94)	131.22(149.21)	0.107(-0.001)	0.75(0.66)

Table 4.7: Similar to Table 4.5 but Δt = 9hrs.

Model Type	Architecture	Model code	Grid	Input	Parms	Model Chain	RMSE	MAE	Bias	R^2
EMPIRICAL	M	EM	R1	ERA5(GFS)	U	EMR1U	208.75(251.67)	146.74(168.64)	0.129(-0.015)	0.80(0.72)
MLP	1	M1	R1	ERA5(GFS)	U	M1R1U	212.66(261.60)	147.51(171.84)	0.127(0.004)	0.80(0.71)
MLP	1	M1	R1	ERA5(GFS)	U+	M1R1U+	203.51(262.53)	142.28(174.94)	0.029(-0.005)	0.82(0.70)
MLP	2	M2	R1	ERA5(GFS)	U	M2R1U	211.99(261.59)	147.49(172.40)	0.118(0.006)	0.80(0.71)
MLP	2	M2	R1	ERA5(GFS)	U+	M2R1U+	200.99(264.15)	140.95(176.00)	0.031(-0.005)	0.82(0.70)
MLP	3	M3	R1	ERA5(GFS)	U	M3R1U	213.17(262.24)	147.72(172.41)	0.135(0.011)	0.80(0.71)
MLP	3	M3	R1	ERA5(GFS)	U+	M3R1U+	201.63(261.80)	141.58(174.55)	0.061(-0.008)	0.82(0.71)
MLP	4	M4	R1	ERA5(GFS)	U	M4R1U	213.21(263.87)	147.67(172.90)	0.132(0.008)	0.80(0.071)
MLP	4	M4	R1	ERA5(GFS)	U+	M4R1U+	201.93(262.48)	141.76(174.38)	0.014(-0.002)	0.82(0.71)
MLP	5	M5	R1	ERA5(GFS)	U	M5R1U	214.53(262.52)	1148.14(172.76)	0.129(0.009)	0.80(0.71)
MLP	5	M5	R1	ERA5(GFS)	U+	M5R1U+	199.64(263.23)	139.91(174.47)	0.026(-0.034)	0.82(0.71)
MLP	1	M1	R2	ERA5(GFS)	U	M1R2U	207.94(249.85)	143.51(168.32)	0.129(-0.069)	0.81(0.72)
MLP	1	M1	R2	ERA5(GFS)	U+	M1R2U+	198.19(242.18)	139.07(166.71)	-0.019(-0.169)	0.82(0.74)
MLP	2	M2	R2	ERA5(GFS)	U	M2R2U	205.74(253.59)	142.20(170.38)	0.122(-0.088)	0.81(0.72)
MLP	2	M2	R2	ERA5(GFS)	U+	M2R2U+	197.89(246.68)	139.72(168.74)	-0.002(-0.104)	0.82(0.73)
MLP	3	M3	R2	ERA5(GFS)	U	M3R2U	207.62(252.18)	143.20(169.20)	0.129(-0.076)	0.81(0.72)
MLP	3	M3	R2	ERA5(GFS)	U+	M3R2U+	196.47(243.64)	138.13(166.26)	-0.040(-0.109)	0.82(0.73)
MLP	4	M4	R2	ERA5(GFS)	U	M4R2U	206.33(252.40)	142.95(168.80)	0.134(-0.083)	0.81(0.72)
MLP	4	M4	R2	ERA5(GFS)	U+	M4R2U+	197.91(242.87)	139.25(165.95)	-0.025(-0.162)	0.82(0.74)
MLP	5	M5	R2	ERA5(GFS)	U	M5R2U	207.82(250.28)	1144.23(168.07)	0.124(-0.089)	0.81(0.73)
MLP	5	M5	R2	ERA5(GFS)	U+	M5R2U+	197.80(241.85)	1138.32(164.8086)	-0.023(-0.087)	0.82(0.74)
CNN	1	C1	R2	ERA5(GFS)	U	C1R2U	195.03(245.37)	137.27(165.57)	-0.023(0.027)	0.83(0.73)
CNN	1	C1	R2	ERA5(GFS)	U+	C1R2U+	199.33(234.86)	140.29(159.97)	-0.006(0.047)	0.82(0.75)
CNN	2	C2	R2	ERA5(GFS)	U	C2R2U	196.90(246.98)	137.32(164.39)	-0.013(0.008)	0.83(0.73)
CNN	2	C2	R2	ERA5(GFS)	U+	C2R2U+	196.06(235.06)	137.48(159.28)	-0.032(0.033)	0.83(0.75)
CNN	3	C3	R2	ERA5(GFS)	U	C3R2U	195.83(249.13)	135.87(165.34)	-0.025(0.014)	0.83(0.72)
CNN	3	C3	R2	ERA5(GFS)	U+	C3R2U+	198.43(237.26)	139.20(158.38)	0.016(0.006)	0.82(0.75)
RESNET	S	RS	R2	ERA5(GFS)	U	RSR2U	205.48(251.69)	141.40(169.46)	0.082(-0.066)	0.81(0.72)
RESNET	S	RS	R2	ERA5(GFS)	U+	RSR2U+	201.99(236.05)	140.14(158.42)	0.012(-0.010)	0.82(0.75)
INCEPTION	N	IN	R2	ERA5(GFS)	U	INR2U	208.37(247.62)	144.86(164.63)	0.122(-0.037)	0.81(0.73)
INCEPTION	N	IN	R2	ERA5(GFS)	U+	INR2U+	198.67(239.82)	1138.19(160.79)	0.025(-0.043)	0.82(0.74)
MLP	M	ME	[R1 R2]	ERA5(GFS)	[U U+]	ME	201.66(240.52)	140.70(160.49)	0.080(-0.053)	0.82(0.74)
IMAGE	I	IE	R2	ERA5(GFS)	U+	IE	193.82(235.45)	135.19(157.75)	0.033(-0.022)	0.83(0.75)
ENSEMBLE	E	EE	[R1 R2]	ERA5(GFS)	[U U+]	EE	195.87(236.16)	136.47(157.56)	0.064(-0.043)	0.83(0.75)

In order to compare model trends, the RMSE and MAE values for the wind power ramp are presented normalised to the corresponding empirical model values as shown in Figure 4.10. For comparison, the corresponding normalised *absolute* wind power RMSE and MAE metrics are shown as dotted lines. The trends are similar, but there are some differences of note:

- The largest gains in accuracy result from using the larger R2 grid. This is true for both the absolute power and ramp, though the gains are larger for the ramp forecasts (GFS), especially for the Δt = 3hrs ramps.

- For both the absolute wind power and ramp, the neural network models using the larger R2 grid and U+ variables as input add more value to the GFS-based forecasts compared with ERA5.

- The MLP models with few layers show the best performance-generating ramps in

terms of RMSE for the Δt = 3hrs ramps, whereas the CNN, ResNet and Inception models show the best performance-generating absolute power. In terms of MAE, the CNN models seem to perform better for the Δt = 3hrs wind power ramp suggesting that the CNN models may not capture extreme ramps as well as the MLP models.

- The differences in model performance between the absolute power and power ramps reduces as Δt increases.

- Ramp forecast model performance as Δt increases deteriorates noticeably using GFS as input from the R2 grid when forecasting using the neural networks. The gains seen relative to ERA5 for Δt = 3hrs have almost disappeared for Δt = 9hrs.
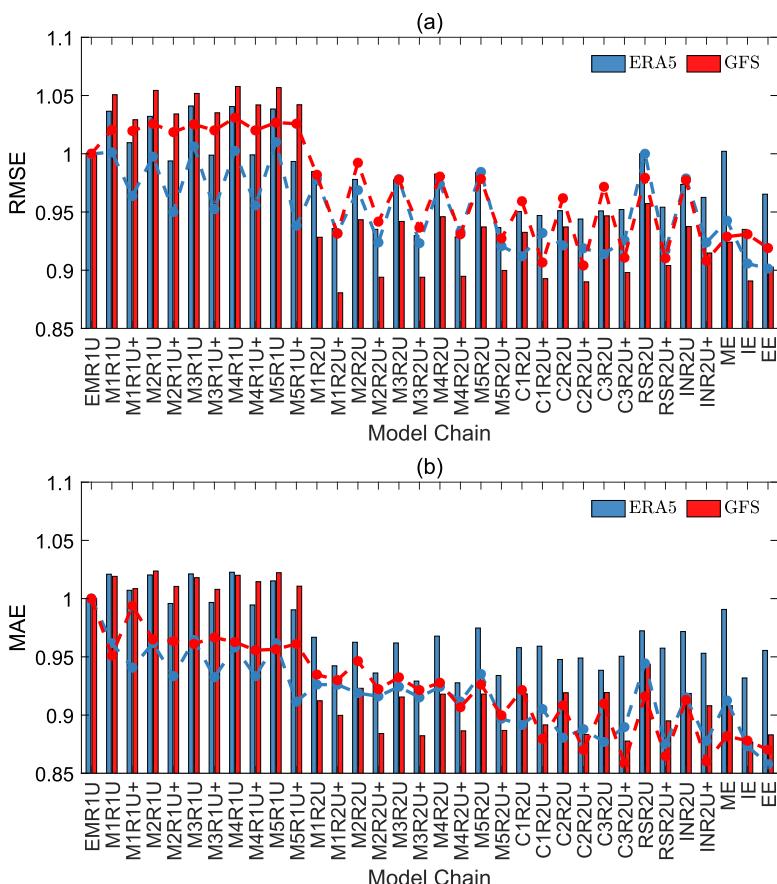


Figure 4.10: The RMSE and MAE of the wind power ramp normalised by the corresponding empirical model values: (a) RMSE, Δt = 3hrs, and (b) MAE, Δt = 3hrs. The horizontal dashed lines in blue (ERA5) and red (GFS forecasts up to 24h ahead) show the normalised absolute wind power RMSE and MAE metrics for comparison.
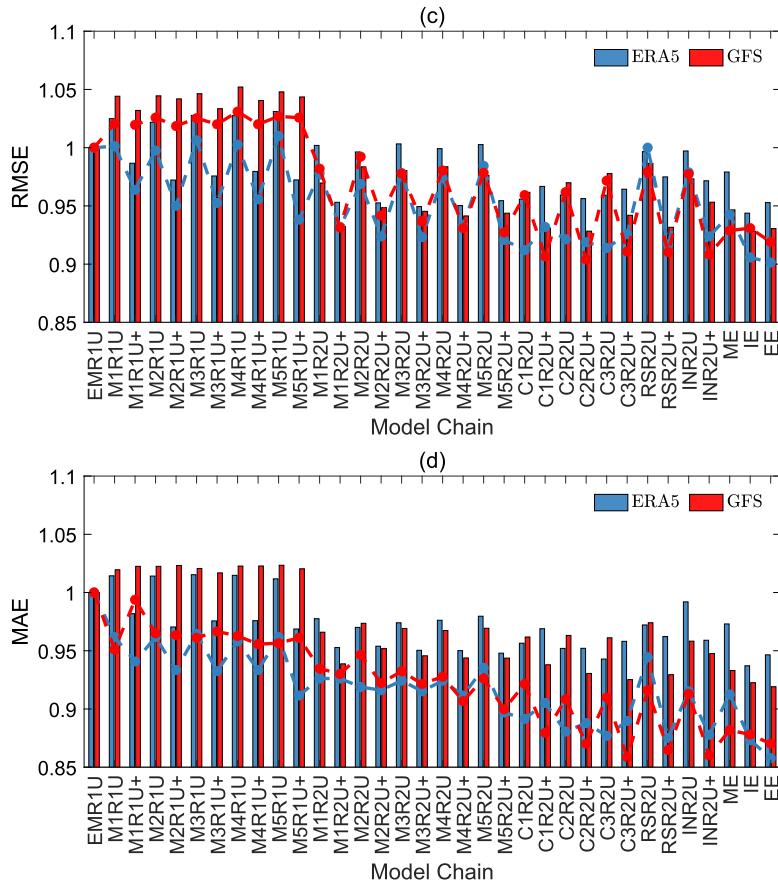
Figure 4.10 (cont.): (c) RMSE, Δt = 6hrs, and (d) MAE, Δt = 6hrs.

4
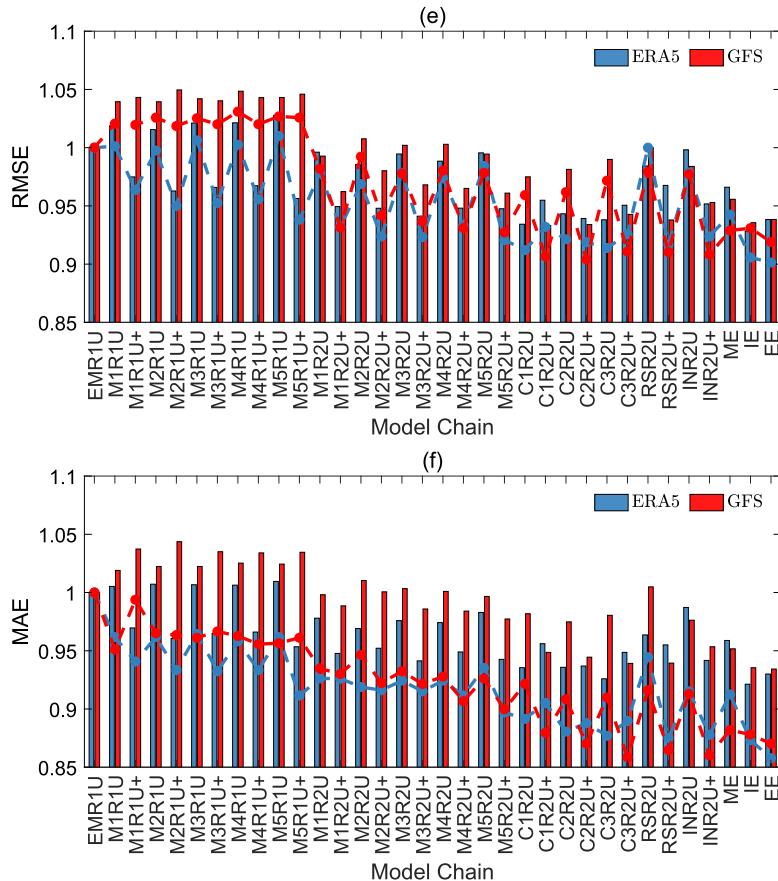
Figure 4.10 (cont.): (e) RMSE, Δt = 9hrs, and (f) MAE, Δt = 9hrs.

4.7. CONCLUSIONS

In this chapter, a simple empirical model and advanced deep learning models are compared in their ability to improve offshore wind power production and wind power ramps forecast for the Belgian offshore wind farm cluster based on global model data. The models use as input grid point data extending over different domain sizes from the ERA5 reanalysis, and the GFS global numerical weather prediction model.

The use of of a larger domain over the site of interest and additional variables other than wind speed are seen to increase the performance of the neural network models. In general, the more complex model architectures and model ensembles perform better and add value to the GFS forecasts when compared to ERA5 which can be considered closer to the 'ground' truth in terms of the meteorological values. However, the gains are small. MLP models with few layers perform well for both absolute power and ramp predictions. The differences in forecast model performance between the absolute power and power ramps reduces as the ramp period increases and for the longer ramp periods, the gains in performance seen with GFS as input using the larger grid reduces relative to ERA5.

This chapter has shown the potential for using deep neural networks to enhance numerical weather prediction forecasts of wind power and wind power ramps, though is an area for further investigation given the rapid advances in the development of ML algorithms.

4

5

WIND POWER AND RAMPS: ASSOCIATION WITH WEATHER PATTERNS

You can never cross the ocean until you have the courage to lose sight of the shore.

Christopher Columbus (1451 – 1506)

Large-scale weather patterns and their variability can influence both the amount of wind power production and its temporal variation, i.e., wind power ramps. In this study, we use a self-organising map to cluster hourly sea level pressure into a discrete number of weather patterns. The dependency of wind power production and wind power ramps on these weather patterns is studied for the Belgian offshore wind farm fleet. A newly developed wavelet-surrogate ramp-detection algorithm is used for the identification of wind power ramps. It was observed that low-pressure systems, southwesterly and northeasterly wind flows are often associated with high levels of wind power production. Regarding wind power ramps, the type of transition between weather patterns was shown to determine whether ramp-up or ramp down events would occur. Ramp-up events tend to occur due to the transition from a high-pressure to a low-pressure system, or the weakening of the intensity of a deep low-pressure system. The reverse is associated with ramp down events.

5.1. INTRODUCTION

IN Chapter 3, a wavelet-surrogate based power ramp detection algorithm is proposed which can detect ramp events of arbitrary ramp rate, timescale, independent of rated capacity. The wind power ramps variation is largely driven by the type of prevailing weather system. This chapter investigates the association of wind power and power ramps with weather patterns. To identify the types of weather patterns from sea level pressure data, a self-organizing map (SOM) is used.

Weather patterns influence the generation of wind power [148, 149]. For instance, European wind power production shows a significant regional variation as a result of the prevailing weather patterns [150]. The occurrence of cyclonic regimes corresponds to an increase of wind power production across Northern Europe. Blocked (high-pressure) regimes lead to an increase of wind power production over southeastern Europe. By contrast, wind power production in the Mediterranean does not show a clear correlation with either cyclonic or blocked regimes. We believe that understanding the relationship between weather patterns and wind power generation helps in power system planning, energy trading and dispatch.

The demand of electricity also shows an association with weather patterns. For example, over the UK, low electricity demand days and high wind power capacity generation are associated with Icelandic low-pressure systems. However, high-electricity-demand days and low wind power capacity are related to high-pressure systems over Scandinavia and Great Britain [151]. Additionally, during prolonged cold spells, the Irish wind power capacity factors are low while the demand for electricity is relatively high [152]. These examples suggest that there are further benefits in classifying and quantifying the prevalence of different weather systems when balancing supply and demand where there is a large penetration of wind power.

Furthermore, weather patterns influence the magnitude and direction of large and rapid changes in wind power production, known as wind power ramps. A study which looked at UK wind farms showed that the passage of cyclonic systems could cause wind power ramps over time scales of around four hours. However, the passage of frontal systems tends to produce short-duration power ramps of timescales in the range of 30 – 60min [153]. Over Eastern Japan, the frequency of ramp-up and ramp down events

shows a strong association with particular weather patterns [154]. It was observed that ramp-up events are mostly related to extra-tropical cyclones while ramp down events are primarily associated with reduced zonal (or meridional) gradients of the surface pressure.

The occurrence of power ramps phenomena described above tends to be associated with particular atmospheric circulations. Attempts have been made to group these circulations into a discrete number of weather patterns. The Lamb classification scheme is one of the earliest and most well-known approaches to classify large-scale European weather patterns focused over the British Isles [155]. The scheme initially consisted of only 10 weather patterns but was later extended to 26 [156]. A related classification scheme known as the GWL (Grosswetterlagen) scheme was developed using 29 weather patterns over Europe [157]. Recently, k-means clustering [158] and principal component analysis (PCA) [150] have been used to cluster European weather patterns into 30 and seven classes, respectively. The use of machine learning to classify weather patterns has increased in popularity in recent times. For example, a study showed the use of three different machine-learning techniques to identify extreme weather events in Taiwan [159] where they were shown to outperform more traditional objective weather classifiers.

An alternative neural network approach to classify weather patterns is to use a self-organizing map (SOM). A SOM has advantages over other well-known clustering techniques. First, SOMs capture nonlinear patterns within the data that cannot be clustered using linear recognition tools such as PCA or Empirical Orthogonal Function (EOF) analysis. Furthermore, SOMs preserve the topological order of the weather patterns [160, 161] leading to a smooth spatial transition from one weather pattern to the next. This is an advantage when grouping patterns into overarching circulation types, e.g., predominantly high or low pressure.

In this chapter, SOM is used to identify the prominent prevailing weather patterns over Europe using mean sea level pressure as an input to SOM. Then, the discrete number of weather patterns are associated with the offshore wind power production, for the aggregated Belgian wind farm fleets.

Section 5.2 describes the wind power and meteorological data used to obtain the results of this chapter. The SOM algorithm that is used to identify weather patterns and the ramp detection methods are presented in section 5.3. In section 5.4, we discuss and present the results: (I) the prominent SOM-based weather patterns, (II) wind power production and ramps characterstics by weather patterns, and (III) a few case studies of the temporal wind power and power ramps with the corresponding weather patterns is shown in section 5.6.3. Finally, the conclusion of this chapter is drawn in section 5.7.

5.2. Data

In this study, we use wind power data provided by Elia, the Belgian system operator[162] from the Belgian offshore wind farms located in the North Sea region at a longitude of between 2.7° and 3.0°E and a latitude of between 51.5° and 51.7°N. These sites were chosen because offshore wind power will make a significant contribution to future installed capacity, particularly in Northern Europe, and because the power production data are open access. The aggregated measured wind power is available from 2013 to date with a 15-min resolution. In 2013, the aggregated rated power was 195MW and by April 2020

had grown to 1608MW. However, during 2015 – 2016, there was no change in rated power which was 712MW. Thus, to simplify the analysis, in this study we consider only this two-year period. Furthermore, it was found that less than 1% of the data were missing for this period.

To cluster the weather patterns, we use sea level pressure (SLP) from the fifth generation of ECMWF's atmospheric reanalyses of the global climate (ERA5) [163] for the period 2003 – 2017. As the ERA5 data are of an hourly resolution, the 15-min wind power data are averaged within each hour so that they can be directly associated with the meteorological data. Therefore, all wind power and ramp values in the following analysis are based on *hourly* values.

5.3. METHODS

5.3.1. SOM ALGORITHM

The SOM was originally developed for pattern recognition [164–166] and is an unsupervised learning technique that maps high-dimensional input data onto a low-dimensional output space. In this chapter, we wish to map an arbitrary pressure field to one of a finite number of classes to assess wind speed (and thus wind power) dependency on large-scale circulation patterns.

A SOM is a simple neural network that consists of an input layer. In our case, the input layer consists of hourly sea level pressure (SLP) for the period 2003 – 2017. This provides $n = 131,496$ temporal data samples on a regular spatial grid of $m = 201 \times 141 = 28,341$ values (Figure 5.1a), representing the area that primarily influences European weather patterns, i.e. $30°W – 20°E; 35 – 70°N$ [167]. This input layer of n 1D data vectors (Figure 5.1b) is connected to a layer of i output neurons through a series of weight vectors (Figure 5.1c). The output layer is a 2D Kohonen map of 30 nodes where each node represents a series of representative weather patterns (Figure 5.1d) based on clustering of the input data.

For simplicity, we initialize the weight vectors from a random sample of the input SLP data vectors. Linear initialization would provide faster convergence but is computationally expensive [164]. The SOM is trained over a series of iteration steps in this study using SOM_PAK software that uses a sequential SOM training algorithm [168]. At each step t, a Euclidean distance is used to calculate the distance between each 2D input data vector $\mathbf{X}(t)$ and each of the i weight vectors $\mathbf{W}_i(t)$. The output node whose weight vector, $\mathbf{W}_c(t)$, is closest to each input node is called the Best-Matching Unit (BMU) and has an index c given by:

$$c = \underset{i}{\operatorname{argmin}}(||\mathbf{X}(t) - \mathbf{W}_i(t)||) \tag{5.1}$$

Then, the weighting vectors of the BMU and those close by are updated to better reflect the input vector:

$$\mathbf{W}_i(t+1) = \mathbf{W}_i(t) + \alpha(t)h_{ci}(t)[\mathbf{X}(t) - \mathbf{W}_i(t)] \tag{5.2}$$

where $\alpha(t)$ is a learning rate which decreases monotonically as a function of iteration
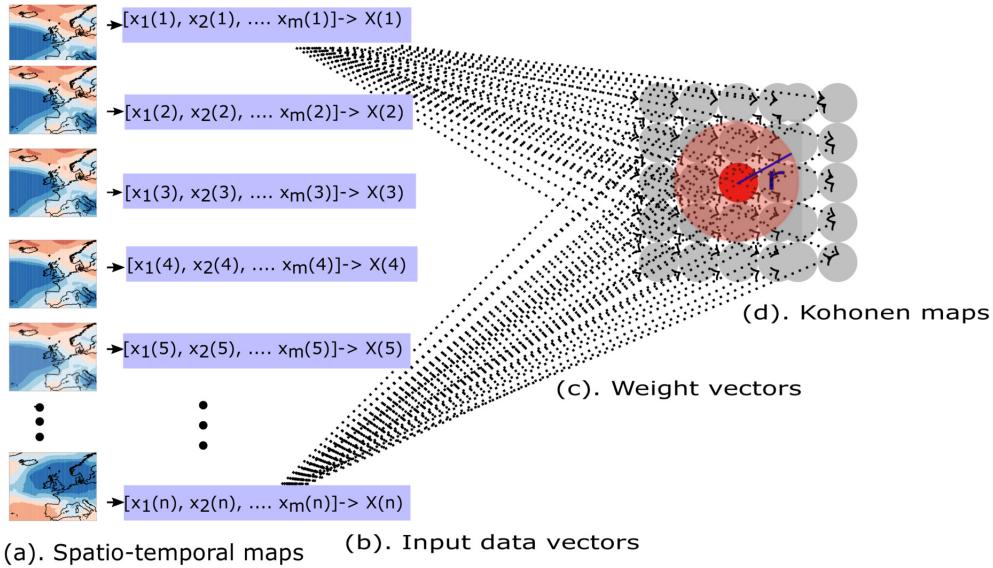
Figure 5.1: Schematic diagram of SOM: (a) n samples of hourly spatial SLP 2D maps containing m grid points (b) 2D spatial data converted into 1D vectors, (c) weight vectors ($\mathbf{W}_i$) connecting input data with 2D Kohonen maps, (d) SOM topological maps and the neighborhood radius (σ). The red dot is a hypothetical Best-Matching Unit (BMU) which has the smallest Euclidean distance between the weight of the output neuron and the input data vector.

time, and h_{ci} is the Gaussian neighborhood function. The value of $\alpha(t)$ decreases linearly with iteration time:

$$\alpha(t) = \alpha_0 \left(1 - \frac{t}{t_{max}}\right) \tag{5.3}$$

where α_0 is the initial user defined learning rate, and t_{max} is the maximum iteration time.

The Gaussian neighborhood function is given by:

$$h_{ci}(t) = \exp\left(-\frac{\text{sqdist}(c,i)}{2\sigma^2(t)}\right) \tag{5.4}$$

where the neighborhood radius size ($\sigma(t)$) also reduces linearly as a function of iteration t in a similar manner to $\alpha(t)$, and sqdist(c,i) is the squared geometric distance between the BMU and neuron i.

As the neurons are initialized randomly, two phases of training are required for the neurons to maintain a topological order. In the first, rough training phase, a relatively wide radius of influence ($\sigma_0 = 6$) is used, i.e., approximately the diameter of the Kohonen map (Figure 5.1d) and the initial learning rate, α_0, is set to 0.05. In the second, fine-tuning phase, the training is iterated using a smaller radius ($\sigma_0 = 3$) and an initial learning rate of 0.02. Following [168], in the first phase σ_0 is about the size of the diameter of the map; and it is reduced to one third of it in the second phase.

In both training phases, the training passes through several iteration steps. In the rough training phase, the total number of iterations, t_{max}, steps is 10% of n (the number of input data vectors). In the fine-tuning phase, we use a Sammon mapping projection [169] at different iteration steps to check the topological order of the neurons to see if the SOM is sufficiently trained. If the Sammon projection shows a relatively 'twisted' neuron map (see Figure 5.2a) then the SOM is not fully trained, whereas a more organized arrangement (Figure 5.2b) suggests that the SOM has been trained sufficiently.
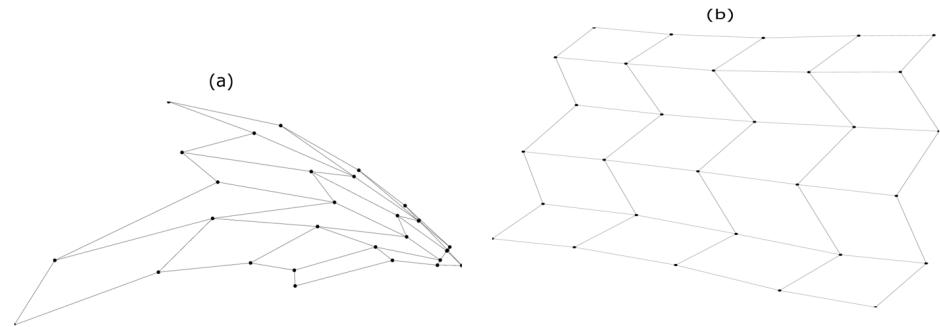

Figure 5.2: Sammon map projection of ERA5 hourly SLP during fine –tuning: (a) after 10,000 iteration steps, and (b) after 131,496 iteration steps.

5.3.2. DETECTING WIND POWER RAMPS

The newly proposed wind power ramps detection algorithm, the wavelet-surrogate algorithm, that is presented in chapter 3 is used in this chapter. This method first generates a wavelet transform of an original time series. Additional wavelet transform is performed based on several random shuffles (100 times in this study) of the original power time series. The wavelet coefficients of this latter transform are used to discriminate the coefficients generated using the original time series from uncorrelated noise. Daubechies level-1 (Haar) mother wavelet to generate the wavelet coefficients using 15-min aggregated wind power values up to a given maximum wavelet scale (a_{max}) and a discrimination level (W_T^*) is used in chapter 3. Based on the hourly offshore wind power data, Figure 6.1 shows the application of the wavelet-surrogate (WS) algorithm to detect ramps using a value of $a_{max} = 20$ and four threshold values for W_T^*. As the discrimination level of W_T^* is reduced from 10% to 1%, the number and duration of detected ramps are reduced, i.e., a high percentage value of W_T^* will pick up a larger number of potentially weak ramps, whereas a smaller percentage value only picks up the strong ramps in a given time period. To provide a reasonable balance between these, we use a 5% discrimination level for W_T^* for the subsequent analysis. Please refer to chapter 3 for further details.
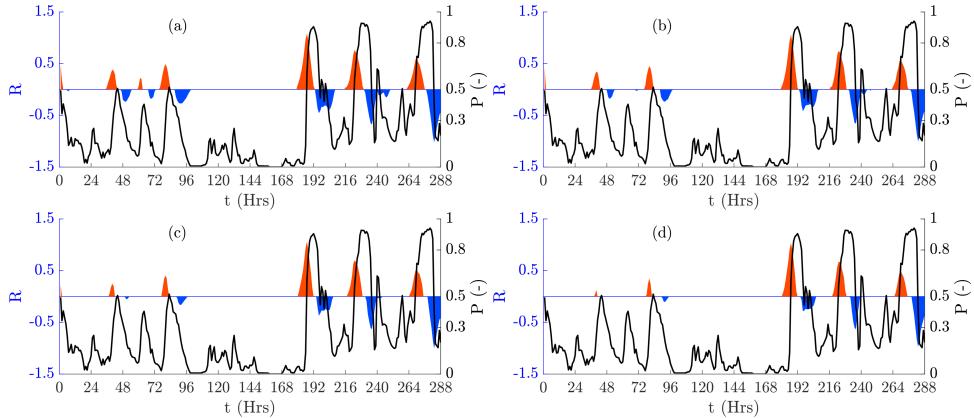
Figure 5.3: Detected normalized power ramps for the period of 20 to 31 May 2015 for $a_{max} = 20$ with discrimination levels, W_T^* of: (a) 10% (b) 5% (c) 2% and (d) 1%. Ramp-up events are shown in red and ramp-down events in blue.

5.4. RESULTS

In this section, the main characteristics of the SOM-clustered weather patterns are first discussed. Then the dependence of the mean power production and power ramps on the different weather patterns are analyzed. Finally, some individual ramp case studies are analyzed in more detail. It should be noted that in all cases, results are normalized to the total rated capacity of the Belgian offshore wind farms during the period 2015 – 2016, i.e., 712MW.

5.5. WEATHER PATTERNS

Based on the discussion in Section 5.1 concerning previous attempts to classify European weather patterns, we chose to classify the hourly ERA5 SLP for the period 2003 – 2017 into 30 weather patterns. The result is shown in Figure 5.4. Hereafter, we refer to these 30 patterns as SOM-based weather patterns. The figure highlights the advantage of using a SOM for classification, as the weather patterns show a smooth transition from one weather pattern to the next. This allows the patterns to be grouped by climatology. For example, weather patterns at the center of the map ($c2 – e2$ and $c3 – e3$) show predominantly weak (slack) pressure gradients, especially over the North Sea, and are characteristic of the summer season [170]. The weather patterns at the right of the map ($f1 – f4$) are dominated by blocked regimes/high pressure, which dominate the winter season [171].

When comparing the SOM-based weather patterns with those clustered using a PCA [150], we found that the SOM produces similar results to the clustered weather patterns in [24, 167]. It can be seen that the classification has captured the main European weather patterns including: Atlantic trough ($f4$, $f5$), Scandinavian trough ($a3$, $a4$), Atlantic ridge ($a1$, $a2$), Scandinavian blocking ($f1$), Greenland blocking ($e1$), Northerly flow ($b1$, $c1$) and British Isles Low Pressure ($a5$) which also prevail in the GWL weather pattern classification. The weather patterns at the bottom of the map are mainly dom-
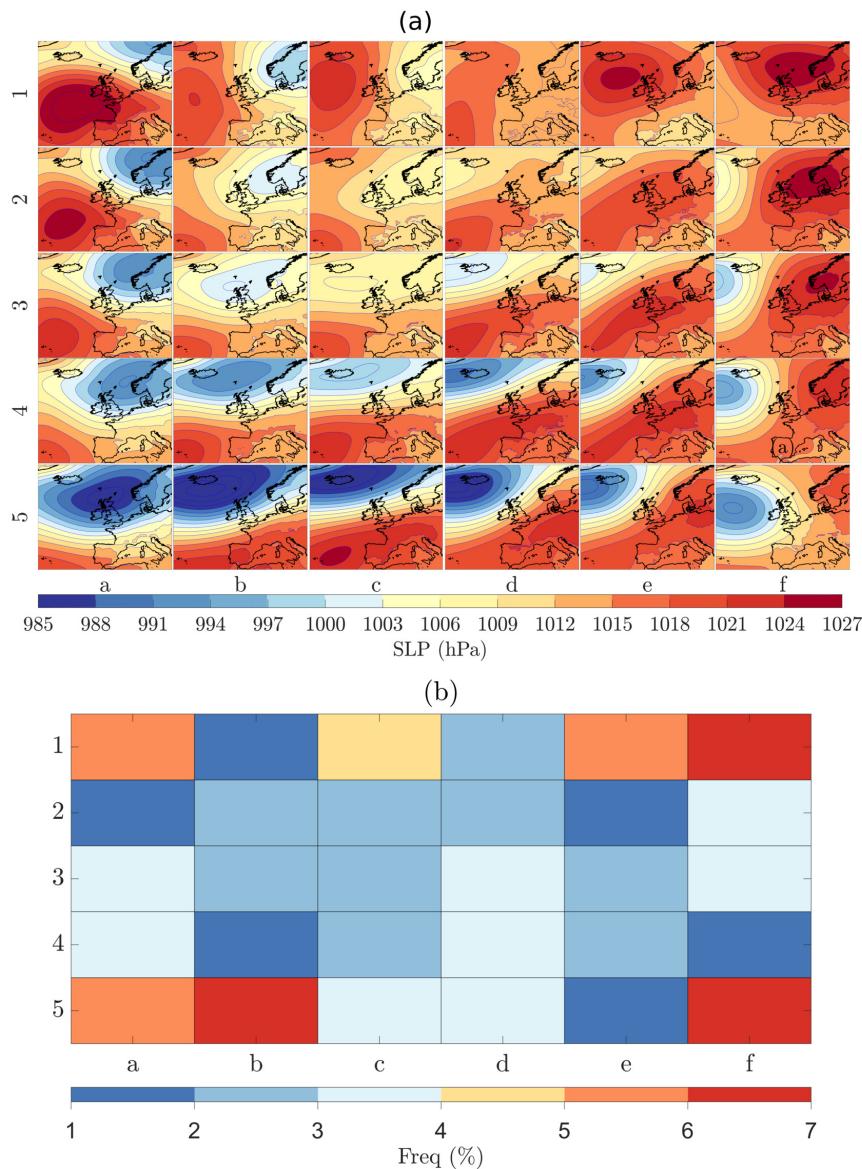
Figure 5.4: The SOM-based weather patterns using ERA5 hourly sea level pressure 2003 – 2017 and corresponding frequency of occurrence: (a) The SOM-based weather patterns. The color scale is hourly sea level pressure (SLP) in hPa and the contour lines are at intervals of 3 hPa; and (b) frequency of weather patterns in (%). Rows (1 – 5) and columns (a – f) are used to label the weather patterns.

inated by zonal flow ($b5 - e5$). Moreover, we can see that the weather patterns which display strong pressure gradients are located at the edges of the map, i.e., right ($f1 - f4$): high pressure over Europe and Scandinavia, left ($a1 - a4$): high pressure over the Atlantic and low pressure over Scandinavia, top ($b1 - d3$): meridional flow and bottom ($a5 - f5$): low pressure and zonal flow. Those weather patterns in the center of the map show indistinct pressure systems with weak gradients. In Figure 5.4b, the frequency of the different weather patterns is shown. Notably, those weather patterns with distinct features at the edge of the map tend to occur more frequently. This likely reflects the fact that most pressure fields can be mapped to distinct weather patterns.

The SOM-based weather patterns are also compared with the Royal Netherlands Meteorological Institute (KNMI) synoptic charts to see how well synoptic systems at a particular point in time are captured using the six most frequently occurring patterns, i.e., $a1$, $e1$, $f1$, $a5$, $b5$ and $f5$. The synoptic chart at 00:00UTC associated with the first occurrence in the time series of each of these six weather patterns is used for validation. The resulting charts are shown in Figure 5.5.

Even though the SOM-based weather patterns are based on the long-term period 2003 – 2017, in general, they capture quite well the individual synoptic systems on given days, with some slight differences. For example, on 3 January 2015, the low-pressure system centered over Finland and the extended high-pressure area west of the UK and south over continental Europe observed on the synoptic chart are essentially captured by weather pattern $a1$, though the small low to the west of the UK is not seen in the SOM-based weather pattern. The synoptic chart also shows a warm front to the southwest of the UK. The European ($e1$) and Scandinavian ($f1$) blocked regimes are clearly observed in the synoptic charts on 6 February 2015 (Figure 5.5b) and 17 March 2015 (Figure 5.5c), respectively. The synoptic chart on the 6 February 2015 also shows a warm front moving over the North Sea. Weather pattern $a5$, dominated by a low-pressure system over the UK is clearly visible in the synoptic chart of 15 January 2015 (Figure 5.5d) with cold and warm frontal systems moving across the North Sea area. Figure 5.5e shows a zonal flow synoptic chart dominated by a southwesterly wind flow which is captured by weather pattern $b5$. This chart also shows a warm front over the North Sea region. Lastly, on 13 February 2015, the synoptic chart shows a low-pressure system over the Atlantic (Figure 5.5f) which is well captured by weather pattern $f5$. On this chart, frontal systems can be seen in the Atlantic with an occluded front approaching the English Channel.

In summary, the SOM-based clustering captures well the features of instantaneous weather systems and in many cases, frontal systems are likely to be observed which may lead to rapid changes in wind speed (wind power ramps).

5.6. WIND POWER TRENDS BY WEATHER PATTERN

5.6.1. WIND POWER PRODUCTION

In Figure 5.6a, the frequency of normalized measured wind power production is allocated to the weather patterns. The highest values of power production that occur frequently are associated with those weather patterns located at the bottom left of the map shown in Figure 5.4 which are mainly characterized by zonal flow and cyclonic circulation (low-pressure systems), i.e., $a5$, $a4$, $a3$, $b5$ and $b4$. However, frequent low-power

5
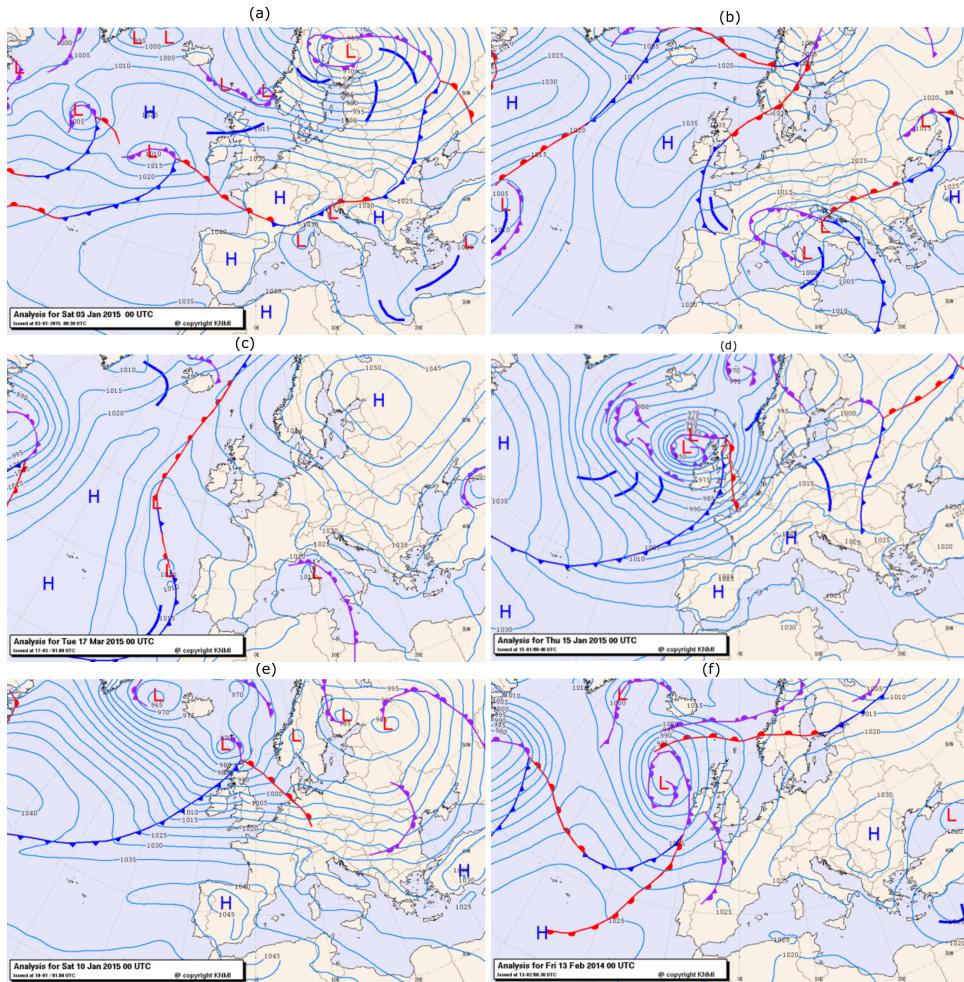
Figure 5.5: KNMI synoptic charts (https://www.knmi.nl, accessed on 05 May 2021) corresponding to the six most common SOM-based weather patterns at 00:00 UTC on: (a) 3 January 2015 (a1), (b) 6 February 2015 (e1), (c) 17 March 2015 (f1), (d) 15 January 2015 (a5), (e) 10 January 2015 (b5), and (f) 13 February 2015 (f5). The prominent synoptic features are shown: L (low pressure), H (high pressure), blue (cold front), red (warm front) and magenta (occluded front).

production value is particularly associated with weather patterns where high pressure dominates, notably blocked regimes such as $f2$ and $f3$ and regimes in the center of the map with slack pressure gradients.

In Figure 5.6b, the normalized mean wind power production by weather pattern is shown. This value can be considered to be the mean capacity factor of the combined off-shore Belgian wind farm cluster. The overall mean capacity factor across all weather patterns is about 0.4. The values effectively summarize the distributions in Figure 5.6a but highlight the extreme differences in capacity factor across the different patterns ranging from 0.2 to 0.8. Maximum capacity is observed for the weather patterns mainly located at left-bottom which are characterized by cyclonic circulation systems. However, the weather patterns in the right are associated with low-capacity factor, and those weather patterns are mainly characterized by blocked regimes or high-pressure systems with a slack pressure gradient.

5.6.2. WIND POWER RAMPS

Figure 5.7 shows the frequency of wind power ramps by weather pattern which are detected using the wavelet-surrogate method with a 5% discrimination level for W_T^* and $a_{max} = 20$. These parameters can detect both short and long duration power ramps. The percentage of ramps is calculated based on the total number of power production values in each weather class (Figure 5.7a (ramp-up) and Figure 5.7b (ramp down)); and as a fraction of the total number of ramps over the two-year period (Figure 5.7c (ramp-up) and Figure 5.7d (ramp down)).

In Figure 5.7a, it is seen that when weather patterns $c2$, $b3$, $c3$ and $c5$ are prevalent, the largest percentage of ramp-up events occur. The first three of these patterns are associated with transitions from high to low-pressure systems when pressure gradients are relatively weak, but wind speeds are still sufficient to maintain a modest amount of production. In such cases, wind turbines are operating below rated power in a steep part of the power curve and thus relatively small changes in wind speed can cause a large change in wind power. The high number of events in $c5$ is less clear as there is a pattern of distinct westerly flow, though with modest winds when looking at the capacity factor values in Figure 5.6b. Again, this is likely to be associated with greater swings in production if operating frequently below rated power.

On the other hand, the largest percentage of ramp down events is seen when patterns $a1$, $a2$, $b1$, $b2$ (in the top left of the SOM) and $b4$ and $c4$ (in the bottom left) prevail (see Figure 5.7b). There does not appear to be a clear link to the pattern of these circulations that could lead to a higher number of ramp down events, but again, the capacity factors are modest during these periods, so wind power output is likely to be variable for a similar reason as above.

When viewed as the percentage of the total number of ramps, the picture is slightly different. In this case, the most frequent number of ramp-up events occurs during patterns $c5$, $d5$ and $f5$ (see Figure 5.7c). This is partly influenced by the frequency with which the synoptic situations fall within one of these patterns, but this is not the entire reason. Patterns $c5$ and $d5$ are not the most frequent patterns but show a proportionally higher number of ramp-up events. The patterns $c5$, $d5$ and $f5$ are all associated with modest winds and again it is likely that the wind turbines will be operating in the below
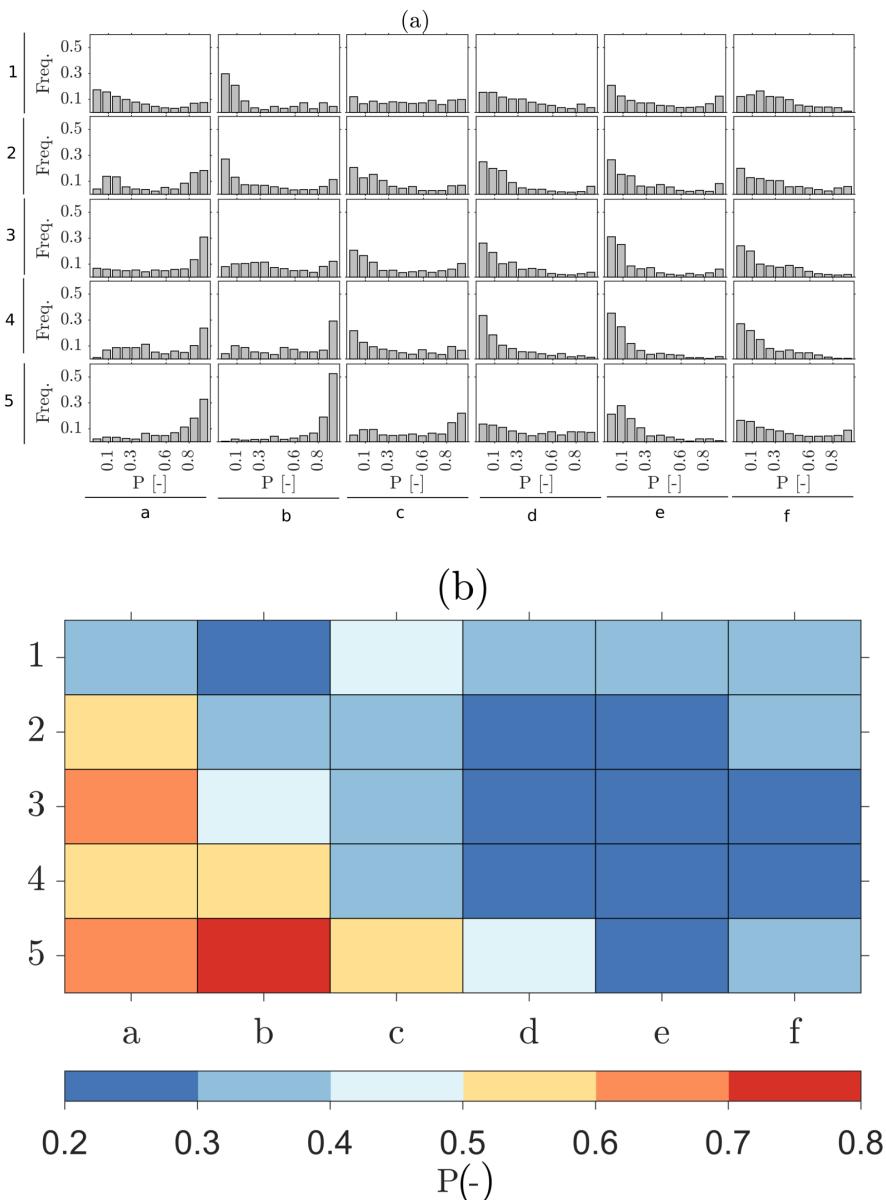
Figure 5.6: Normalized wind power production by weather patterns: (a) distribution of normalized wind power, and (b) mean value of normalized wind power (mean capacity factor).
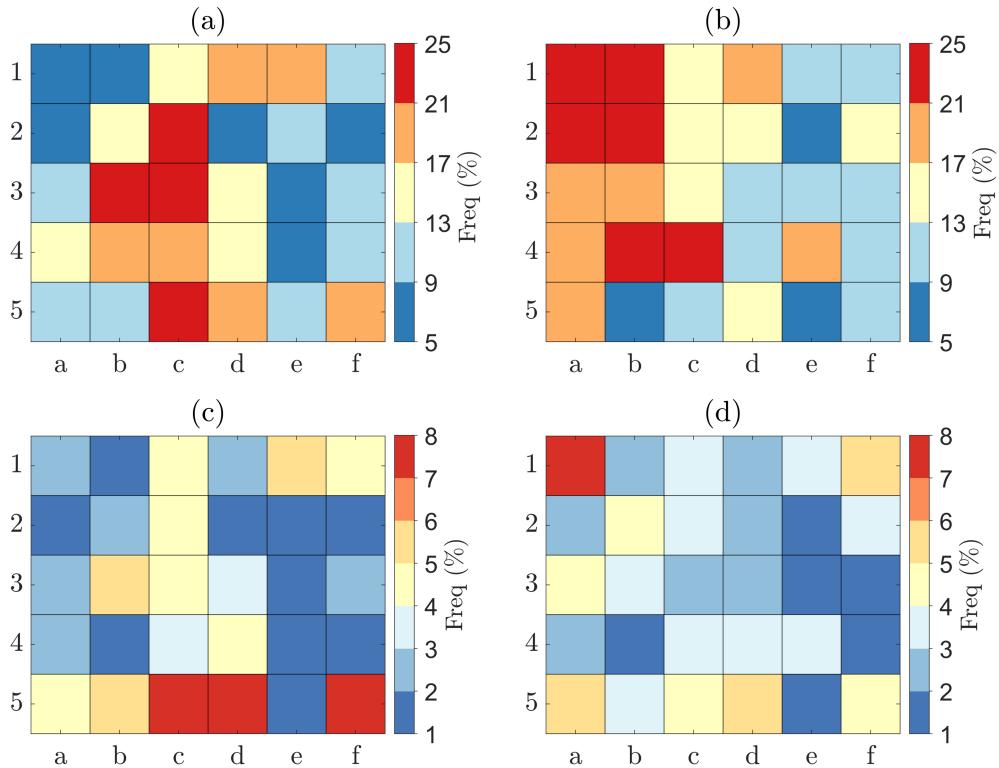
Figure 5.7: Frequency of ramp-up and ramp-down events as a function of weather pattern: (a) ramp-up events as a fraction of the number of hours of generation classified as a particular pattern, (b) as (a) for ramp down events, (c) ramp-up events as a fraction of the total number of ramps identified, and (d) as (c) for ramp down events.

rated range. The ramp down events as a fraction of the total ramps show less variability (see Figure 5.7d), with the highest occurrence for pattern $a1$ which was also seen in Figure 5.7a.

In summary, the occurrence of wind power ramps seems to be associated with modest wind speeds when wind turbines are operating at below rated power in the steepest part of the power curve. Another factor which could affect the prevalence of ramp events is the passage of fronts [17] which is not picked up from the pressure fields alone although the individual charts in Figure 5.5 shows that such activity is frequently present for several of the most commonly occurring patterns. Alternatively, the transition between particular patterns may play a role and this is explored in the next section.

5.6.3. WIND POWER RAMP CASE STUDIES

In this section, we look for temporal trends in weather-pattern transitions during ramp events, classifying the ramps into weak and strong wind power ramp cases as shown in Figures 5.8 and 5.9, respectively. In Table 5.1, the first four ramp cases, RC1 – RC4 are relatively slowly evolving ramps (weak ramp rates), whereas the ramp cases, RC5 – RC8 are stronger ramps that show a rapid increase or decrease over a relatively short period of time.

The temporal evolution of the weak ramp cases, RC1 – RC4, along with the associated weather-pattern transitions just before, during and just after each ramp event are shown in Figure 5.8. The ramps are characterized by a significant rise or fall in power production over a long period. Figure 5.8a and 5.8c show ramp-up events in green whereas Figure 5.8b and 5.8d show ramp down events in red. Figure 5.9 shows the equivalent results for the strong ramp cases RC4 – RC8 where significant power changes are seen over a short period.

Table 5.1: Case study ramp start and end times (to the nearest hour) and type of ramp.

Ramp cases	Start	End	Ramp type
RC1	26-Nov-2015 20:00	27-Nov-2015 15:00	ramp up
RC2	22-Nov-2016 10:00	23-Nov-2016 01:00	ramp down
RC3	23-Jan-2015 12:00	24-Jan-2015 02:00	ramp up
RC4	09-Mar-2016 11:00	10-Mar-2016 01:00	ramp down
RC5	19-May-2016 13:00	19-May-2016 23:00	ramp up
RC6	04-Feb-2016 11:00	04-Feb-2016 20:00	ramp down
RC7	27-May-2015 14:00	27-May-2015 22:00	ramp up
RC8	09-May-2015 14:00	10-May-2015 02:00	ramp down

By combining the temporal evolution of each ramp with the change in weather patterns observed it is possible to gain some insight into the cause of the ramp events. For example, for RC1 (solid green line) and RC3 (dashed green line), we can see that the start of the ramp-up events are associated with a transition from weak low-pressure systems to strong low-pressure systems, i.e., $b4$ to $b5$ for RC1 and $d4$ to $c5$ for RC3. These weather patterns are located near the bottom of the SOM in Figure 5.4a. In these cases, the ramps are likely due to the fact that the wind turbine capacity factors increase as
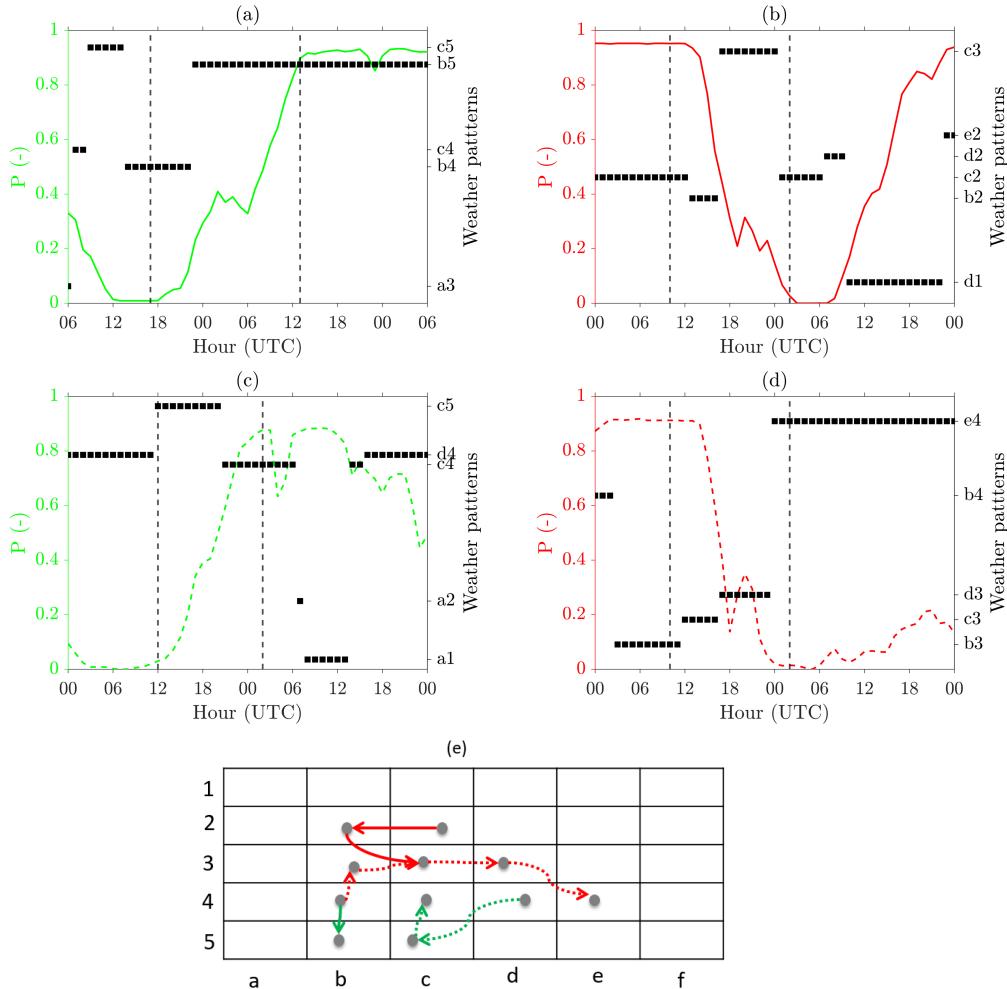
Figure 5.8: Weak wind power ramp cases and associated weather patterns: (a) RC1, (b) RC2, (c) RC3, (d) RC4, and (e) a sketch of the weather-pattern transitions for RC1 (solid green line), RC2 (solid red line), RC3 (green dashed line) and RC4 (red dashed line). RC1 – RC4 periods are shown in Table 5.1. The vertical black dash lines in the (a – d) indicate the detected start and end time of the ramps.

the low-pressure systems become deeper. The ramp down cases, RC2 (solid red line) and RC4 (dashed red line) are triggered when the low-pressure systems evolve to high-pressure systems. These weather patterns transition from the center left of the SOM to the right in these ramp cases. As a result of these weather-pattern transitions, the normalized wind power production decreases to almost to zero from near maximum capacity factors. For the strong ramp cases in Figure 5.9, the first ramp-up event, RC5 (solid green line), occurs due to a transition from a weak low-pressure system (c3) to a strong low-pressure system accompanied by a southwesterly wind flow (d4). However, the second ramp up event, RC7 (green dashed line), is triggered due to a transition from a weather pattern (a1) with a high-pressure system in the area of the wind farms transitioning to weak zonal/low pressure (c3). In this case, the normalized wind power production is close to zero during weather pattern a1 as the high-pressure system leads to very low wind speeds around turbine cut-in. The ramp down case, RC6 (solid red line), occurs due to a transition from weather pattern a1 to the weather pattern d4 characterized by southwesterly wind flow. In this case, occluded and warm frontal systems contributed to the development of the ramp as seen in the KNMI synoptic chart (not shown). For the second ramp down event, RC8 (red dashed line), a transition is seen from a weak pressure system (d2) to strong blocked regimes (e3 and f3).

It is worth noting that for the strong ramp events, the transitions seen in the SOM between weather patterns are larger compared to the weak ramps. This reflects the more rapid changes in wind speed associated with rapid changes in weather conditions and the fact that the data are hourly so that intermediate patterns are less likely to be resolved.

In summary, it can be seen that ramp events tend to be associated with a change in weather pattern. By studying the transition through different weather patterns, the type and strength of a ramp can be determined. The combination of weather-pattern transitions with information about frontal activity could enhance this still further. This would require a more detailed clustering approach using temperature information, which is beyond the scope of this study.
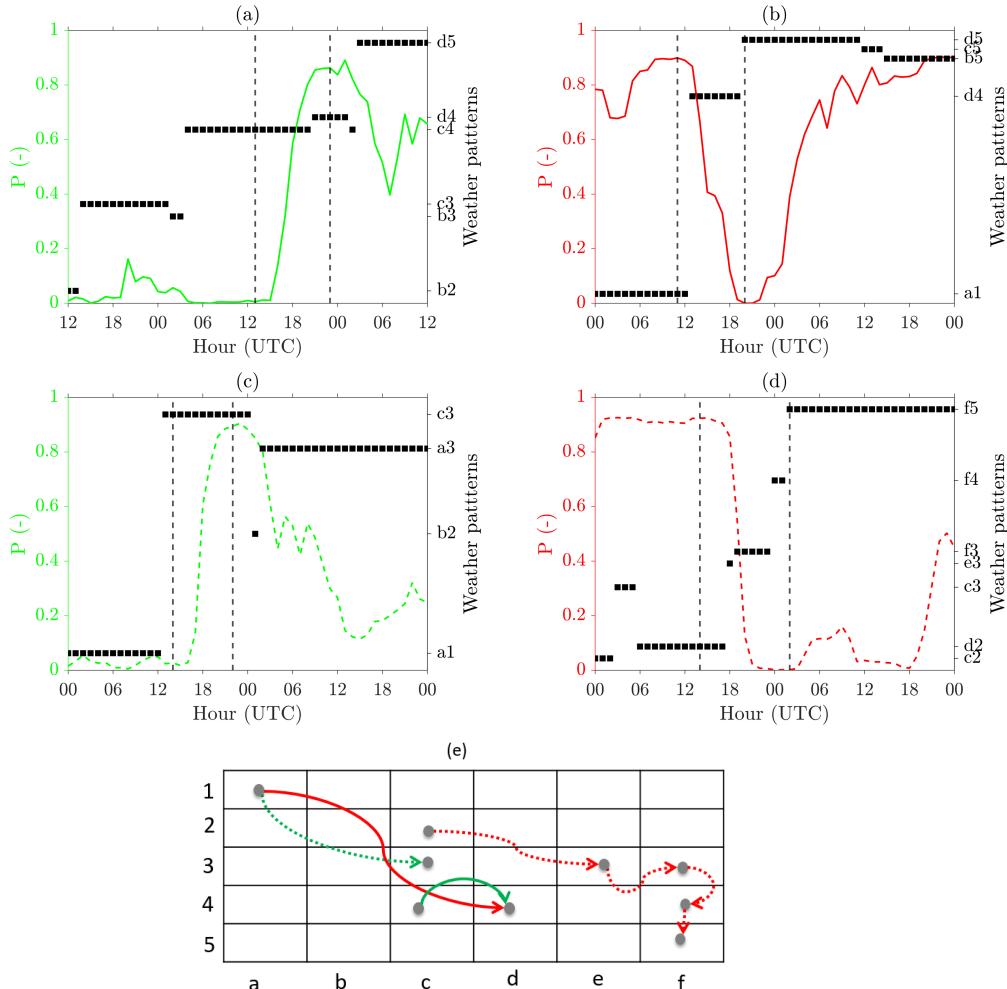
Figure 5.9: Strong wind power ramp cases and associated weather patterns: (a) RC5, (b) RC6, (c) RC7, (d) RC8, and (e) a sketch of the weather-pattern transitions for RC5 (solid green line), RC6 (solid red line), RC7 (green dashed line) and RC8 (red dashed line). RC5 – RC8 periods are shown in Table 5.1. The vertical black dash lines in the (a – d) indicate the detected start and end time of the ramps.

5.7. CONCLUSIONS

In this chapter, we demonstrate the application of a SOM to classify weather patterns over the North Sea. The advantage of the SOM is shown in its ability to classify similar weather circulation patterns close together in the map, allowing a higher-level overview of the prevailing weather systems.

The relationship between the clustered weather patterns and normalized wind power production for the Belgian offshore wind farm fleet has been quantified. Wind power production shows a maximum capacity factor for those weather patterns that are characterized by cyclonic (low-pressure) systems, northeasterly and zonal wind flow, whereas a weak pressure gradient and blocked regimes are the main cause for low-capacity factors.

Finally, we have studied the dependency of wind power ramps on prevailing weather patterns. In general, wind power ramps occur frequently for the weather patterns that are characterized by low-pressure systems, northeasterly and zonal wind flow. The type of weather-pattern transition determines the type of ramp. Eight ramp cases were studied to better understand the weather-pattern transitions which occurred during these events. It was seen that the ramp events were commonly associated with a change in weather pattern. For the four cases examined, ramp up events occurred during the transition from weak low-pressure systems to deep low-pressure systems. The four ramp down events were seen to be associated with a transition from low-pressure systems to blocked regimes.

For further work, it is recommended that additional information about the prevalence of frontal systems be included, for example, using a SOM to cluster spatial patterns in temperature. In addition, a more comprehensive analysis is required of the weather-pattern transitions that are seen for many ramp events to provide a deeper insight into the dependency of wind power ramps for different weather circulation patterns.

6

PROJECTED CHANGES IN WIND POWER AND RAMPS

Anyone who has never made a mistake has never tried anything new.

Albert Einstein (March 14, 1879 – April 18, 1955)

.

Only a few studies on the overall impact of climate change on offshore wind power production and wind power ramps in the North Sea region have been published. This study focuses on the characteristics of expected wind power production and wind power ramps in the future climate aided by the classification of circulations patterns using a self-organizing map (SOM). A SOM is used to cluster high-resolution CMIP5-CORDEX sea level pressure data into 30 European area weather patterns. These patterns are used to better understand wind power production trends and any potential changes. An increased frequency of occurrence and extended persistence of high pressure systems lasting at least 24 hours is projected in the future. Whereas contrasting reducing tendency for low-pressure systems is estimated. No significant evidence is seen for a change in wind power capacity factor over the North Sea, though tentative evidence is seen for a reduction in wind power ramps. Annual energy production is seen to be dominated by a small number of weather patterns with westerly, south-westerly or north-westerly winds. Future wind power production is projected to become less from westerly winds and more from south-westerly and north-westerly flows. Ramp up events are primarily associated with strong south-westerly winds or weather patterns with a weak pressure gradient. Ramp down events have a stronger association with more north-westerly flow. In a future climate, a reduction in ramp up events associated with weak pressure gradients is projected.

6.1. INTRODUCTION

IN Chapter 3 and 5, wind power ramp detection algorithm and the association of weather patterns with wind power and power ramps are discussed, respectively. This chapter looks into future changes in the frequency of weather patterns, and how this may affect wind power production and wind power ramps. Weather patterns are clustered using a self-organising map (SOM) and changes in future weather pattern frequency are quantified. Changes in future wind power generation and power ramps are quantified and these changes are associated with changes in projected weather pattern frequency.

Renewable energy generation will play a significant role in the aspiration to limit global temperature change to 1.5°C above pre-industrial levels [172]. The world needs a clear strategic plan to rapidly shift from fossil fuels to cleaner, renewable energy sources. Offshore wind energy, in particular, has seen rapid growth in European waters. Cumulative offshore wind power capacity was 2.5GW in 2009 but had reached 29.4GW by August 2022 [173, 174]. Overall, a significant proportion of offshore wind power is obtained from the North Sea, accounting for 77% (16.9GW) of the total European offshore wind power production [173]. As offshore wind will contribute an increasing fraction of future energy needs, there is now interest in how climate change may affect the level and characteristics of wind power production and wind power ramps, as this may have implications for future development and electricity grid balancing.

Studies have shown that projected changes in future wind speed patterns are highly uncertain, and there are significant disagreements between different climate models [175–179]. For example, the change in the 50-year return period of near-surface wind speeds down-scaled from the Bergen Climate Model (BCM) by the Rossby Centre Regional Climate Model (RCA, ver.3 or RCA3) shows a significantly larger change than when down-scaled using the High-Resolution Limited Area Model (HIRHAM5) over the east-

ern and central Mediterranean [175]. This disagreement appears to be due to the poor choice of roughness length in the planetary boundary layer scheme in RCA3 [180].

Moreover, in [175], it is also shown that climate model uncertainty propagates from general circulation models (GCMs) to regional climate models (RCMs), which leads to spatial variation in the down-scaled projected wind speed change. Significant spatial differences are observed in the projected changes to the 50-year return period of wind speed values when using the ECHAM5 GCM compared with the Bergen Climate Model (BCM) when downscaled by the same RCM (HIRHAM5). The downscaled ECHAM5 predicts larger changes over the North Atlantic Ocean than the downscaled BCM. In contrast, the down-scaled BCM predicts greater changes over the Black Sea.

As well as future climate-driven changes to wind speed, a number of studies (e.g. [84, 88, 92, 181–183] have considered how this might translate to changes in wind power in Europe. One such study has suggested that wind power production will increase over much of northern-eastern Europe, with the largest increases seen in the Baltic Sea. However, a decrease is seen for Atlantic areas, and much of western and southern Europe [84] and over the central Mediterranean Sea [181]. Here too, there is significant disagreement between different models regarding the sign of wind power changes. The work by [84] has shown that European wind power production is expected to show a change of about ± 15% and ± 20% by the mid and late 21st century, respectively [84]. A further study found that the production of wind power derived from the down-scaling of several GCMs using RCA (ver.4) for the Representative Concentration Pathway (RCP 4.5) and RCP 8.5 scenarios [184] shows a generally decreasing trend over the continent of Europe, with the exception of a slight increase over the Baltic Sea region [88].

Aside from spatial variation, projected changes in wind speed also show seasonal dependence. Some studies have indicated an increasing trend in wind power production during Winter, particularly over central and north-western Europe, while wind power production during the summer may decrease [177, 183, 185]. A model ensemble of down-scaled ECHAM5 output also shows similar seasonal behavior at the end of the 21st century over northern Europe [182, 186]. In the European winter, wind power production is at full capacity for a significant amount of the time. By contrast, during the summer, the output is more often at partial load or around cut-in. Higher winds in Winter may have little impact on output or indeed require more curtailment in times of high production and low demand. In contrast, during the summer, lower winds may require more backup capacity from other sources or increased energy storage [183].

Changes in the future temporal variation in wind power, such as wind power ramps, associated with rapid changes in wind speed, could impact supply and integration into the grid. Few studies have been carried out to quantify potential changes in future wind power ramps. A study conducted in Japan projected a significant reduction in ramp down events under a high warming scenario, with the largest reduction in all ramp events during the autumn [187]. However, to date, there has been no similar study for Europe or the projected European offshore wind power fleet. This is the motivation for this present study which looks at the change in the projected future frequency of wind power ramps over the North Sea region.

The characteristics of wind speed and wind speed ramps (along with the associated changes in wind farm output, including wind power ramps) can be associated with par-

ticular weather patterns. Therefore, future changes in large-scale synoptic circulation systems are of concern when wishing to understand potential changes in the characteristics of wind farm production. Such changes can manifest as a change in the frequency of particular weather patterns, a change in the mean spatial value of certain variables, or a shift in the position of a particular feature associated with a weather pattern, such as a high or low-pressure center.

Studies have indicated potential changes in the seasonal mean of mean sea level pressure (MSLP) under a future climate [176, 188, 189]. For instance, in winter (DJF), the projected MSLP over the Mediterranean region shows an increasing trend, while any change is expected to be small in summer (JJA) [176]. It was shown that the seasonal change in MSLP could contribute to a decrease in wind speed during winter over this region but that the signal was unclear in summer. Therefore, exploring the projected changes in weather patterns could help to understand the factors contributing to wind speed, wind power, and power ramps under the influence of future climate change.

A self-organizing map (SOM) has been used widely for identifying weather patterns in the field of meteorology [190] showing itself to be a powerful tool for reducing data dimensions. SOMs have the advantage that similar patterns remain close to each other in the output map. Previously, SOMs have been used to identify prevailing weather patterns over Europe [23, 191], and it was shown that SOM-based weather patterns captured the dominant circulation systems which could then be used to study spatial and temporal wind speed trends. Based on these findings, the approach taken in this work is to use a SOM to identify 30 distinct weather patterns using historical and projected sea level pressure data. The map is then used to study changes in the prevalence of each pattern and the impact this may have on future projected mean wind speed, wind power and ramp event frequency.

Specifically, the objectives of this study are: (i) to identify European weather patterns using three-hourly MSLP data from multiple climate model chains for 1970 – 2077, (ii) to quantify changes in the prevalence of these patterns in the 2006 – 2041 and 2042 – 2077 periods compared with the base period, 1970 – 2005 and (iii) to quantify the impact any changes may have on mean wind speed, wind power and wind power ramps events under future projected climate change.

6.2. DATA

This study uses near-surface wind speed and MSLP data from downscaled GCMs, produced from the Coordinated Regional Downscaling Experiment (CORDEX). CORDEX was a globally coordinated project that produced simulated future climate data using several GCMs which were then downscaled using different RCMs. Different initialization state and physical parameterizations were used to generate ensemble predictions of the future climate. The aim of the CORDEX project was to generate regional-scale climate projections for impact assessment and adaptation studies worldwide, and the data are available from the Earth System Grid Federation (ESGF) LIU portal [192]. The European CORDEX (EU-CORDEX) model outputs which are available at a spatial resolution of 0.11 degrees (EUR-11, 12.5km) and three-hourly temporal resolution are used in this study [193]. In total, output data from six RCA (ver 4.1) downscaled GCMs for the historical period 1970 – 2005 and the future period from the Coupled Model Intercom-

parison Project Phase 5 (CMIP5), 2006 – 2077 are used (Table 6.1). CMIP5 projections are made using different Representative Concentration Pathway (RCP) scenarios, and in this study, the medium RCP scenario, RCP4.5, is used. The RCP4.5 scenario results in an increase of global temperature of about 2°C at the end of 21st century [194]. The dataset is split into three periods, 1970 – 2005 (referred to henceforth as P-0), 2006 – 2041 (P-I), and 2042 - 2077 (P-II).

For this study, wind speed and wind power values were calculated based on the three-hourly data for each of the six models in Table 6.1. These values were also averaged over the six models and are henceforth referred to as ensemble averages.

Table 6.1: CORDEX downscaled GCMs by RCA (ver.4.1) and the downscaled ensemble members.

Driving Model	Calendar days	Ensemble[a]	References
CNRM-CERFACS-CNRM-CM5 (CNRM)	366	r1i1p1	[195]
ICHEC-EC-EARTH (ICHEC)	366	r12i1p1	[196]
IPSL-IPSL-CM5A-MR (IPSL)	365	r1i1p1	[197]
MOHC-HadGEM2-ES (MOHC)	360	r1i1p1	[198]
MPI-M-MPI-ESM-LR (MPI)	366	r1i1p1	[199]
NCC-NorESM1-M (NCC)	365	r1i1p1	[200, 201]

[a] rN is the index of ensemble members, iN is the index of initialization states, and pN corresponds to the index of physical parameterizations used.

6

6.3. METHODS

6.3.1. WIND POWER ESTIMATION

The CORDEX wind speed data are provided at 10m above the surface. The wind speed is extrapolated to a hypothetical turbine hub height of 100m using the log law following the example of other researchers e.g. [202]. The surface roughness length is chosen as 0.0002m to be representative of the open sea as this work is primarily focused on offshore wind power.

The extrapolated wind speed value is used to estimate wind power production by using a hypothetical 8MW power curve [203]. The power curve has a cut-in wind speed of 4m/s, a rated wind speed of 12.5m/s, and a cut-out wind speed of 25m/s. To simplify the analysis of wind power production and wind power ramps characters, the wind power is normalized to the rated power to generate a capacity factor.

6.3.2. DETECTION OF WIND POWER RAMPS

In chapter 3, a novel approach was proposed employing wavelets in conjunction with randomly shuffled surrogates. The approach was illustrated using observational data from the Belgian aggregated offshore wind farms. We have adopted this approach for the present study which involves using a wavelet transformation of a time series of wind power capacity factor values and a large number of randomly shuffled data realisations. The wavelet coefficients from the random realisations are used to discriminate the wavelet coefficients of the original time series based on a maximum wavelet scale (a_{max}) and a

discrimination level (W_T^*). In Figure 6.1, four examples are shown for the detection of ramp events based on a maximum wavelet scale a_{max} = 20 and four discrimination levels of W_T^*. It can be seen that by reducing the value of W_T^* from 10% to 1%, fewer ramps are detected. In this study, we use a discrimination level of W_T^* = 5% to provide a good balance between detecting a power ramp event whilst excluding uncorrelated random fluctuations.
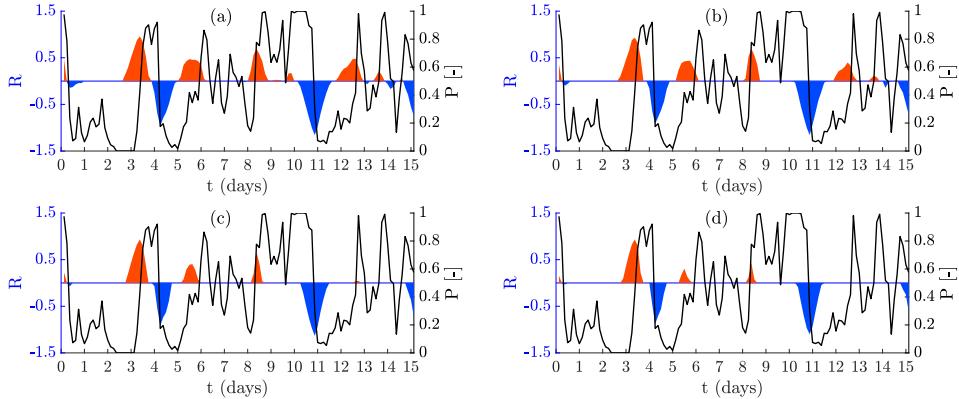

Figure 6.1: Normalised wind power ramps (R) from 15 to 31 December 2005 based on a sample of three-hourly CORDEX downscaled CNRM data. Ramps are detected using a wavelet-surrogate method with a maximum wavelet scale value of a_{max}=20 and discrimination levels, W_T^* of: (a) 10% (b) 5% (c) 2% and (d) 1%. Ramp up events are shown in red and ramp down events in blue.

6.3.3. CLUSTERING OF WEATHER PATTERNS

Based on the results of Chapter 5, we used a SOM to cluster three-hourly CORDEX MSLP data into 30 distinct weather patterns using the SOM_PAK software package [168]. The MSLP output data from each of the six downscaled GCMs for the full period, 1970 – 2077 were first concatenated. They were then fed into the software sequentially, and the SOM neuron weights initialized randomly from the spatial MSLP data. Sequential training was carried out in two phases. The first phase, known as rough training, was used to arrange the weight vectors of the SOM neurons topographically. This training phase used a large initial learning rate (α_0 = 0.05) and neighborhood radius size (σ_0 = 6). With training time, both values were decreased linearly as a function of iteration time which was set to about 400,000 time steps. In the fine-tuning phase, training was initialised using the output from the rough training phase. In this phase, a smaller initial learning rate (α_0 = 0.02) and neighborhood radius size (σ_0 = 3) were used which were also decreased linearly. Finally, a Sammon mapping projection [169] was used at different iteration steps until the neurons were not twisted, which indicated that the SOM was trained sufficiently.

Once the topological order of the weight vectors was determined, the best matching unit corresponding to the input data was determined based on the minimum Euclidean distance between the weight of the neurons and the input data vectors.

6.4. SOM-BASED WEATHER PATTERNS

Figure 6.2a shows the 30 generated weather patterns. Due to the nature of a SOM, similar circulation systems cluster close together on a map. Many weather patterns show distinct circulation types, *e.g.*, cyclonic, anti-cyclonic, zonal, and meridional flow. At the top of the map, the weather patterns are dominated by meridional flow (b1) and high-pressure systems (c1, d1, e1 and f1). Weather patterns at the bottom of the map are mainly characterised by low-pressure systems (a5 – d5). Weather patterns to the left of the map are mainly characterised by northeasterly flow (a1 and a3) with low pressure over Scandinavia. Weather patterns on the right are characterised by southwesterly flow (f4 and f5) with high pressure over the European continent and Scandinavia. The most distinct weather pattern systems are located at the edges of the map.

Figure 6.2b shows the percentage frequency of occurrence of each weather pattern. Figure 6.2c shows the distribution of the duration of weather pattern events based on consecutive three-hourly values for the four most frequently occurring weather patterns, i.e. d1, a2, b5 and f5. The longest weather pattern events persist for 14 days but those that persist more than six days rare. Furthermore, Figure 6.2d shows the percentage fraction (Frac) of events by weather pattern that persist for at least 24 hours, *i.e.* nine or more consecutive three-hourly values. This is given by the fraction of weather pattern events to the right of vertical dashed blue line in Figure 6.2c. Weather patterns located at the edges of the map such as weather patterns b5, f5, a3, d1, and a2 tend to occur more frequently and with greater persistence than the weather patterns at the center. These outer weather patterns tend to be associated with quite distinct circulation features with relatively strong pressure gradients. The central weather patterns display weaker pressure gradients, and their lower persistence suggests that they are more likely to be transition states between the outer weather patterns in the map.

6
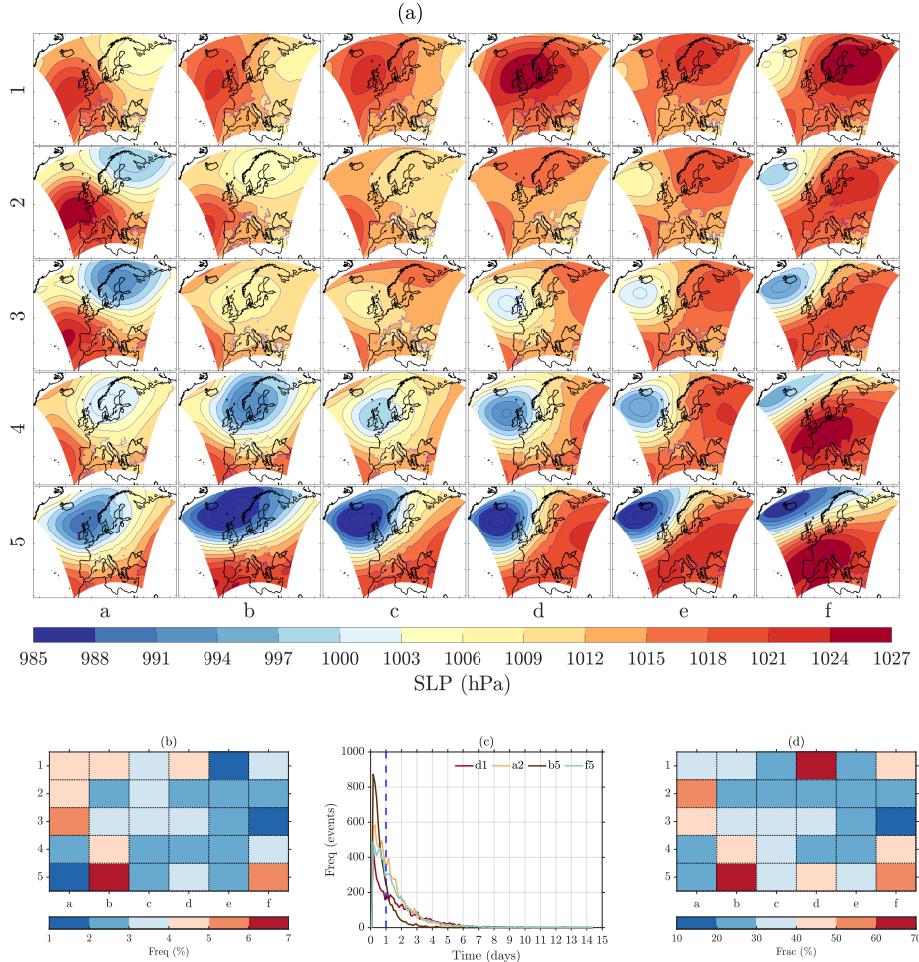
Figure 6.2: SOM-based weather patterns: (a) clusters based on three-hourly MSLP, 1970 – 2077. The shaded color is the MSLP in hPa and the contour line is MSLP in 3hPa intervals, (b) frequency of occurrence in (%), (c) distribution of the duration of events corresponding to weather patterns d1, a2, b5 and f5, and (d) fraction (%) of events where a weather pattern persists at least 24 hours. The vertical dotted blue line in (c) shows the threshold used to calculate the fraction of events in (d). N.B. The rows (1 – 5) and columns (a – f) are used to label weather patterns.

6.5. Projected future SOM-based weather patterns changes

Figure 6.3a, 6.3b and 6.3c show the absolute frequency of weather patterns in the P-0, P-I and P-II periods, respectively. Figure 6.4(a) and 6.4 (b) show the projected fractional change in weather pattern frequency in P-I and P-II, respectively, relative to P-0. Overall, comparing the two future periods, the projected change of weather pattern frequency is greater in P-II compared to P-I. The weather patterns that are mainly located at the

top and right, which are characterised by high-pressure and southwesterly flow, show an increasing tendency. On the other hand, most of the weather patterns that are located around the center and some of the weather patterns that are located at the bottom are characterised by a weak spatial pressure gradient and low-pressure systems. These weather patterns show a decreasing tendency in the future climate.
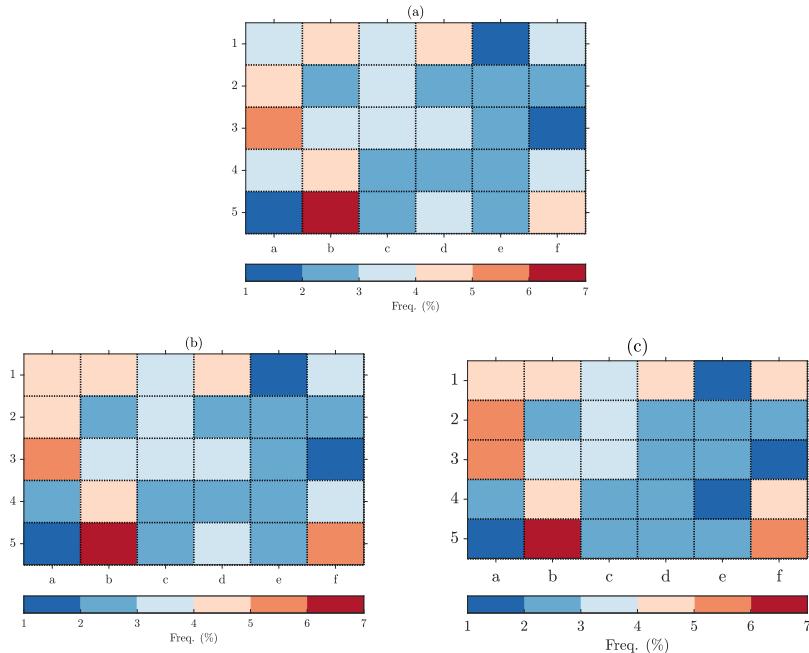

Figure 6.3: Frequency of weather patterns in the: (a) P-0, (b) P-I and (c) P-II periods.

Figure 6.4(c) and 6.4(d) show the change in the fraction of weather patterns which persist at least 24 hours for the two periods, P-I and P-II, relative to P-0 . Overall, a similar trend is seen, though some differences are seen near the top of the map. For example, weather patterns c1 and e1 show an increasing frequency based on all three-hourly values, whereas the corresponding weather patterns that persist at least 24 hours show a decreasing trend for c1 and for e1 an increase in P-I and a decrease in P-II.

To further investigate the consistency of the temporal changes, trends are analysed on a yearly basis in Figure 6.5. Figure 6.5(a) shows the change in weather pattern frequency per year over the entire study period based on all three-hourly values, and Figure 6.5(b) shows the same information but for weather patterns persisting at least 24 hours. Those patterns where the trend is significant at the 5% level are indicated. Weather patterns that are located at the left, top, and bottom right, with dominant high pressure systems centred to the west and south of Europe show a significant increasing trend, whereas those with a significant decreasing trend are located at the center and bottom of the map which tend to have a either weak pressure gradient or are dominated by low

6
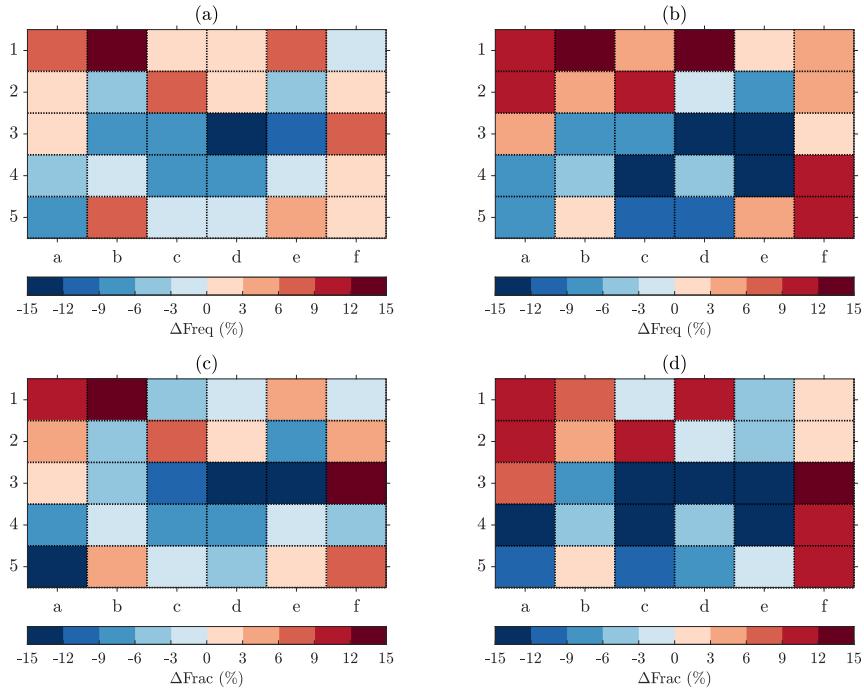
Figure 6.4: Projected changes in SOM-based weather pattern occurrence relative to P-0: (a) change in weather pattern frequency in P-I, (b) same as (a) but in P-II, (c) change in the fraction of of events where a weather pattern persists at least 24 hours. in P-I ; (d) same as (c) but in P-II.

pressure systems centred to the west of Europe.

For two of the weather patterns that show a significant increasing and decreasing trends, a yearly plot is shown. Figures 6.5c and 6.5d show the annual frequency per year of weather patterns d1 (a pattern dominated by high pressure) and d3 (a pattern with a relatively weak low pressure system) based on all values and where a pattern persists for at least 24 hours, respectively. The trends are clear for both weather patterns though there is a large degree of inter-annual variation.
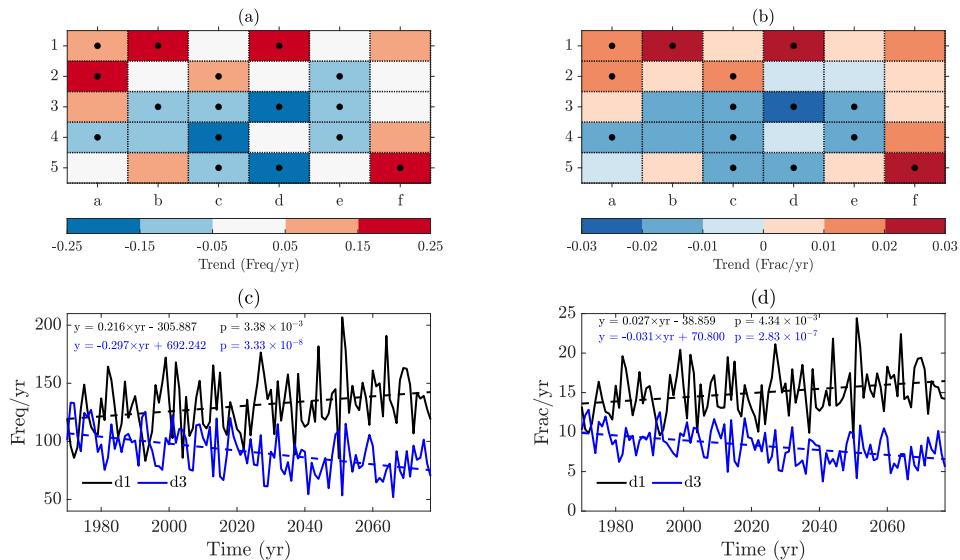

Figure 6.5: Based on the whole study period: (a) change in weather pattern frequency per year based on all three-hourly data, (b) as (a) but for events of a particular weather pattern that persist for at least 24 hours, (c) annual frequency/year for patterns d1 and d3 based on all three-hourly values, and (d) as (b) but for events of a particular weather pattern that persist for at least 24 hours. The dots in (a) and (b) represent where the p-value of the trend <0.05.

6.6. FUTURE WIND POWER PRODUCTION AND WIND POWER RAMPS

6.6.1. PROJECTED CHANGES IN WIND POWER PRODUCTION

Capacity factors were first calculated based on the wind speed values from each of the six downscaled models in Table 6.1 and then a mean of these values evaluated from the ensemble of the six. Figure 6.6(a) shows the six-model ensemble capacity factor over the North Sea for P-0. Five grid points close to offshore wind farm locations are selected to analyze the temporal trend and variability of the wind power capacity factor over the North Sea area in more detail and these are marked on the map as: S1 (Belwind), S2 (Borssele), S3 (Hornsea 1), S4 (Gode Wind 1 and 2) and S5 (Horns Rev 3). In order to show the level of inter-annual variability, Figure 6.6(b) shows the annual capacity factor and trend line over the period 1970 – 2077 for S2. Furthermore, for each of the sites S1 to

S5, a trend line is fitted to the mean annual capacity factors and the slope along with the p-value of the fit (in brackets) is shown in Table 6.2.
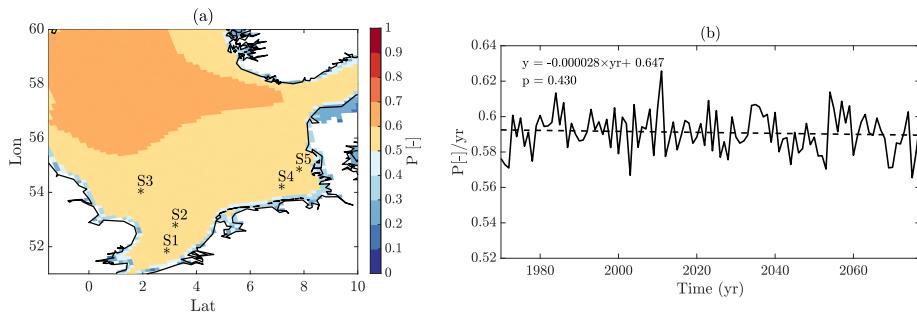

Figure 6.6: (a) Spatial map of capacity factor based on mean wind speed values from the ensemble of the six downscaled models in Table for P-0 showing grid points close to offshore wind farm locations S1–S5, and (b) yearly ensemble values of the capacity factor for S2 for the whole study period 1970 – 2077 showing the best fit linear trend and significance level.

Figures 6.7a and 6.7b show the change in MSLP over Europe for the P-I and P-II periods, respectively, compared with the base period. A progressive increase in pressure is seen over the Atlantic extending over the continent and the North Sea region with reducing pressure over north-eastern Europe.

Figure 6.7c – 6.7f shows the change in wind speed and capacity factor over the North Sea region for P-I and P-II relative to P-0 based on the mean six model ensemble wind speed values. For P-I, Figure 6.7c shows an increasing trend in wind speed over the south, southeast, and east of the region and a decreasing trend over the north and northwest. By contrast, for P-II, Figure 6.7d shows wind speed strongly decreasing over the north and northwest, and a weaker increase over the south, southeast and east of the region. This is consistent with the change in MSLP where during P-I, the increase in pressure in the Atlantic initially contributes to an increase in pressure gradient which then weakens over the western North Sea during P-II once the increase in pressure becomes more widespread over the continent.

Figure 6.7e and Figure 6.7f, show the corresponding projected changes in capacity factor for P-I and P-II, respectively. It can be seen that the trends are similar though slightly less pronounced than the spatial changes in wind speed due to the non-linear nature of the power curve where power output is constant over the range of wind speeds between rated and cut-out.

Figure 6.8 compares the annual capacity factor for each model based on the grid point closest to S2. In each case, a best fit linear trend line is shown along with its p value. CNRM, IPSL, MOHC and NCC show no signicant trend, but ICHEC and MPI show declining values with p values < 0.05. It is also notable that IPSL gives annual capacity factor values which are significantly lower than the other models.

The best fit linear trend line and significant level (p) are calculated for all the sites S1 to S5 for the ensemble and individual models as shown in Table 6.2. For the capacity factors calculated based on the mean model ensemble wind speed values, there is no significant trend for any of the sites. It shows a declining trend for all sites though it is not
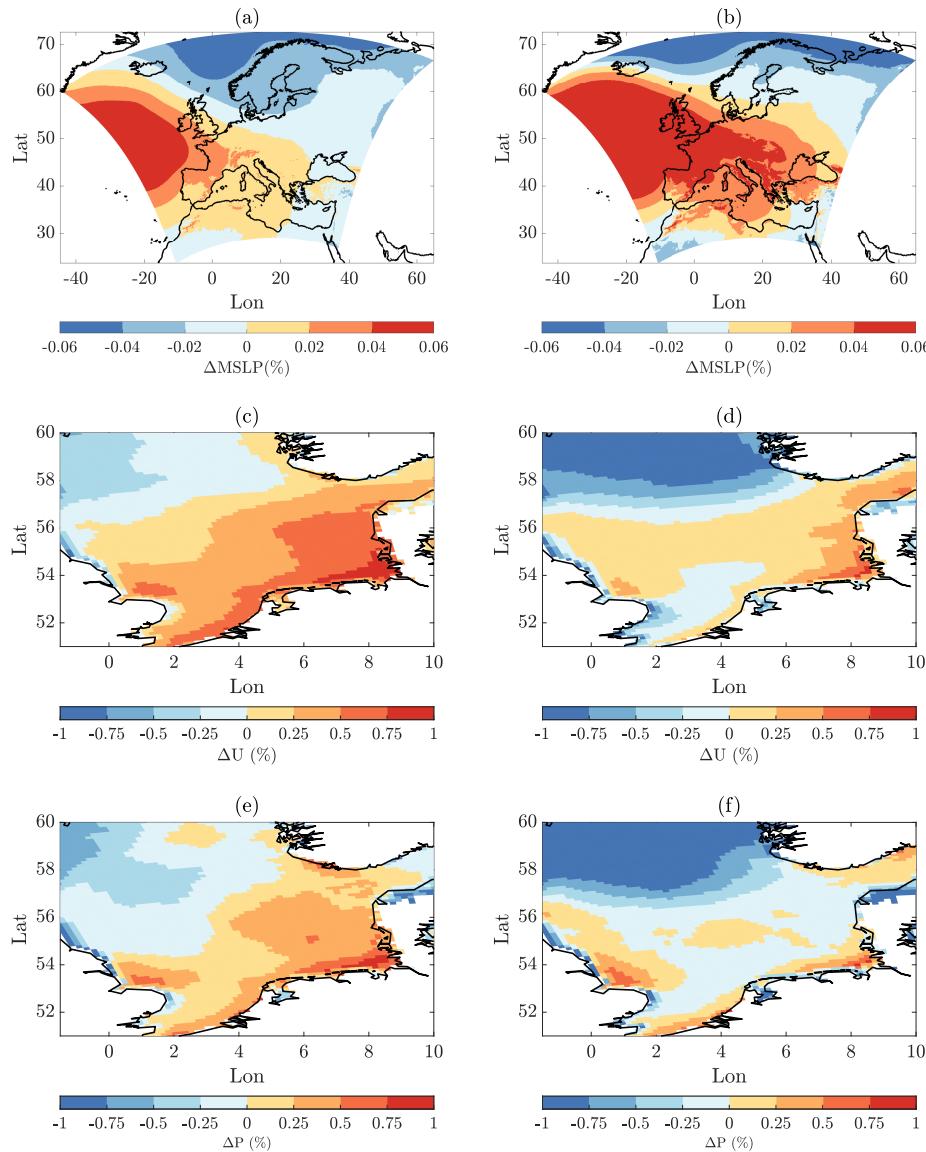
Figure 6.7: Projected change relative to P-0 in: (a) average mean sea level pressure for P-I, (b) average mean sea level pressure for P-II, (c) average wind speed for P-I, (d) average wind speed for P-II, (e) average capacity factor for P-I, and (f) average capacity factor for P-II,. All values are based on mean values from an ensemble of the six models in Table 6.1.
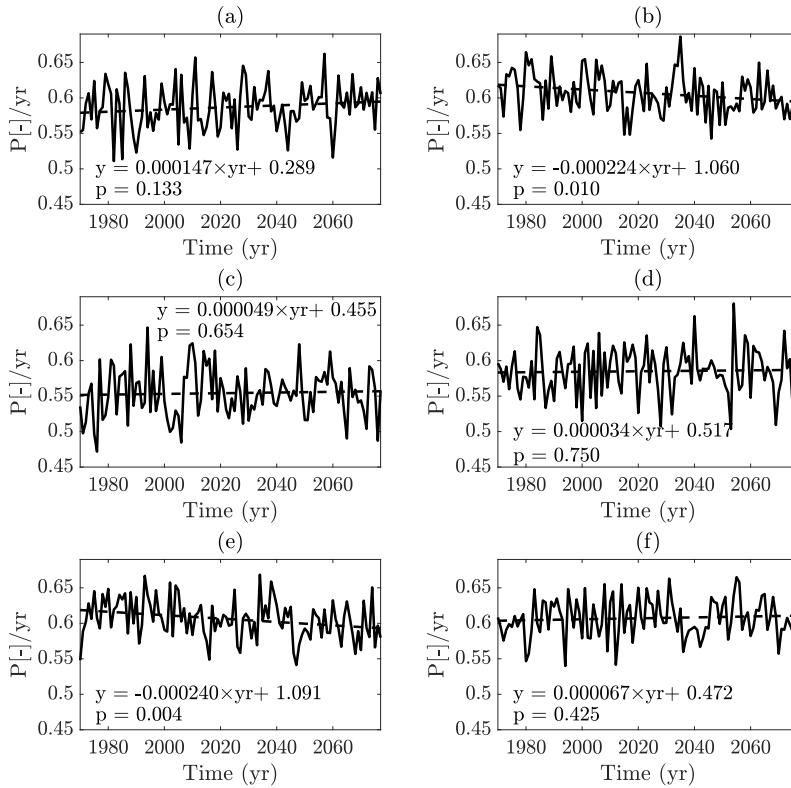
Figure 6.8: For the grid point closest to site S2, the best fit trend-line, equations and p-value values of wind power capacity factor for models: (a) CNRM, (b) ICHEC, (c) IPSL, (d) MOHC, (e) MPI, and (f) NCC are shown.

significant. With the exception of ICHEC and MPI, all models show a slight increasing trend though this is not significant. ICHEC shows a significant declining trend ($p < 0.05$) for all sites and MPI shows a significant declining trend for S2 and S3. The disagreement between the models is likely associated with differences in GCM numerics and physical parameterizations which is outside the scope of this study.

Table 6.2: The best-fit linear trend ($\times 10^{-5}$) and p-values based on the capacity factor over the entire study period for each model at sites S1 to S5. The text in bold indicates that the estimated slope is significant at $p<0.05$ where the p-values are shown in parentheses.

Models	S1	S2	S3	S4	S5
Ensemble	-1.8(0.656)	-2.8(0.430)	-8.0 (0.793)	-2.1 (0.589)	-5.0(0.890)
CNRM	16(0.116)	14.7(0.133)	11.9(0.185)	14.2(0.121)	10.6(0.230)
ICHEC	**-22.4(0.013)**	**-22.4(0.010)**	**-22.2(0.009)**	**-19.9(0.015)**	**-24.2(0.03)**
IPSL	8.1(0.560)	4.9(0.654)	13.3(0.188)	19.0(0.102)	21.3(0.062)
MOHC	2.1(0.850)	3.4(0.750)	0.8(0.935)	5.0(0.635)	3.0(0.062)
MPI	-17.0(0.053)	**-24.0(0.004)**	**-19.6(0.019)**	14.6(0.127)	16.4(0.091)
NCC	2.5(0.781)	6.7(0.425)	10.7(0.193)	8.7(0.373)	8.8(0.362)

6

6.6.2. PROJECTED CHANGES IN WIND POWER RAMPS

Wind power ramps were calculated following the procedure described in Section 6.3.2. First, the capacity factor was calculated for each model, then the total number of ramps per year was calculated for each model and from this an ensemble average was determined. Figure 6.9a - 6.9d shows spatial maps over the North Sea of the projected change in the ensemble averaged ramp up and ramp down frequency for P-I and P-II compared to P-0. The maps indicate a decreasing trend in wind power ramps over some of the North Sea region especially off the eastern coast of the UK and the Dutch coast. The trend for ramp up and ramp down events is similar. For site S2, the annual frequency of ramp up and ramp down events is shown in Figure 6.9e for the entire study period. The trend lines are clearly negative and significant at p<0.05 despite some degree of interannual variability.
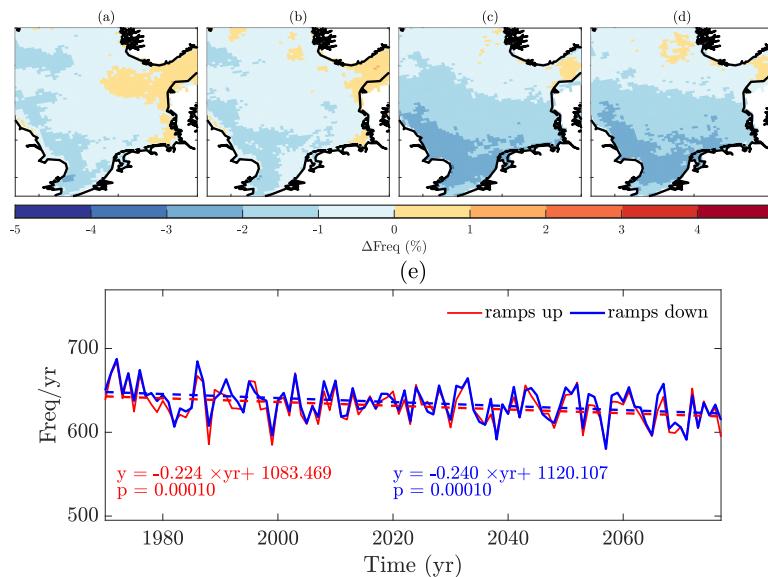

Figure 6.9: Projected changes compared to P-0 in model ensemble wind power ramp frequency: (a) ramp up events for P-I, (b) as (a) but for ramp down events, (c) as (a) but for P-II, (d) as (c) but for ramp down events; and (e) annual ramp up and ramp down event frequencies at site S2 with best fit linear trend-line and p-value.

Figure 6.10 shows the annual ramp frequency for each individual model for site S2. All but one of the models (i.e. except NCC) show declining trends for ramp up and ramp down events over the study period. ICHEC, IPSL and MOHC show significantly declining ramp up events with $p < 0.05$ and CNRM, IPSL, MOHC and MPI show significantly declining ramp down events (there is some difference between the models in terms of the absolute number of ramp events with CNRM giving the most and IPSL the least).

Tables 6.3 and 6.4 summarise the best fit trend line slopes to the annual ramp up and ramp down event frequencies, respectively, over the study period for each of the sites S1 – S5 by model and for the ensemble. For all sites, the ensemble average trend shows a significant decline where the p value < 0.05. All of the sites show significant

declining trends according to at least some of the models, though not the majority. The NCC model shows some evidence of increasing frequency at certain sites and site S5 (the most easterly site) also shows evidence of an increasing ramp up and ramp down frequency for some models, but neither of these trends is significant.
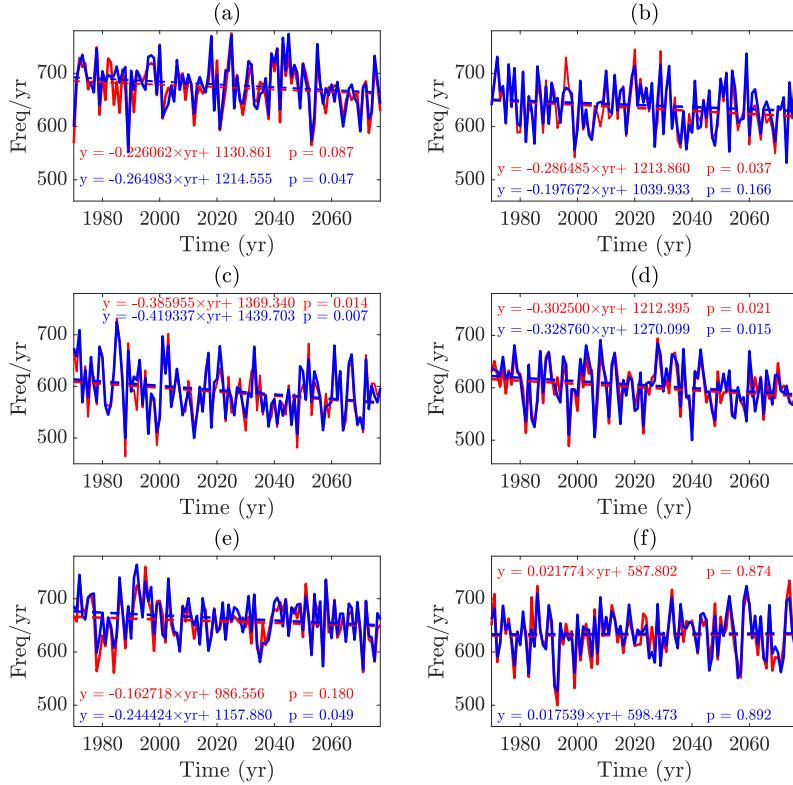

Figure 6.10: Annual wind power ramp up (red) and ramp down (blue) event frequencies for site S2, with best fit linear trend line and p-value of estimated slope based on data from the models: (a) CNRM, (b) ICHEC, (c) IPSL, (d) MOHC, (e) MPI, and (f) NCC.

Table 6.3: Annual wind power ramp up frequency trend line slope and p-value (p) in parentheses by model for sites S1 to S5. The bold text indicates the estimated slope has a significant level p<0.05.

Models	ramp up events				
	S1	S2	S3	S4	S5
Ensemble	**-0.215(0.00004)**	**-0.224(0.00010)**	**-0.225(0.00047)**	**-0.147(0.00175)**	**-0.162(0.00984)**
CNRM	**-0.327(0.016)**	-0.226(0.087)	-0.111(0.386)	-0.035(0.796)	-0.109(0.409)
ICHEC	-0.161(0.223)	**-0.286(0.037)**	**-0.292(0.033)**	-0.315(0.050)	**-0.339(0.023)**
IPSL	**-0.462(0.003)**	**-0.386(0.014)**	**-0.323(0.030)**	-0.277(0.071)	-0.209(0.187)
MOHC	**-0.327(0.016)**	**-0.303(0.021)**	-0.222(0.110)	**-0.375(0.010)**	**-0.361(0.014)**
MPI	-0.146(0.239)	-0.163(0.180)	-0.250(0.055)	-0.052(0.652)	0.007(0.948)
NCC	0.133(0.313)	0.022(0.874)	-0.154(0.256)	0.169(0.216)	0.042(0.747)

Table 6.4: Annual wind power ramp down frequency trend line slope and p-value (p) in parentheses by model for sites S1 to S5. The bold text indicates the estimated slope has a significant level p<0.05.

Models	ramp down events				
	S1	S2	S3	S4	S5
Ensemble	**-0.232(0.00004)**	**-0.240(0.00010)**	**-0.202(0.00047)**	**-0.184(0.00984)**	**-0.142(0.00984)**
CNRM	**-0.352(0.013)**	**-0.265(0.047)**	-0.090(0.493)	-0.044(0.739)	0.104(0.431)
ICHEC	-0.133(0.344)	-0.198(0.166)	-0.244(0.077)	-0.295(0.060)	**-0.315(0.031)**
IPSL	**-0.449(0.003)**	-0.419(0.007)	**-0.314(0.027)**	**-0.368(0.020)**	-0.127(0.411)
MOHC	**-0.389(0.003)**	**-0.329(0.015)**	-0.187(0.187)	**-0.373(0.008)**	**-0.389(0.007)**
MPI	-0.012(0.920)	**-0.244(0.049)**	**-0.312(0.017)**	-0.172(0.149)	0.023(0.833)
NCC	-0.058(0.651)	0.018(0.892)	-0.062(0.641)	0.148(0.254)	0.062(0.620)

6

6.7. The impact of future weather pattern changes on wind power and wind power ramps

This section looks at how different weather patterns contribute to wind power production and wind power ramps and how this is projected to change in the future.

6.7.1. Impact on wind power

Figure 6.11(a) shows how annual energy production (AEP) is distributed amongst the different weather patterns for S1 – S5. The AEP values are calculated based on the wind speed distribution for each weather pattern and the 8MW wind power curve. This is converted to AEP (%) by dividing by the total production across all weather patterns and converting to a percentage. It is notable that a large fraction of the AEP (10%) is associated with pattern b5. This comprises a very strong low pressure system north of Europe with strong westerly winds. Pattern a3 with a strong south-west to north-east pressure gradient and north-westerly winds also contributes a significant fraction to overall AEP. Figure 6.11(b) and Figure 6.11(c) show the projected changes in the distribution of AEP for P-I and P-II, respectively. The most significant change in P-I is an increase in the contribution to AEP by b5. The weather patterns in the middle row of the SOM show primarily reducing contributions to AEP. The changes seen during P-II show interesting trends. In this case, the AEP contribution from b5 is hardly different to P-0. Much of the AEP has been redistributed in the form of an increase associated with patterns a2 (similar circulation pattern to a3, but with the high over the Atlantic and the low over Scandi-
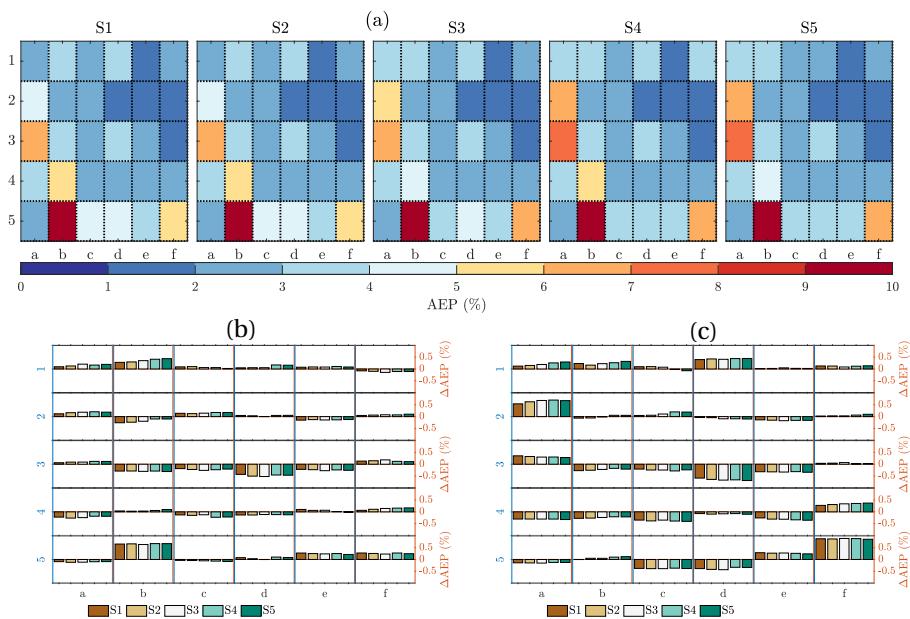
Figure 6.11: (a) Distribution of the annual energy production (AEP) by weather pattern for S1 – S5 in P-0 , (b) projected change for P-I, and (c) as (b) but for P-II.

navia displaced more to the north-east) and f5 (similar circulation pattern to b5 but with the high over southern Europe and the low north of the UK displaced further north) balanced by a decrease across the third and fourth rows of the SOM, in particular d5 (similar circulation pattern to b5 but with the high over southern Europe displaced more to the east and the low north of the UK displaced more to the west, so winds move from being mainly westerly to more south-westerly). Trends across the sites S1 – S5 are very similar. These trends broadly reflect the changes in occurrence of the different weather patterns observed in Figure 6.4.

6

6.7.2. IMPACT ON WIND POWER RAMPS

Figure 6.12a shows the distribution of ramp up events during P-0 by weather pattern for
sites S1 – S5. The greatest single number of ramp up events is seen for class f5. This is a
relatively frequently occurring pattern as seen in Figure 6.4, however, not as frequent as
the similar pattern b5 which contributes far fewer ramp up events. Weather patterns in
the centre of the SOM with weak pressure gradients are also associated with a relatively
large number of ramp up events. Weather patterns dominated by high pressure systems,
and thus low wind speeds, seen at the top right of the SOM, are associated with relatively
few ramps and also contribute little to AEP as seen in Figure 6.11(a). Figure 6.12b shows
the change in ramp up event distribution for P-I. The most notable change is a reduc-
tion in the occurrence of ramp up events associated with weak pressure gradients in the
centre of the SOM. For period P-II, shown in Figure 6.12c, the trend is similar, with addi-
tional significant decreases in contributions from c4 and d5 where winds are driven by
low pressure systems. An increase in ramp-up events is seen for the first row of the SOM
with high pressure dominated systems and periods of low production. Trends across the
sites S1 – S5 are broadly similar.
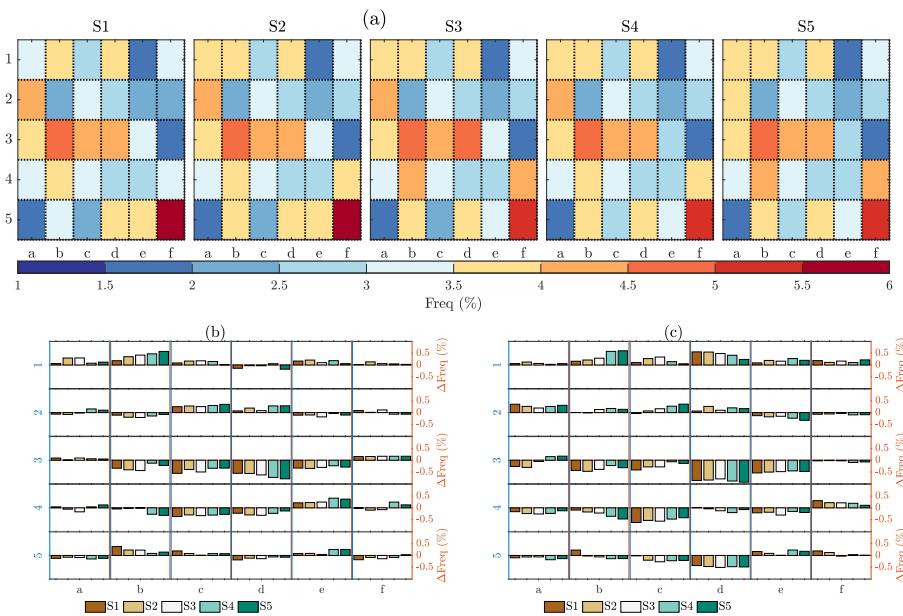
Figure 6.12: (a) Distribution of ramp up events by weather pattern for S1–S5 in P-0, (b) projected change for
P-I, and (c) as (b) but for P-II.

Figure 6.13a shows the distribution of ramp down events during P-0 by weather pattern for sites S1 – S5. Trends are similar as the ramp down events seen in Figure 6.12a, though there is a larger proportion of ramps associated with weather patterns at the top and left of the SOM, especially a2, a3 and b4. These patterns are associated with relatively strong north-westerly winds and weakening low pressure systems which are known to contribute to ramp down events [23, 31, 204]. Figure 6.13b and Figure 6.13c show the changes projected for P-I and P-II, respectively. The changes seen are very similar to those expected for ramp up events in 6.11(b) and 6.11(c)
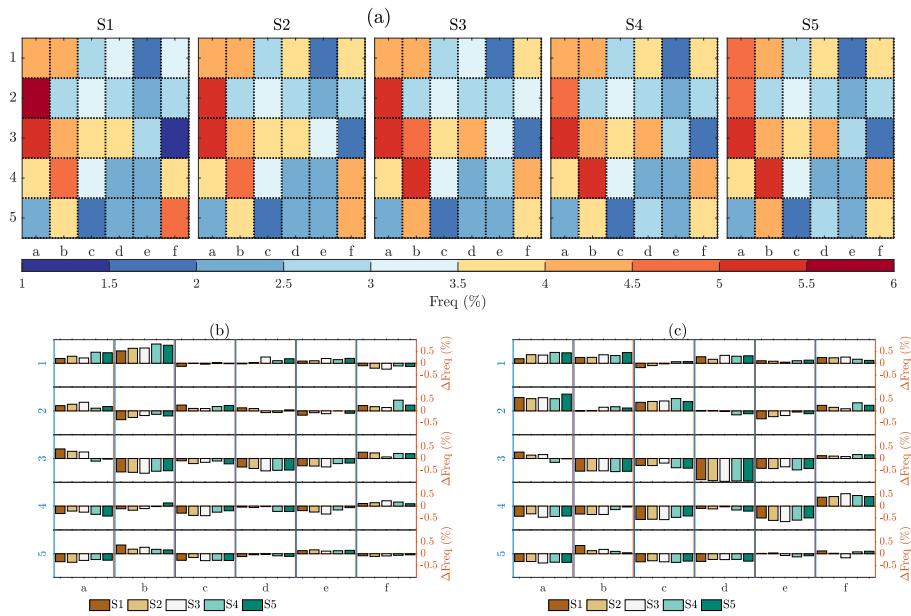

Figure 6.13: (a) Distribution of ramp down events by weather pattern for S1–S5 in P-0, (b) projected change for P-I, and (c) as (b) but for P-II.

6.8. DISCUSSIONS

Before concluding this chapter, we would like to point out a few limitations of the present study.

6.8.1. VERTICAL EXTRAPOLATION OF NEAR-SURFACE WIND SPEEDS

In this study, we make use of wind speed data from the Euro-CORDEX project and only consider the RCP45 scenario. Even though for other projection scenarios (e.g., RCP26 and RCP85), the Euro-CORDEX database provides 100m wind speed values, similar high-altitude data are not available for the RCP45 case. Thus, we had to extrapolate the 10m wind speed values to 100m, which is the hub height of a hypothetical wind turbine. We used the adiabatic logarithmic law of the wall, that is only valid for neutrally stratified conditions. For non-neutral conditions, one should use either the Monin-Obukhov (M-O) similarity formulation or one of its generalizations (e.g., [205]). Another viable approach would be to use the so-called geostrophic drag laws (e.g., [206]). For stable conditions, the boundary layer height could be very shallow. Furthermore, low-level jets are often present under stably stratified conditions. For such cases, the existing similarity formulations perform rather poorly (see [207] and the references therein). Given that the M-O and geostrophic drag law formulations require additional input variables (e.g., momentum flux, sensible heat flux, geostrophic wind speed), for simplicity, we opted to use the adiabatic logarithmic law in this study.

6

6.8.2. NOTABLE DIFFERENCES IN CMIP5 AND CMIP6 DATASETS

All the statistical analyses of the present study are based on the Euro-CORDEX dataset downscaled from the CMIP5 runs. Recently, coarse-resolution data from the next-generation CMIP6 project have become publicly available. A few studies [208–210] have already compared the trends of projected wind power production based on CMIP5 and CMIP6 datasets. Several significant differences have been reported. For example, in contrast to CMIP5, CMIP6 predicts a decline in wind resources for Northern Europe and most of Europe by the end of the century (SSP5 - 8.5 scenario). At the same time, CMIP6 shows an increase in wind resources during future summers in some regions of southern Europe, whereas CMIP5 projects the opposite trend.

To the best of our knowledge, recent studies have yet to investigate the trends of wind ramps in CMIP6. Once downscaled (high-resolution) CMIP6 datasets become available, we will investigate this problem and revisit other science questions addressed in our current study.

6.8.3. THERMODYNAMIC EFFECTS

The change in projected wind energy is influenced not only due to the change in dynamics of large-scale meteorological systems but also determined by atmospheric thermodynamics. Ohba [187] investigated the influence of thermodynamics when studying wind ramp phenomena over Japan. In our future work, we intend to extend the current study to include thermodynamical influences.

6.9. Conclusions and recommendations

In this work, future changes in weather pattern occurrence, wind power production and wind power ramps have been analysed based on CORDEX data derived from the output from an ensemble of model chains used as part of CMIP5 to predict the future regional climate under the RCP4.5 scenario. A SOM was used to classify MLSP data into 30 discrete weather patterns to better understand the association between circulation patterns and wind power production and wind power ramps. The CORDEX data analysed were divided into three periods: a historic period (P-0), a near future period (P-I) and a far future period (P-II).

An increase was projected in the occurrence of weather patterns associated with high-pressure systems and north-easterly flows. By contrast, there was projected to be a reduction in the frequency of weather patterns associated with low-pressure systems and weak spatial pressure gradients.

Five North Sea sites characteristic of offshore wind farms were chosen to further study the spatial characteristics of wind power production and wind power ramps. Overall, based on the CMIP5 model ensemble, no significant change in wind power capacity factor was seen over the entire study period (P0, P-I and P-II), although there was tentative evidence of a reduction in wind power ramps.

Annual energy production is projected to be dominated by a small number of weather patterns with westerly, south-westerly or north-westerly winds. Changes in patterns of production in a future climate are not entirely monotonic, but production is projected to become less from westerly winds and more from south-westerly and north-westerly flows.

Ramp up events are primarily associated with strong south-westerly winds or weather patterns with a weak pressure gradient. Ramp down events have a stronger association with more north-westerly flow. The most notable change in a future climate is a reduction in ramp up events associated with weak pressure gradients.

The findings of this work are based on the assumption that a fixed number of weather patterns can be used to classify circulation patterns which are valid over a long period where the climate is changing. Further work is required to determine the validity of this assumption.

7

CONCLUSIONS AND RECOMMENDATIONS

Research is something that everyone can do, and everyone ought to do. It is simply collecting information and thinking systematically about it.

Raewyn Connell(January 03, 1944)

This chapter summarizes the findings, limitations, and recommendations of the thesis. The response to research questions presented in chapter 1 in Section 1.6 are briefly explained.

7.1. FINDINGS AND CONCLUSIONS

Offshore wind power will supply a substantial proportion of energy in the future. The North Sea is the largest potential source of offshore wind power for several European countries. For this reason, this study has used the North Sea region as a case study to investigate the characteristics of wind power generation and wind power ramps in the present and future climate. This thesis has looked at: modelling and forecasting of wind power and wind power ramps; detection of wind power ramps, association of wind power and power ramps with weather patterns; and anticipated changes in wind power output and wind power ramps in the future. Four research questions were posed in Section 1.6; the response to each of these research questions is addressed in the following subsections.

7.1.1. CAN AN ALGORITHM BE DEVELOPED TO DETECT WIND POWER RAMPS OVER A RANGE OF DURATIONS?

Wind power production is distinguished by wind power ramps, which are temporal increases or decreases in wind power output. To distinguish wind power ramp events, many algorithms have been developed. Nonetheless, as stated in Section 3.1, most of these algorithms have one or more shortcomings.

A novel wind power ramp identification method, based on a wavelet-surrogate (WS) technique, is suggested in this research. It can identify different ranges of wind power ramp duration and is independent of wind power change in relation to the rated power ΔP. Wavelet coefficients of temporal wind power generation and multiple randomly shuffled wind power wavelet coefficients are used to differentiate ramp events using the original wavelet coefficients at a specified discrimination level. The sign of the discriminating wavelet coefficient (section 3.4) determines the direction of the wind power ramp.

The newly developed wavelet-surrogate method is evaluated by detecting wind power ramps from a wind power generation time series based on a fleet of turbines with varying total rated power over time. The method was used to discriminate a range of ramp rates of different duration. It is proposed that this approach improves on existing wind power ramp detection methods with its ability to detect ramps of arbitrary rate and duration, independent of total power capacity.

7.1.2. DO DEEP LEARNING MODELS HAVE THE POTENTIAL TO IMPROVE WIND POWER AND POWER RAMP MODELLING AND FORECASTING?

In this work, deep-learning neural network models were used to see how well they could enhance numerical weather prediction forecasts comparing GFS forecast model data as input with the ERA5 reanalysis which represents, as far as possible, the 'ground truth'. The enhanced forecasts were benchmarked against a simple empirical power curve generated using historical data. The neural network architectures employed in this study

were a multilayer perceptron (MLP), convolutional neural network (CNN), residual network (ResNet), and inception network (IN). The capacity of the deep learning models to enhance forecasts of wind power and wind power ramps was investigated. Aside from the GFS and ERA5 reanalysis data, the sin and cosine of the hour, day, and month of the year are used to train, validate, and test the models (Chapter 4) in their ability to forecast power and power ramps for the aggregated Belgian offshore wind farm cluster. The building of deep learning models is not entirely straightforward because the model accuracy depends on the tuning of multiple hyperparameters. With this in mind, model sensitivity to the depth of the neural network and the types of input meteorological variables was investigated.

The performance of the empirical and deep learning models to forecast wind power and power ramps was evaluated using different error metrics. Wind power ramp forecasts were directly derived from the absolute wind power forecast models. In general, the deep learning models outperform the empirical model in terms of enhancing both wind power and power ramp forecasts. The skill of the deep learning models depends on model input parameters, model grid and sophistication of model architecture. More sophisticated model architectures with additional layers and model ensembles provide more accurate forecasts than simpler models, though gains are relatively modest.

7.1.3. HOW DO WEATHER PATTERNS AFFECT THE MAGNITUDE OF WIND POWER PRODUCTION AND THE CHARACTERISTICS OF POWER RAMPS?

Wind power magnitude and wind power ramps are driven by the dynamics of atmospheric processes. Past studies have shown that different specific weather patterns influence onshore wind power production. In this study, weather patterns over the North Sea have been investigated to see how they influence offshore wind power and wind power ramps using the case of the Belgian aggregated offshore wind farm cluster.

To quantify the association of weather patterns with wind power magnitude and wind power ramp characteristics, thirty distinct European weather patterns were first identified from long-term sea level pressure data using self-organizing maps (SOMs). Selected SOM weather patterns were compared with The Royal Netherlands Meteorological Institute (KNMI) pressure charts for specific time periods and were found to capture well the characteristics of individual events.

The association of these weather patterns with Belgian offshore wind power production and wind power ramps was then quantified. Periods of high wind power production was predominantly related to weather patterns characterised by low-pressure systems and southwesterly wind flow. Northeasterly wind flow was frequently associated with extreme wind speed values with accompanying frontal systems potentially leading to a greater chance of wind turbine cut-out. In contrast, high-pressure systems and low-pressure systems with weak spatial gradients were associated with low wind power capacity factors.

Wind power ramps were found to be mainly related to the transition of weather patterns rather than specific weather patterns themselves. A significant fraction of ramp-up events occurs during weather pattern transition from high-pressure to low-pressure with weak spatial gradient. Whereas ramp-down events occur when weather patterns move from low-pressure to high-pressure systems or low-pressure with a weak spatial gradi-

ent. This study has shown that there is a clear correlation of wind power production and wind power ramp characteristics with specific types of weather patterns, which could be helpful in planning power dispatch.

7.1.4. ARE THERE EXPECTED TO BE CHANGES IN FUTURE PATTERNS OF WIND POWER PRODUCTION AND POWER RAMPS RELATED TO CLIMATE CHANGE?

An ensemble of downscaled general circulation models (GCMs) were used to assess future trends in North Sea offshore wind power power production and wind power ramps using projected future climate data from the CORDEX initiative.

Firstly, changes in the frequency of weather patterns in a future climate was determined, using sea level pressure data from the downscaled future climate simulations. Once again, 30 patterns were identified using a SOM. In a future climate, patterns associated with southwesterly flows, northeasterly flows, and high-pressure systems were seen to increase in frequency and persistence whereas patterns associated with low-pressure systems and low-pressure with a weak spatial gradient will see a decrease.

To examine potential future changes in wind power production and wind power ramps across the North Sea area, wind power production was simulated from the downscaled GCM future projected wind speed values using a hypothetical 8MW rated power wind power curve and wind power ramp events were identified using the wavelet-surrogate technique.

Overall, the wind power generation is expected to reduce across the North Sea region though trends varies geographically. Additionally, differences between the models were seen. The increase in frequency and persistence of weather patterns dominated by high-pressure systems in a future projected climate is primarily responsible for the decline in wind energy generation.

Changes in the frequency of wind power ramps was also quantified. A significant reduction in the frequency of wind power ramps across the North Sea area in the future was projected.

7.2. LIMITATIONS OF THIS STUDY

Four research topics concerning offshore wind power production and wind power ramp characteristics, focusing on the North Sea area, have been addressed in this study. This study used observed wind power, a reanalysis (ERA5), global numerical model data (GFS), and CORDEX downscaled GCM climate projection data. Even though this research has produced some interesting results, some limitations are noted:

- Deep neural network models have been shown to improve numerical weather prediction forecasts of wind power and power ramps. Although the more complex deep learning models only showed a modest improvement compared with the simpler models, the effectiveness of deep learning models is influenced by the hyper-parameters used. Additional hyper-parameters might improve the accuracy of the deep learning models even further. Furthermore, the sensitivity of deep learning model accuracy to hyper-parameter choice was not investigated.

- Using a specific wavelet scale and discrimination level, the wavelet-surrogate (WS)

method can detect wind power ramp events with a certain ramp rate and timescale. The performance of the algorithm has been assessed using only two sites: the combined wind power generation from the Belgian offshore wind farm cluster and onshore wind power from Sweden. It still requires further testing for a wider range of sites and climatologies.

- Wind power capacity factor and the characteristics of wind power ramps have been associated with clustered weather patterns using only sea level pressure data. Although it has not been explored in this work, taking into account temperature gradients as well as sea level pressure may yield additional weather patterns associated with frontal systems. Such weather patterns may also have a significant influence on wind power production and power ramps.

- In a future climate, the wind power capacity factor and wind power ramp frequency are projected to decrease. Furthermore, the reasons for these changes were linked to changes in the frequency of particular weather patterns. However, a number of variables may affect wind power production and wind power ramp characteristics. For example, this study does not address the relationship between temperature gradients and atmospheric events at the mesoscale with wind power and wind power ramps. This study, rather than focusing on individual wind farms, has primarily focused on larger scale trends where mesoscale effects are less important. More granular studies considering a wider range of variable and their future impact would be beneficial.

- In summary, this study has examined the relationship between weather patterns and wind power output and power ramps in the current and future climate. Large-scale meteorological systems drive the general circulation patterns associated with wind speed, whereas wind power generation and wind power ramps are also influenced by atmospheric phenomena within the atmospheric boundary layer, either at the mesoscale or microscale level. These atmospheric phenomena require a mesoscale model or large-eddy simulation modelling which is not addressed in this work.

7.3. RECOMMENDATIONS

This thesis offers a detailed understanding of offshore wind power and wind power ramps, through modelling, characterising wind power ramps, assessing their relationship to weather patterns, and studying potential changes in a future climate. The information provided by the study is of relevance to both academics and the wind energy sector.

Recommendations resulting from this study are:

- A hybrid model, combining high-resolution numerical weather prediction models with deep learning algorithms, can enhance numerical weather prediction model forecasts of wind power production and wind power ramps. More complex model architectures and model ensembles give modest improvements compared with simpler models but this warrants further investigation.

- A wavelet-surrogate (WS) ramp detection algorithm is effective to extract ramp events of different ramp rates and timescales and its potential should be explored further for a range of climatologies onshore and offshore and for different applications.

- It may be possible to further improve the correlation of wind power and power ramps with clustered weather patterns by adding additional meteorological variables, such as temperature, in addition to sea level pressure.

- This study has considered the impact of changes to the frequency of future weather patterns on large scale production of wind power. Projected changes in wind power production and power ramps should be studied in more detail at the wind farm level taking into account factors such as temperature gradients and atmospheric stability.

7

BIBLIOGRAPHY

[1]   Magdi Ragheb. "History of harnessing wind power". In: *Wind Energy Engineering*. Elsevier, 2017, pp. 127–143.

[2]   Keith Vaughan. "Windmills of Holland". In: *PSA Journal* 72.4 (2006), pp. 30–34.

[3]   Rene Bos. "Extreme gusts and their role in wind turbine design". In: (2017).

[4]   Xiaojing Sun, Diangui Huang, and Guoqing Wu. "The current state of offshore wind energy technology development". In: *Energy* 41.1 (2012), pp. 298–312.

[5]   Lizer Ramirez, Daniel Fraile, and G Brindley. "Offshore wind in Europe: Key trends and statistics 2019". In: (2020).

[6]   Komusanac Ivan et al. "Wind energy in Europe windeurope.org 2021 Statistics and the outlook for 2022-2026 Published in February 2022". In: (2022).

[7]   International Renewable Energy Association et al. *Future of Wind: Deployment, Investment, Technology, Grid Integration and Socio-Economic Aspects (A Global Energy Transformation paper). Abu Dhabi: International Renewable Energy Agency.* 2019.

[8]   Lizer Ramirez, Daniel Fraile, and G Brindley. "Offshore wind in Europe: Key trends and statistics 2020". In: (2021).

[9]   J Wang et al. "Wind power forecasting uncertainty and unit commitment". In: *Applied Energy* 88.11 (2011), pp. 4014–4023.

[10] Cedric De Jonghe et al. "Determining optimal electricity technology mix with high level of wind power penetration". In: *Applied Energy* 88.6 (2011), pp. 2231–2238.

[11] Mingjian Cui et al. "Characterizing and analyzing ramping events in wind power, solar power, load, and netload". In: *Renewable energy* 111 (2017), pp. 227–244.

[12] Laura Bianco et al. "A wind energy ramp tool and metric for measuring the skill of numerical weather prediction models". In: *Weather and Forecasting* 31.4 (2016), pp. 1137–1156.

[13] James F Manwell, Jon G McGowan, and Anthony L Rogers. *Wind energy explained: theory, design and application.* John Wiley & Sons, 2010.

[14] J Freedman, M Markus, and R Penc. "Analysis of West Texas wind plant ramp-up and ramp-down events". In: *AWS Truewind, LLC* (2008).

[15] Cristobal Gallego-Castillo, Alvaro Cuerva-Tejero, and Oscar Lopez-Garcia. "A review on the recent history of wind power ramp forecasting". In: *Renewable and Sustainable Energy Reviews* 52 (2015), pp. 1148–1157.

[16] M Sherry and D Rival. "Meteorological phenomena associated with wind-power ramps downwind of mountainous terrain". In: *Journal of Renewable and Sustainable Energy* 7.3 (2015), p. 033101.

[17] Mathieu Pichault et al. "Characterisation of intra-hourly wind power ramps at the wind farm scale and associated processes". In: *Wind Energy Science* 6.1 (2021), pp. 131–147.

[18] Karla Pereyra-Castro et al. "Wind and wind power ramp variability over Northern Mexico". In: *Atmosphere* 11.12 (2020), p. 1281.

[19] Theresa A Aguilar. "Detecting the long-term frequency of large-scale wind power ramp events observed in ERCOT's aggregated wind power time-series data". PhD thesis. 2019.

[20] IREA IRENA. "Future of wind: Deployment, investment, technology, grid integration and socio-economic aspects". In: (2019).

[21] Dolf Gielen et al. "Global energy transformation: a roadmap to 2050". In: (2019).

[22] Bedassa R Cheneka, Simon J Watson, and Sukanta Basu. "A simple methodology to detect and quantify wind power ramps". In: *Wind Energy Science* 5.4 (2020), pp. 1731–1741.

[23] Bedassa R Cheneka, Simon J Watson, and Sukanta Basu. "Associating Synoptic-Scale Weather Patterns with Aggregated Offshore Wind Power Production and Ramps". In: *Energies* 14.13 (2021), p. 3903.

[24] Bedassa R Cheneka, Simon J Watson, and Sukanta Basu. "The impact of weather patterns on offshore wind power production". In: *Journal of Physics: Conference Series*. Vol. 1618. 6. IOP Publishing. 2020, p. 062032.

[25] Bedassa R Cheneka, Simon J Watson, and Sukanta Basu. "Quantifying the impacts of synoptic weather patterns on North Sea wind power production and ramp events under a changing climate". In: *Energy and Climate Change* (2023), p. 100113.

[26] Peiwen Yu and Anping Lin. "Heuristic Feature Selection for Wind Power Anomaly Events Study". In: *Frontiers in Energy Research* (2021), p. 588.

[27] Dev Tayal. "Achieving high renewable energy penetration in Western Australia using data digitisation and machine learning". In: *Renewable and Sustainable Energy Reviews* 80 (2017), pp. 1537–1543.

[28] Pierre-Julien Trombe, Pierre Pinson, and Henrik Madsen. "A general probabilistic forecasting framework for offshore wind power fluctuations". In: *Energies* 5.3 (2012), pp. 621–657.

[29] Noah Francis. "Predicting sudden changes in wind power generation". In: *North American Windpower* 5.9 (2008), pp. 58–60.

[30] Erik Ela and Jason Kemper. *Wind plant ramping behavior*. Tech. rep. National Renewable Energy Lab.(NREL), Golden, CO (United States), 2009.

[31] Carlos Ferreira et al. *A survey on wind power ramp forecasting*. Tech. rep. Argonne National Lab.(ANL), Argonne, IL (United States), 2011.

[32]   Raffi Sevlian and Ram Rajagopal. "Detection and statistics of wind power ramps". In: *IEEE Transactions on Power Systems* 28.4 (2013), pp. 3610–3620.

[33]   Chandrika Kamath. "Understanding wind ramp events through analysis of historical data". In: *IEEE PES T&D 2010*. IEEE. 2010, pp. 1–6.

[34]   Nicholas Cutler et al. "Detecting, categorizing and forecasting large ramps in wind farm power output using meteorological observations and WPPT". In: *Wind Energy: An International Journal for Progress and Applications in Wind Power Conversion Technology* 10.5 (2007), pp. 453–470.

[35]   YH Wan. *Analysis of wind power ramping behavior in ERCOT*. Tech. rep. National Renewable Energy Lab.(NREL), Golden, CO (United States), 2011.

[36]   Cameron W Potter, Eric Grimit, and Bart Nijssen. "Potential benefits of a dedicated probabilistic rapid ramp event forecast tool". In: *2009 IEEE/PES Power Systems Conference and Exposition*. IEEE. 2009, pp. 1–5.

[37]   Beatrice Greaves et al. "Temporal forecast uncertainty for ramp events". In: *Wind Engineering* 33.4 (2009), pp. 309–319.

[38]   Kristen T Bradford, RL Carpenter, and Brent Shaw. "Forecasting southern plains wind ramp events using the wrf model at 3-km". In: *AMS Student Conference*. Citeseer. 2010.

[39]   Arthur Bossavy, Robin Girard, and Georges Kariniotakis. "Forecasting uncertainty related to ramps of wind power production". In: *European Wind Energy Conference and Exhibition 2010, EWEC 2010*. Vol. 2. European Wind Energy Association. 2010, 9–pages.

[40]   Arthur Bossavy, Robin Girard, and George Kariniotakis. "Forecasting ramps of wind power production with numerical weather prediction ensembles". In: *Wind Energy* 16.1 (2013), pp. 51–63.

[41]   Qing Yang et al. "Evaluation of WRF-predicted near-hub-height winds and ramp events over a Pacific Northwest site with complex terrain". In: *Journal of applied meteorology and climatology* 52.8 (2013), pp. 1753–1763.

[42]   Ásta Hannesdóttir and Mark C Kelly. "Detection and characterization of extreme wind speed ramps". In: *Wind Energy Science* 4.3 (2019), pp. 385–396.

[43]   Feng Ji, Xingguo Cai, and Jihong Zhang. "Wind power prediction interval estimation method using wavelet-transform neuro-fuzzy network". In: *Journal of Intelligent & Fuzzy Systems* 29.6 (2015), pp. 2439–2445.

[44]   Cristóbal Gallego, Alvaro Cuerva, and Alexandre Costa. "Detecting and characterising ramp events in wind power time series". In: 555 (2014), p. 012040.

[45]   Katie Coughlin, Aditya Murthi, and Joseph Eto. "Multi-scale analysis of wind power and load time series data". In: *Renewable energy* 68 (2014), pp. 494–504.

[46]   Jie Zhang et al. "Ramp forecasting performance from improved short-term wind power forecasting over multiple spatial and temporal scales". In: *Energy* 122 (2017), pp. 528–541.

[47]   Raffi Sevlian and Ram Rajagopal. "Detection and statistics of wind power ramps".
       In: *IEEE Transactions on Power Systems* 28.4 (2013), pp. 3610–3620.

[48]   Melinda Marquis et al. "Forecasting the wind to reach significant penetration
       levels of wind energy". In: *Bulletin of the American Meteorological Society* 92.9
       (2011), pp. 1159–1171.

[49]   OpenSkiron. *REGIONAL MODELS EXPLAINED AT EYE LEVEL*. https://openskiron.
       org/en/, Last accessed on 30 Oct Aug 2022. 2022.

[50]   Timothy R Oke. *Boundary layer climates*. Routledge, 2002.

[51]   Richard A Anthes. "The general question of predictability". In: *Mesoscale meteo-
       rology and forecasting*. Springer, 1986, pp. 636–656.

[52]   Yuh-Lang Lin. *Mesoscale dynamics*. Vol. 630. Cambridge University Press Cam-
       bridge, 2007.

[53]   Gary Lackmann. *Midlatitude synoptic meteorology*. American Meteorological So-
       ciety, 2011.

[54]   A DeMarco and S Basu. "On the tails of the wind ramp distributions". In: *Wind
       Energy* 21 (2018), pp. 892–905.

[55]   C. Ferreira et al. *A Survey on Wind Power RAMP Forecasting*. Tech. rep. Argonne
       National Laboratory (ANL), USA, 2011.

[56]   Tianyang Liu et al. "Enhancing Wind Turbine Power Forecast via Convolutional
       Neural Network". In: *Electronics* 10.3 (2021), p. 261.

[57]   Shahram Hanifi et al. "A critical review of wind power forecasting methods—past,
       present and future". In: *Energies* 13.15 (2020), p. 3764.

[58]   Joseph B Olson et al. "Improving wind energy forecasting through numerical weather
       prediction model development". In: *Bulletin of the American Meteorological So-
       ciety* 100.11 (2019), pp. 2201–2220.

[59]   William YY Cheng et al. "The impact of model physics on numerical wind fore-
       casts". In: *Renewable Energy* 55 (2013), pp. 347–356.

[60]   Martin Cenek et al. "Climate change and power security: Power load prediction
       for rural electrical microgrids using long short term memory and artificial neural
       networks". In: *Applied Sciences* 8.5 (2018), p. 749.

[61]   Daniel pradilla. *Convolutional neural network*. https://www.danielpradilla/,
       Last accessed on 17 Aug 2022. 2022.

[62]   Yann LeCun et al. "Gradient-based learning applied to document recognition".
       In: *Proceedings of the IEEE* 86.11 (1998), pp. 2278–2324.

[63]   Alex Krizhevsky, Ilya Sutskever, and Geoffrey E Hinton. "Imagenet classification
       with deep convolutional neural networks". In: *Communications of the ACM* 60.6
       (2017), pp. 84–90.

[64]   Karen Simonyan and Andrew Zisserman. "Very deep convolutional networks for
       large-scale image recognition". In: *arXiv preprint arXiv:1409.1556* (2014).

[65] Christian Szegedy et al. "Going deeper with convolutions". In: *Proceedings of the IEEE conference on computer vision and pattern recognition*. 2015, pp. 1–9.

[66] Kaiming He et al. "Deep residual learning for image recognition". In: *Proceedings of the IEEE conference on computer vision and pattern recognition*. 2016, pp. 770–778.

[67] Peter J Sousounis and Christopher M Little. *Climate Change Impacts on Extreme Weather*. 2017.

[68] UK metoffice. *Causes of climate change*. https://www.metoffice.gov.uk, Last accessed on 17 Aug 2022. 2022.

[69] Valérie Masson-Delmotte et al. "Global warming of 1.5 C". In: *An IPCC Special Report on the impacts of global warming of* 1.5 (2018).

[70] Sonia Seneviratne et al. "Changes in climate extremes and their impacts on the natural physical environment". In: (2012).

[71] Suzana J Camargo, Kerry A Emanuel, and Adam H Sobel. "Use of a genesis potential index to diagnose ENSO effects on tropical cyclone genesis". In: *Journal of Climate* 20.19 (2007), pp. 4819–4834.

[72] Gabriel A Vecchi and Brian J Soden. "Global warming and the weakening of the tropical circulation". In: *Journal of Climate* 20.17 (2007), pp. 4316–4340.

[73] Thomas R Knutson et al. "Dynamical downscaling projections of twenty-first-century Atlantic hurricane activity: CMIP3 and CMIP5 model-based scenarios". In: *Journal of Climate* 26.17 (2013), pp. 6591–6617.

[74] Robert J Trapp et al. "Changes in severe thunderstorm environment frequency during the 21st century caused by anthropogenically enhanced global radiative forcing". In: *Proceedings of the National Academy of Sciences* 104.50 (2007), pp. 19719–19723.

[75] Noah S Diffenbaugh, Martin Scherer, and Robert J Trapp. "Robust increases in severe thunderstorm environments in response to greenhouse forcing". In: *Proceedings of the National Academy of Sciences* 110.41 (2013), pp. 16361–16366.

[76] John T Allen, David J Karoly, and Kevin J Walsh. "Future Australian severe thunderstorm environments. Part II: The influence of a strongly warming climate on convective environments". In: *Journal of Climate* 27.10 (2014), pp. 3848–3868.

[77] Patrick T Marsh, Harold E Brooks, and David J Karoly. "Preliminary investigation into the severe thunderstorm environment of Europe simulated by the Community Climate System Model 3". In: *Atmospheric Research* 93.1-3 (2009), pp. 607–618.

[78] Øystein Hov et al. *Extreme weather events in Europe: preparing for climate change adaptation*. Norwegian Meteorological Institute, 2013.

[79] John A Church et al. "Evaluating the ability of process based models to project sea-level change". In: *Environmental Research Letters* 8.1 (2013), p. 014051.

[80] Ottmar Edenhofer et al. "IPCC special report on renewable energy sources and climate change mitigation". In: *Prepared By Working Group III of the Intergovernmental Panel on Climate Change, Cambridge University Press, Cambridge, UK* (2011).

[81] Jennifer Cronin, Gabrial Anandarajah, and Olivier Dessens. "Climate change impacts on the energy system: a review of trends and gaps". In: *Climatic change* 151.2 (2018), pp. 79–93.

[82] Marco Gaetani et al. "Climate modelling and renewable energy resource assessment". In: *JRC Scientific and Policy Report EUR XXXXX EN* (2015).

[83] Annemarie Devis, Nicole PM Van Lipzig, and Matthias Demuzere. "Should future wind speed changes be taken into account in wind farm development?" In: *Environmental Research Letters* 13.6 (2018), p. 064012.

[84] Isabelle Tobin et al. "Assessing climate change impacts on European wind energy from ENSEMBLES high-resolution climate projections". In: *Climatic Change* 128.1 (2015), pp. 99–112.

[85] Hanna Hueging et al. "Regional changes in wind energy potential over Europe using regional climate model ensemble projections". In: *Journal of Applied Meteorology and Climatology* 52.4 (2013), pp. 903–917.

[86] Isabelle Tobin et al. "Climate change impacts on the power generation potential of a European mid-century wind farms scenario". In: *Environmental Research Letters* 11.3 (2016), p. 034013.

[87] J Scott Hosking et al. "Changes in European wind energy generation potential within a 1.5 C warmer world". In: *Environmental Research Letters* 13.5 (2018), p. 054032.

[88] Richard Davy et al. "Climate change impacts on wind energy potential in the European domain with a focus on the Black Sea". In: *Renewable and sustainable energy reviews* 81 (2018), pp. 1652–1659.

[89] D Carvalho et al. "Potential impacts of climate change on European wind energy resource under the CMIP5 future climate projections". In: *Renewable Energy* 101 (2017), pp. 29–40.

[90] Kepa Solaun and Emilio Cerdá. "Climate change impacts on renewable energy generation. A review of quantitative projections". In: *Renewable and sustainable energy Reviews* 116 (2019), p. 109415.

[91] Asian Development Bank (adb). *Climate Risk and Adaptation in the Electric Power Sector*. ADB Reports RPT124764. Asian Development Bank (ADB), 2014.

[92] Sara C Pryor and RJ Barthelmie. "Climate change impacts on wind energy: A review". In: *Renewable and sustainable energy reviews* 14.1 (2010), pp. 430–437.

[93] SC Pryor and RJ Barthelmie. "Assessing the vulnerability of wind energy to climate change and extreme events". In: *Climatic change* 121.1 (2013), pp. 79–91.

[94] Arkadiusz Mróz, Jan Holnicki-Szulc, and Tuomo Kärnä. "Mitigation of ice loading on off-shore wind turbines: Feasibility study of a semi-active solution". In: *Computers & structures* 86.3-5 (2008), pp. 217–226.

[95]   Clement Hochart et al. "Wind turbine performance under icing conditions". In: *Wind Energy: An International Journal for Progress and Applications in Wind Power Conversion Technology* 11.4 (2008), pp. 319–333.

[96]   Sumeet Kulkarni, MC Deo, and Subimal Ghosh. "Changes in the design and operational wind due to climate change at the Indian offshore sites". In: *Marine Structures* 37 (2014), pp. 33–53.

[97]   Scott Greene, Mark Morrissey, and Sara E Johnson. "Wind climatology, climate change, and wind energy". In: *Geography Compass* 4.11 (2010), pp. 1592–1605.

[98]   Isabelle Tobin et al. "Vulnerabilities and resilience of European power generation to 1.5 C, 2 C and 3 C warming". In: *Environmental Research Letters* 13.4 (2018), p. 044024.

[99]   Juha Kiviluoma et al. "Index for wind power variability". In: *The 13th Wind Integration Workshop, 11th–14th November 2014, Berlin*. Ed. by Uta Betancourt and Thomas Ackermann. Nov. 2014.

[100]   Juha Kiviluoma et al. "Variability in large-scale wind power generation". In: *Wind Energy* 19.9 (2016), pp. 1649–1665.

[101]   Arthur Bossavy, Robin Girard, and Georges Kariniotakis. "Forecasting uncertainty related to ramps of wind power production". In: 2010.

[102]   Nicholas Cutler et al. "Detecting, categorizing and forecasting large ramps in wind farm power output using meteorological observations and WPPT". In: *Wind Energy: An International Journal for Progress and Applications in Wind Power Conversion Technology* 10.5 (2007), pp. 453–470.

[103]   Cristobal Gallego-Castillo, Alvaro Cuerva-Tejero, and Oscar Lopez-Garcia. "A review on the recent history of wind power ramp forecasting". In: *Renewable and Sustainable Energy Reviews* 52 (2015), pp. 1148–1157.

[104]   Elia. *Wind power generation*. https://www.elia.be, Last accessed on 17 Aug 2020. 2020.

[105]   SCB. *Energy prices and switching of suppliers, 3rd quarter 2017*. Tech. rep. Technical Report EN 24 SM 1704. Swedish Energy Agency, 2017.

[106]   EEM20. *EEM20 Forecasting Competition*. https://eem20.eu/, Last accessed on 17 Aug 2020. 2020.

[107]   Stephane Mallat. *A Wavelet Tour of Signal Processing. A Wavelet Tour of Signal Processing*. Academic press, 2009.

[108]   James Theiler et al. "Testing for nonlinearity in time series: the method of surrogate data". In: *Physica D: Nonlinear Phenomena* 58.1-4 (1992), pp. 77–94.

[109]   Helene Laurent and Christian Doncarli. "Stationarity index for abrupt changes detection in the time-frequency plane". In: *IEEE Signal processing letters* 5.2 (1998), pp. 43–45.

[110]   Manuel Davy and Simon Godsill. "Detection of abrupt spectral changes using support vector machines an application to audio signal segmentation". In: 2 (2002), pp. II–1313.

[111] Pierre Borgnat and Patrick Flandrin. "Stationarization via surrogates". In: *Journal of Statistical Mechanics: Theory and Experiment* 2009.01 (2009), P01001.

[112] Diego Guarin, Alvaro Orozco, and Edilson Delgado. "A new surrogate data method for nonstationary time series". In: *arXiv e-prints* (Aug. 2010), arXiv:1008.1804. arXiv: 1008.1804.

[113] Pierre Borgnat et al. "Testing stationarity with surrogates: A time-frequency approach". In: *IEEE Transactions on Signal Processing* 58.7 (2010), pp. 3459–3470.

[114] James Dunyak et al. "Coherent gust detection by wavelet transform". In: *Journal of Wind Engineering and Industrial Aerodynamics* 77 (1998), pp. 467–478.

[115] Xiaoning Gilliam et al. "Coherent structure detection using wavelet analysis in long time-series". In: *Journal of Wind Engineering and Industrial Aerodynamics* 88.2-3 (2000), pp. 183–195.

[116] CJ Steele et al. "Modelling sea-breeze climatologies and interactions on coasts in the southern North Sea: implications for offshore wind energy". In: *Quarterly Journal of the Royal Meteorological Society* 141.690 (2015), pp. 1821–1835.

[117] Christopher Nunalee and Sukanta Basu. "Mesoscale Modeling of Low-Level Jets over the North Sea". In: *Wind Energy - Impact of Turbulence.* Ed. by Michael Hölling, Joachim Peinke, and Stefan Ivanell. Berlin, Heidelberg: Springer Berlin Heidelberg, 2014, pp. 197–202. ISBN: 978-3-642-54696-9.

[118] Peter C Kalverla et al. "Low-level jets over the North Sea based on ERA5 and observations: together they do better". In: *Wind Energy Science* 4.2 (2019), pp. 193–209.

[119] Bo Gu et al. "Short-term forecasting and uncertainty analysis of wind power based on long short-term memory, cloud model and non-parametric kernel density estimation". In: *Renewable Energy* 164 (2021), pp. 687–708.

[120] Huai-zhi Wang et al. "Deep learning based ensemble approach for probabilistic wind power forecasting". In: *Applied energy* 188 (2017), pp. 56–70.

[121] Hui Liu et al. "An experimental investigation of two Wavelet-MLP hybrid frameworks for wind speed prediction using GA and PSO optimization". In: *International Journal of Electrical Power & Energy Systems* 52 (2013), pp. 161–173.

[122] SN Singh, Abheejeet Mohapatra, et al. "Repeated wavelet transform based ARIMA model for very short-term wind speed forecasting". In: *Renewable energy* 136 (2019), pp. 758–768.

[123] Mahdi Khodayar, Jianhui Wang, and Mohammad Manthouri. "Interval deep generative neural network for wind speed forecasting". In: *IEEE Transactions on Smart Grid* 10.4 (2018), pp. 3974–3989.

[124] Mahdi Khodayar and Jianhui Wang. "Spatio-temporal graph deep neural network for short-term wind speed forecasting". In: *IEEE Transactions on Sustainable Energy* 10.2 (2018), pp. 670–681.

[125] Gabriel de Freitas Viscondi and Solange N Alves-Souza. "A Systematic Literature Review on big data for solar photovoltaic electricity generation forecasting". In: *Sustainable Energy Technologies and Assessments* 31 (2019), pp. 54–63.

[126]   Tanveer Ahmad and Huanxin Chen. "Deep learning for multi-scale smart energy forecasting". In: *Energy* 175 (2019), pp. 98–112.

[127]   Qing Cao, Bradley T Ewing, and Mark A Thompson. "Forecasting wind speed with recurrent neural networks". In: *European Journal of Operational Research* 221.1 (2012), pp. 148–154.

[128]   Hui Liu, Hong-qi Tian, and Yan-fei Li. "Four wind speed multi-step forecasting models using extreme learning machines and signal decomposing algorithms". In: *Energy conversion and management* 100 (2015), pp. 16–22.

[129]   Hui Liu et al. "Forecasting models for wind speed using wavelet, wavelet packet, time series and Artificial Neural Networks". In: *Applied Energy* 107 (2013), pp. 191–208.

[130]   Hui Liu et al. "A hybrid model for wind speed prediction using empirical mode decomposition and artificial neural networks". In: *Renewable energy* 48 (2012), pp. 545–556.

[131]   Kazutoshi Higashiyama, Yu Fujimoto, and Yasuhiro Hayashi. "Feature extraction of NWP data for wind power forecasting using 3D-convolutional neural networks". In: *Energy Procedia* 155 (2018), pp. 350–358.

[132]   Kazutoshi Higashiyama, Yu Fujimoto, and Yasuhiro Hayashi. "Feature extraction of numerical weather prediction results toward reliable wind power prediction". In: *2017 IEEE PES Innovative Smart Grid Technologies Conference Europe (ISGT-Europe)*. IEEE. 2017, pp. 1–6.

[133]   Sukanta Basu et al. "Day-ahead Wind Power Predictions at Regional Scales: Post-processing Operational Weather Forecasts with a Hybrid Neural Network". In: *2020 17th International Conference on the European Energy Market (EEM)*. IEEE. 2020, pp. 1–6.

[134]   Eric Lacoa Arends et al. "Probabilistic wind power forecasting combining deep learning architectures". In: *2020 17th International Conference on the European Energy Market (EEM)*. IEEE. 2020, pp. 1–6.

[135]   Tinghui Ouyang, Heming Huang, and Yusen He. "Ramp events forecasting based on long-term wind power prediction and correction". In: *IET Renewable Power Generation* 13.15 (2019), pp. 2793–2801.

[136]   Li Han et al. "Wind Power Ramp Event Forecasting Based on Feature Extraction and Deep Learning". In: *Energies* 13.23 (2020), p. 6449.

[137]   Yu Ding, Jiong Tang, and Jianhua Z Huang. "Data analytics methods for wind energy applications". In: *Turbo Expo: Power for Land, Sea, and Air*. Vol. 56802. American Society of Mechanical Engineers. 2015, V009T46A020.

[138]   Matt W Gardner and SR Dorling. "Artificial neural networks (the multilayer perceptron)—a review of applications in the atmospheric sciences". In: *Atmospheric environment* 32.14-15 (1998), pp. 2627–2636.

[139]   Kaiming He and Jian Sun. "Convolutional neural networks at constrained time cost". In: *Proceedings of the IEEE conference on computer vision and pattern recognition*. 2015, pp. 5353–5360.

[140] Rupesh Kumar Srivastava, Klaus Greff, and Jürgen Schmidhuber. "Highway networks". In: *arXiv preprint arXiv:1505.00387* (2015).

[141] Christopher M Bishop et al. *Neural networks for pattern recognition*. Oxford university press, 1995.

[142] Brian D Ripley. *Pattern recognition and neural networks*. Cambridge university press, 2007.

[143] Christian Szegedy et al. "Rethinking the inception architecture for computer vision". In: *Proceedings of the IEEE conference on computer vision and pattern recognition*. 2016, pp. 2818–2826.

[144] Diederik P Kingma and Jimmy Ba. "Adam: A method for stochastic optimization". In: *arXiv preprint arXiv:1412.6980* (2014).

[145] Lutz Prechelt. "Early stopping-but when?" In: *Neural Networks: Tricks of the trade*. Springer, 1998, pp. 55–69.

[146] Xavier Glorot and Yoshua Bengio. "Understanding the difficulty of training deep feedforward neural networks". In: *Proceedings of the thirteenth international conference on artificial intelligence and statistics*. JMLR Workshop and Conference Proceedings. 2010, pp. 249–256.

[147] Abien Fred Agarap. "Deep learning using rectified linear units (relu)". In: *arXiv preprint arXiv:1803.08375* (2018).

[148] David James Brayshaw et al. "The impact of large scale atmospheric circulation patterns on wind power generation and its potential predictability: A case study over the UK". In: *Renewable Energy* 36.8 (2011), pp. 2087–2096. ISSN: 0960-1481.

[149] J.M. Correia et al. "The influence of the main large-scale circulation patterns on wind power production in Portugal". In: *Renewable Energy* 102 (2017), pp. 214–223. ISSN: 0960-1481.

[150] Christian M. Grams et al. "Balancing Europe's wind-power output through spatial deployment informed by weather regimes". In: *Nature Climate Change* 7.8 (July 2017), pp. 557–562.

[151] Hazel E Thornton et al. "The relationship between wind power, electricity demand and winter weather patterns in Great Britain". In: *Environmental Research Letters* 12.6 (June 2017), p. 064017.

[152] Lucy C Cradden and Frank McDermott. "A weather regime characterisation of Irish wind generation and electricity demand in winters 2009–11". In: *Environmental Research Letters* 13.5 (May 2018), p. 054022.

[153] Daniel R Drew, Janet F Barlow, and Phil J Coker. "Identifying and characterising large ramps in power output of offshore wind farms". In: *Renewable Energy* 127 (2018), pp. 195–203.

[154] Masamichi Ohba, Shinji Kadokura, and Daisuke Nohara. "Impacts of synoptic circulation patterns on wind power ramp events in East Japan". In: *Renewable Energy* 96 (Oct. 2016), pp. 591–602.

[155] Hubert Horace Lamb. "British Isles weather types and a register of the daily sequence of circulation patterns 1861-1971". In: *Geophysical Memoir 116* (1972).

[156] A Jenkinson and F Collison. "An initial climatology of gales over the North sea. Synoptic Climatology Branch Memorandum". In: *Meteorol. Off* (1977), pp. 1–62.

[157] FW Gerstengarbe and PC Werner. "Katalog der Grosswetterlagen Europas nach Paul Hess und Helmut Brezowski 1881–1992, 4., vollständ. neu bearb". In: *Aufl., Deutscher Wetterdienst, Offenbach, Germany* (1993).

[158] Robert Neal et al. "A flexible approach to defining weather patterns and their application in weather forecasting over Europe". In: *Meteorological Applications* 23.3 (Apr. 2016), pp. 389–400.

[159] Shih-Hao Su et al. "Identification of synoptic weather types over Taiwan area with multiple classifiers". In: *Atmospheric Science Letters* 19.12 (2018), e861.

[160] Yonggang Liu. "Patterns of ocean current variability on the West Florida Shelf using the self-organizing map". In: *Journal of Geophysical Research* 110.C6 (2005).

[161] Yonggang Liu, Robert H. Weisberg, and Christopher N. K. Mooers. "Performance evaluation of the self-organizing map for feature extraction". In: *Journal of Geophysical Research* 111.C5 (2006).

[162] Pieter-Jan Marsboom. "Belgian Wind Forecasting - Phase 1". In: *Elia Publishing* 13.5 (Feb. 2012), p. 25.

[163] H. Hersbach et al. "ERA5 hourly data on single levels from 1979 to present. Copernicus Climate Change Service (C3S) Climate Data Store (CDS)." In: (2018). Accessed on 05.12.2020.

[164] T. Kohonen, M. R. Schroeder, and T. S. Huang, eds. *Self-Organizing Maps*. 3rd. Berlin, Heidelberg: Springer-Verlag, 2001. ISBN: 3540679219.

[165] Teuvo Kohonen. "The self-organizing map". In: *Proceedings of the IEEE* 78.9 (1990), pp. 1464–1480.

[166] Teuvo Kohonen. "Essentials of the self-organizing map". In: *Neural networks* 37 (2013), pp. 52–65.

[167] Robert Neal et al. "A flexible approach to defining weather patterns and their application in weather forecasting over Europe". In: *Meteorological Applications* 23.3 (2016), pp. 389–400.

[168] Teuvo Kohonen et al. "Som pak: The self-organizing map program package". In: *Report A31, Helsinki University of Technology, Laboratory of Computer and Information Science* 1.1-27 (1996), pp. 39–40.

[169] John W Sammon. "A nonlinear mapping for data structure analysis". In: *IEEE Transactions on Computers* 100.5 (1969), pp. 401–409.

[170] Nicola Cortesi et al. "Characterization of European wind speed variability using weather regimes". In: *Climate Dynamics* 53.7 (2019), pp. 4961–4976.

[171] Karin van der Wiel et al. "The influence of weather regimes on European renewable energy production and demand". In: *Environmental Research Letters* 14.9 (2019), p. 094010.

[172]   Climate Change IRENA and Renewable Energy. "National policies and the role of communities, cities and regions (Report to the G20 Climate Sustainability Working Group (CSWG))". In: *International Renewable Energy Agency, Abu Dhabi* (2019).

[173]   WindEurope. "2020 Statistics and the outlook for 2021-2025,Published in February 2021". In: *WindEurope* (2021).

[174]   WindEurope. *Offshore wind energy 2022 mid-year statistics.* Tech. rep. WindEurope, 2022.

[175]   SD Outten and I Esau. "Extreme winds over Europe in the ENSEMBLES regional climate models". In: *Atmos. Chem. Phys* 13.10 (2013), pp. 5163–5172.

[176]   Andreina Belušić Vozila et al. "Wind over the Adriatic region in CORDEX climate change scenarios". In: *Journal of Geophysical Research: Atmospheres* 124.1 (2019), pp. 110–130.

[177]   Julia Moemken et al. "Future changes of wind speed and wind energy potentials in EURO-CORDEX ensemble simulations". In: *Journal of Geophysical Research: Atmospheres* 123.12 (2018), pp. 6373–6389.

[178]   Julia Moemken et al. "Wind speed and wind energy potentials in EURO-CORDEX ensemble simulations: evaluation, bias-correction and future changes". In: *EGU General Assembly Conference Abstracts.* Vol. 19. 2017, p. 13305.

[179]   Burkhardt Rockel and Katja Woth. "Extremes of near-surface wind speed over Europe and their future changes as estimated from an ensemble of RCM simulations". In: *Climatic Change* 81.1 (2007), pp. 267–280.

[180]   Anders Höglund et al. *Validation and correction of regionalised ERA-40 wind fields over the Baltic Sea using the Rossby Centre Atmosphere model RCA3. 0.* SMHI, 2009.

[181]   I Koletsis et al. "Assessment of offshore wind speed and power potential over the Mediterranean and the Black Seas under future climate changes". In: *Renewable and Sustainable Energy Reviews* 60 (2016), pp. 234–245.

[182]   Mark Reyers, Julia Moemken, and Joaquim G Pinto. "Future changes of wind energy potentials over Europe in a large CMIP5 multi-model ensemble". In: *International Journal of Climatology* 36.2 (2016), pp. 783–796.

[183]   Juliane Weber, Fabian Gotzens, and Dirk Witthaut. "Impact of strong climate change on the statistics of wind power generation in Europe". In: *Energy Procedia* 153 (2018), pp. 22–28.

[184]   Detlef P Van Vuuren et al. "The representative concentration pathways: an overview". In: *Climatic change* 109.1 (2011), pp. 5–31.

[185]   Gareth P Harrison, Lucy C Cradden, and John P Chick. "Preliminary assessment of climate change impacts on the UK onshore wind energy resource". In: *Energy Sources, Part A* 30.14-15 (2008), pp. 1286–1299.

[186]   Simon Watson. "Quantifying the variability of wind energy". In: *Wiley Interdisciplinary Reviews: Energy and Environment* 3.4 (2014), pp. 330–342.

[187]   Masamichi Ohba. "The impact of global warming on wind energy resources and ramp events in Japan". In: *Atmosphere* 10.5 (2019), p. 265.

[188]   David James Brayshaw et al. "The impact of large scale atmospheric circulation patterns on wind power generation and its potential predictability: A case study over the UK". In: *Renewable Energy* 36.8 (2011), pp. 2087–2096.

[189]   Jose M Garrido-Perez et al. "Impact of weather regimes on wind power variability in western Europe". In: *Applied Energy* 264 (2020), p. 114731.

[190]   Teuvo Kohonen. *Self-organizing maps*. Vol. 30. Springer Science & Business Media, 2012.

[191]   Bedassa R Cheneka, Simon J Watson, and Sukanta Basu. "The impact of weather patterns on offshore wind power production". In: *Journal of Physics: Conference Series* 1618 (Sept. 2020), p. 062032.

[192]   ESGF. *ESGF@LiU in cooperation with SMHI*. 2021. URL: https://esg-dn1.nsc.liu.se. (last accessed: 14.03.2021).

[193]   Daniela Jacob et al. "EURO-CORDEX: new high-resolution climate change projections for European impact research". In: *Regional environmental change* 14.2 (2014), pp. 563–578.

[194]   Reto Knutti and Jan Sedláček. "Robustness and uncertainties in the new CMIP5 climate model projections". In: *Nature climate change* 3.4 (2013), pp. 369–373.

[195]   Aurore Voldoire et al. "The CNRM-CM5. 1 global climate model: description and basic evaluation". In: *Climate dynamics* 40.9-10 (2013), pp. 2091–2121.

[196]   W Hazeleger et al. "EC-Earth V2. 2: description and validation of a new seamless earth system prediction model". In: *Climate dynamics* 39.11 (2012), pp. 2611–2629.

[197]   Olivier Marti et al. "Key features of the IPSL ocean atmosphere model and its sensitivity to atmospheric resolution". In: *Climate Dynamics* 34.1 (2010), pp. 1–26.

[198]   Cdea Jones et al. "The HadGEM2-ES implementation of CMIP5 centennial simulations". In: *Geoscientific Model Development* 4 (2011), pp. 543–570.

[199]   Marco A Giorgetta et al. "Climate and carbon cycle changes from 1850 to 2100 in MPI-ESM simulations for the Coupled Model Intercomparison Project phase 5". In: *Journal of Advances in Modeling Earth Systems* 5.3 (2013), pp. 572–597.

[200]   Mats Bentsen et al. "The Norwegian earth system model, NorESM1-M-Part 1: Description and basic evaluation". In: *GMDD* 5.3 (2012), pp. 2843–2931.

[201]   T Iversen et al. *The Norwegian Earth System Model, NorESM1-M–Part 2: Climate response and scenario projections, Geosci. Model Dev., 6, 389–415*. 2013.

[202]   Stefan Emeis. *Wind energy meteorology: atmospheric physics for wind power generation*. Springer, 2018.

[203]   Cian Desmond et al. "Description of an 8 MW reference wind turbine". In: *Journal of Physics: Conference Series*. Vol. 753. 9. IOP Publishing. 2016, p. 092013.

[204]   Masamichi Ohba, Shinji Kadokura, and Daisuke Nohara. "Impacts of synoptic circulation patterns on wind power ramp events in East Japan". In: *Renewable energy* 96 (2016), pp. 591–602.

[205]   Sven-Erik Gryning et al. "On the extension of the wind profile over homogeneous terrain beyond the surface boundary layer". In: *Boundary-layer Meteorology* 124 (2007), pp. 251–268.

[206]   Sergej S Zilitinkevich and Igor N Esau. "Resistance and heat-transfer laws for stable and neutral planetary boundary layers: Old theory advanced and re-evaluated". In: *Quarterly Journal of the Royal Meteorological Society* 131 (2005), pp. 1863–1892.

[207]   S Basu. "Vertical wind speed profiles in atmospheric boundary layer flows". In: *Wind energy engineering: a handbook for onshore and offshore wind turbines, 2nd Edition*. Ed. by T Letcher. Elsevier, 2022.

[208]   D Carvalho et al. "Wind energy resource over Europe under CMIP6 future climate projections: What changes from CMIP5 to CMIP6". In: *Renewable and Sustainable Energy Reviews* 151 (2021), p. 111594.

[209]   Jan Wohland. "Process-based climate change assessment for European winds using EURO-CORDEX and global models". In: *Environmental Research Letters* 17.12 (2022), p. 124047.

[210]   Andrea N Hahmann, Oscar Garcı-a-Santiago, and Alfredo Peña. "Current and future wind energy resources in the North Sea according to CMIP6". In: *Wind Energy Science* 7.6 (2022), pp. 2373–2391.

ACKNOWLEDGEMENTS

Last but least, my deepest gratitude goes to my family, brothers, and sisters who were with me. Meaza, thank you for being a supportive wife during the Ph.D. time and for taking responsibility during the challenging time. My two superheroes, Elyad and Eba, always remind me to refrain from working during weekends and to leave the office early, so we will have more time together now. Booniko, the little princess, officially became a cherished member of the family on 20 March 2022. Your presence has been a true blessing throughout the challenging journey.

Above all, I extend my boundless gratitude to the Almighty God, the creator of Heaven and Earth, for His unwavering care and guidance throughout the trials and adventures I have traversed. It is through His strength, grace, and wisdom that I stand here today as the person I am.

Bedassa R. Cheneka
Delft, September 2023

Curriculum Vitæ

Bedassa Regassa Cheneka

08 – 01 – 1981	Born in Bekoji, Ethiopia.

Education

2001 – 2005	Bachelor of Science in Meteorology Arba Minch University, Ethiopia
2007 – 2009	Master of Science in Meteorology Arba Minch University, Ethiopia
2018 – 2023	Doctor of Philosophy in Wind Energy Technische Universiteit Delft (Delft University of Technology)

Thesis: Wind Power Ramps: Forecasting, Characterisation and Future Projection

Promotor: Prof. dr. S. J. Watson and Prof. dr. S. Basu

Work Experiences

2005 – 2007	Meteorologist National Meteorological Agency, Ethiopia
2009 – 2012	Lecturer Arba Minch University, Ethiopia
2012 – 2013	Lecturer Adama Science and Technology University, Ethiopia
2015 – 2015	Meteorologist National Meteorological Agency, Ethiopia
2015 – 2018	Senior Project Officer Agricultural Transformation Agency, Ethiopia

AWARDS

2013	Asia Pacific Climate Center (APCC) Young Scientist Support Program
2014	Alexander von Humboldt International Climate Protection Fellowship

LIST OF PUBLICATIONS

JOURNAL PAPERS

3. **Cheneka, B.R.**, Watson, S.J. and Basu, S., *Quantifying the impacts of synoptic weather patterns on North Sea wind power production and ramp events under a changing climate*, Energy and Climate Change.

2. **Cheneka, B.R.**, Watson, S.J. and Basu, S., *Associating Synoptic-Scale Weather Patterns with Aggregated Offshore Wind Power Production and Ramps*, Energies **p.3903**, 14(2021).

1. **Cheneka, B.R.**, Watson, S.J. and Basu, S., *A simple methodology to detect and quantify wind power ramps*, Wind Energ. Sci., 5, 1731–1741, **2020**.

CONFERENCE PAPERS

3. **Cheneka, B.R.**, Watson, S.J. and Basu, S., *The impact of weather patterns on offshore wind power production.*, Journal of Physics: Conference Series, 1618 (6), **2020**.

2. Basu, S., Watson, S. J., Arends, E. L., and **Cheneka, B.R.**, *Day-ahead Wind Power Predictions at Regional Scales: Post-processing Operational Weather Forecasts with a Hybrid Neural Network.*, 2020 17th International Conference on the European Energy Market (EEM), pp. 1-6, **2020**.

1. Arends, E. L., Watson, S. J., Basu, S. and **Cheneka, B.R.**, *Probabilistic wind power forecasting combining deep learning architectures.*, 2020 17th International Conference on the European Energy Market (EEM), pp. 1-6, **2020**.

CONFERENCES ATTENDED

3. **Cheneka, B.R.**, Watson, S.J. and Basu, S., *Potential Changes in Wind Power Ramp Behaviour under a Projected Climate Change Scenario*, , Wind Energy Science Conference, 25 – 28 May **2021**, Hannover, Germany.

2. **Cheneka, B.R.**, Watson, S.J. and Basu, S., *The Impact of Weather Patterns on Offshore Wind Power Production* , Torque 2020, 28 September – 2 October **2020**, Delft, The Netherlands.

1. **Cheneka, B.R.**, Watson, S.J. and Basu, S., *Association Between Offshore Wind Characteristics over the North Sea and Weather Pattern Clusters Determined using Self-Organising Maps (SOMs)*, Wind Energy Science Conference,17 - 20 June **2019**, Cork, Ireland.